



## Index of contributed talks CMiF 2019

### Session T1, Monday 19 August 11:00 – 12:30

<b>T1.1</b>	Giuseppe Antonio	Zampogna	EPFL (CH)
<b>T1.2</b>	Antoine	Riaud	Fudan University (CN)
<b>T1.3</b>	Joachim	Delannoy	EPSCI & Ecole Polytechnique (FR)
<b>T1.4</b>	Gabriel	Le Doudic	Université Paris Diderot (FR)
<b>T1.5</b>	Saswata	Basak	IIT Bombay (IN)

### Session T2, Tuesday 20 August 11:00 – 12:30

<b>T2.1</b>	Massimiliano	Rossi	Technical University of Denmark (DK)
<b>T2.2</b>	Rune	Barnkob	TU Munich (DE)
<b>T2.3</b>	Wei	Qiu	Lund University (SE)
<b>T2.4</b>	Udita	Gosh	Université de Lille (FR)
<b>T2.5</b>	Anthony	Bonfils	NORDITA (SE)

### Session T3, Wednesday 21 August 11:00 – 12:30

<b>T3.1</b>	Diana	Garcia-Gonzalez	University of Twente (NL)
<b>T3.2</b>	Srinath	Lakshman	University of Twente (NL)
<b>T3.3</b>	Walter	Tewes	University of Twente (NL)
<b>T3.4</b>	Abhinav	Naga	Max Planck Inst, Polymer Research (DE)
<b>T3.5</b>	Alexandros	Oratis	Boston University (US)

### Session T4, Thursday 22 August 11:00 – 12:30

<b>T4.1</b>	Valentina	Vitali	Lund University (SE)
<b>T4.2</b>	Jacob Søberg	Bach	Technical University of Denmark (DK)
<b>T4.3</b>	Armaghan (Amy)	Fakhfour	SAWLab Saxony, IFW Dresden (DE)
<b>T4.4</b>	Weiwei	Cui	Tianjin University (CN)
<b>T4.5</b>	Yao	Lu	University of Twente (NL)

### Session T5, Thursday 22 August 20:00 – 21:00

<b>T5.1</b>	Élfego	Ruiz-Gutiérrez	Northumbria University (GB)
<b>T5.2</b>	Yaxing	Li	University of Twente (NL)
<b>T5.3</b>	Melika	Motaghian	Wageningen University (NL)

### Session T6, Friday 23 August 11:00 – 12:30

<b>T6.1</b>	Mads	Rode	Technical University of Denmark (DK)
<b>T6.2</b>	Minji	Kim	Washington University in St. Louis (US)
<b>T6.3</b>	Aina	Ramamonjy	Université Paris Diderot (FR)
<b>T6.4</b>	Christian	Esparza Lopez	University of Cambridge (GB)
<b>T6.5</b>	Juliette	Amauger	Ecole Polytechnique (FR)

### Session T7, Friday 23 August 17:00 – 18:00

<b>T7.1</b>	Pallav	Kant	University of Twente (NL)
<b>T7.2</b>	Lukas	Hauer	Max Planck Inst, Polymer Research (DE)
<b>T7.3</b>	Vatsal	Sanjay	University of Twente (NL)



# A homogenization-based model for fluids flowing across permeable thin interfaces: an effective stress jump condition

Giuseppe A. Zampogna<sup>1</sup>, François Gallaire<sup>1</sup>

<sup>1</sup>Laboratory of Fluid Mechanics and Instabilities, EPFL, Lausanne, Switzerland

E-mail: [giuseppe.zampogna@epfl.ch](mailto:giuseppe.zampogna@epfl.ch),

## Introduction

The dynamics of fluid flowing across thin permeable surfaces (i.e. membranes) is an intrinsically multiscale phenomenon, owing to very different scales. A clear explanation of the mechanisms at the basis of membrane processes is necessary, since they have applications in many industrial fields. In the present project, we use a multi-scale homogenization technique to develop an equivalent model to simulate the hydrodynamic interactions between a rigid membrane and a surrounding incompressible fluid flow. The model, able to provide a description of the micro- and macro-scopic fluid behavior, consists of a constraint to be satisfied by the fluid velocity components, imposed within the fluid domain, over a virtual smooth surface passing through the center of each pore. It shows that the membrane produces a jump in fluid stresses whose intensity and direction, formally evaluated solving problems at the microscale, depend on the external flow and on the pore geometry.

## The effective jump model

The formal development of the equivalent model can be found in [3]. It consists of joining a standard homogenization technique [1] and match asymptotic expansions to determine correct boundary conditions for the microscopic problems as done in [2]. To carry out the model, we assume that the

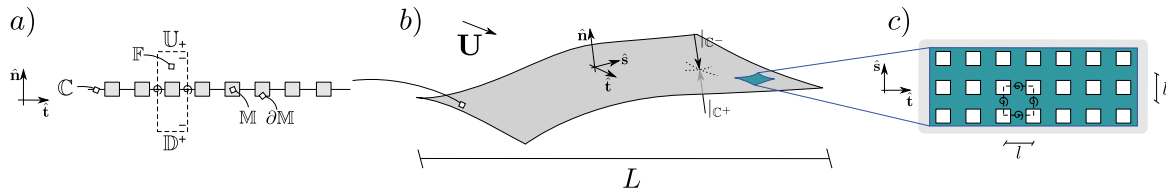


**Figure 1:** A fluid flow with an incoming velocity  $\mathbf{U}$  encounters a smooth permeable surface characterized by a macroscopic length scale  $L$  (frame  $b$ ). In frames  $a$  and  $c$ , a zoom in on the two orthogonal planes  $(\hat{\mathbf{t}}, \hat{\mathbf{n}})$  and  $(\hat{\mathbf{t}}, \hat{\mathbf{s}})$  reveals that the surface presents a microscopic structure, whose thickness and pore size is of order  $l$ . The structure is periodic and an elementary microscopic cell can be identified (the dashed rectangles in frames  $a$  and  $b$ ). The flow field is assumed microscopically periodic within this cell.

non-dimensional Stokes equations are valid in the fluid domain, denoted in figure 1 with  $\mathbb{F}$ ,

$$0 = \nabla \cdot \boldsymbol{\Sigma}, \quad \nabla \cdot \mathbf{u} = 0 \quad (1)$$

with  $\boldsymbol{\Sigma} = -p\mathbf{I} + \mu(\nabla\mathbf{u} + \nabla\mathbf{u}^T)$  the fluid stress tensor and  $\mathbf{u}$  and  $p$  denoting the fluid velocity and pressure. Since the phenomenon is multiscale, we can decompose its physical description in different sub-phenomena at each scale. Formally, this means that we introduce an infinitesimal separation of scales parameter  $\epsilon = l/L$ , with  $l$  and  $L$  defined in figure 1, and we decompose the spatial variable in a microscopic,  $\mathbb{F}$ -periodic part,  $\mathbf{x}$ , and a macroscopic part  $\mathbf{X} = \epsilon\mathbf{x}$  and we search for a solution of the flow field of the type  $f = \sum_{n=0}^{+\infty} \epsilon^n f^{(n)}(\mathbf{x}, \mathbf{X}, t)$ , with  $f \in \{p, \mathbf{u}, \boldsymbol{\Sigma}\}$  and  $f^{(n)}$  representing the  $n$ -th order approximation of  $f$  with respect to the parameter  $\epsilon$ . After applying homogenization, the leading order approximation of the velocity can be written as

$$\bar{\mathbf{u}}^{(0)}|_{\mathbb{C}} = \bar{\mathbf{M}} : \boldsymbol{\Sigma}^{(0)}|_{\mathbb{C}^-} + \bar{\mathbf{N}} : \boldsymbol{\Sigma}^{(0)}|_{\mathbb{C}^+}, \quad \bar{\mathbf{u}}^{(0)}|_{\mathbb{C}} = \bar{\mathbf{u}}^{(0)}|_{\mathbb{C}^-} = \bar{\mathbf{u}}^{(0)}|_{\mathbb{C}^+}, \quad (2)$$

where the symbols  $|_{\mathbb{C}^-}$  and  $|_{\mathbb{C}^+}$  denotes the limit toward the upwind and downwind directions introduced in figure 1.  $\bar{\mathbf{M}}$  and  $\bar{\mathbf{N}}$  are the upwind and downwind third order motility tensors, whose equations, valid on the microscopic elementary cell introduced in figure 1, are found during the homogenization procedure

$$\begin{cases} -\nabla\mathbf{Q} + \nabla^2\mathbf{M} = 0, \\ \nabla \cdot \mathbf{M} = 0, \\ \boldsymbol{\Sigma}(\mathbf{Q}, \mathbf{M}) \cdot \mathbf{n} = \mathbf{I} \wedge \mathbf{I} \cdot \mathbf{n} \quad \text{on } \mathbb{U}, \\ \boldsymbol{\Sigma}(\mathbf{Q}, \mathbf{M}) \cdot \mathbf{n} = 0 \quad \text{on } \mathbb{D}, \end{cases} \quad \begin{cases} -\nabla\mathbf{R} + \nabla^2\mathbf{N} = 0, \\ \nabla \cdot \mathbf{N} = 0, \\ \boldsymbol{\Sigma}(\mathbf{R}, \mathbf{N}) \cdot \mathbf{n} = 0 \quad \text{on } \mathbb{U}, \\ \boldsymbol{\Sigma}(\mathbf{R}, \mathbf{N}) \cdot \mathbf{n} = \mathbf{I} \wedge \mathbf{I} \cdot \mathbf{n} \quad \text{on } \mathbb{D}, \end{cases} \quad (3)$$

with  $\mathbf{M}, \mathbf{Q}, \mathbf{N}$  and  $\mathbf{R}$   $\mathbb{F}$ -periodic and  $\mathbf{M} = \mathbf{N} = 0$  on  $\partial\mathbb{M}$ .  $\mathbf{Q}$  and  $\mathbf{R}$  are second order tensors introduced during the homogenization procedure and are physically unimportant. In equation (2), the symbol  $\bar{\cdot}$  denotes a spatial average carried out by integrating the variables over a surface  $\mathbb{C}$  lying on  $(\mathbf{s}, \mathbf{t})$  and intersecting each elementary cell in the center of the solid inclusion  $\mathbb{M}$ , i.e.

$$\bar{f} := \frac{1}{|\mathbb{C}_{\mathbb{F}} \cup \mathbb{C}_{\mathbb{M}}|} \int_{\mathbb{C}_{\mathbb{F}}} f dA. \quad (4)$$

$\mathbb{C}_{\mathbb{F}}$  and  $\mathbb{C}_{\mathbb{M}}$  are respectively the fluid and solid part of  $\mathbb{C}$ , within a given microscopic elementary cell. Condition (2), a purely macroscopic equation depending only on  $\mathbf{X}$ , states that, while the velocity is continuous across the membrane, a jump in the fluid stresses is produced, whose direction and intensity depend on the microscopic geometry.

### Validation and results

In order to be able to apply the developed model, the solution of problems (3) is computed for a given microscopic structure (cf. figure 2 for an example). Once averaged values of the microscopic tensors are computed, condition (2) can be used in a given macroscopic configuration. The membrane is an interface which splits the fluid domain in the upwind and downwind part, and condition (2) is used numerically to exchange informations between these two fluid regions. The macroscopic fields obtained with equation (2) are compared with the solution of full-scale numerical simulations, showing a good agreement up to an order  $\epsilon^2$ , in an averaged sense, as predicted by the theory.

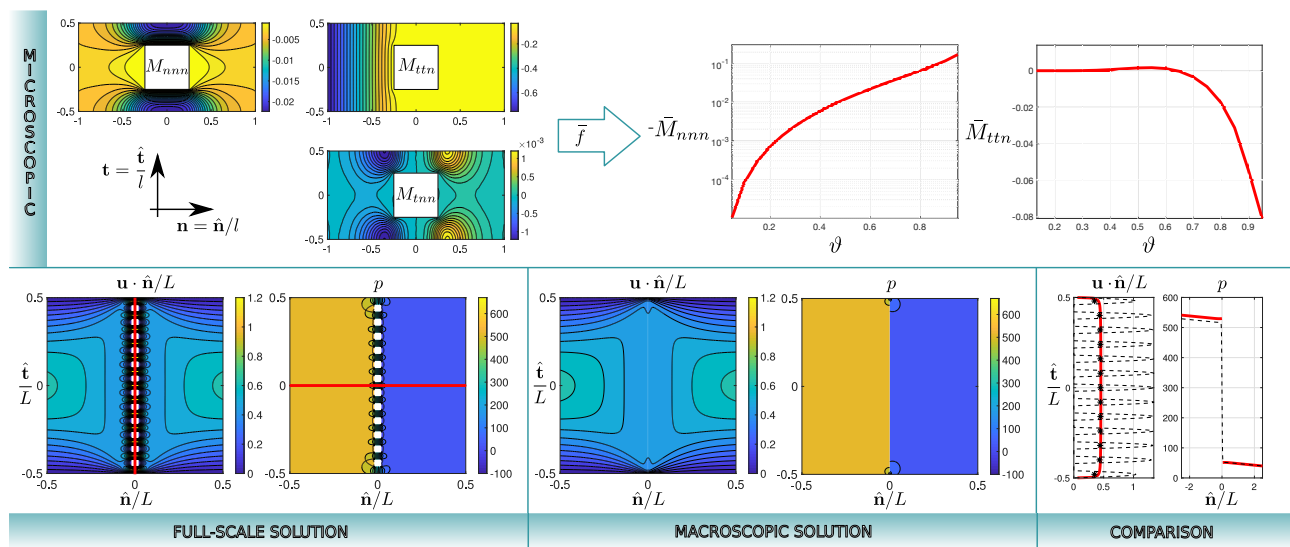


**Figure 2:** Solution and validation procedure. “Microscopic” panel: on the left isocontours of some components of  $\mathbf{M}$  are shown for a simple 2D microscopic domain. On the right, the average (4) of  $\mathbf{M}$  is used to characterize the microscopic geometry with respect to the fluid ratio  $\vartheta = |\mathbb{C}_{\mathbb{F}}|/|\mathbb{C}_{\mathbb{F}} \cup \mathbb{C}_{\mathbb{M}}|$ . In the bottom row a 2D channel flow enforced by a constant inlet normal velocity is proposed. The channel is split in two parts by the membrane and the isocontours of normal velocity and pressure are shown in the region around the membrane, whose microscopic structure can be appreciated in the “full-scale solution” panel. Condition (2) is applied as an interface condition on the permeable surface (“macroscopic solution” panel) and for validation purposes the velocity and pressure profiles have been compared over the corresponding red lines sketched in the full-scale solution. In the “comparison” panel the red lines represent the solution of the macroscopic model, the dashed black lines the full-scale solution and the stars the full-scale solution after applying the average defined in (4).

### Conclusion

The model developed, able to simulate the presence of a rigid permeable membrane within a fluid domain, represents a step forward a more formal description of membrane processes. It allows to characterize the microscopic structure of a membrane and its effects on the macroscopic flow. At the present stage, we focused on the hydrodynamics across the membrane. This is the basis to develop a more complete multiphysics tool to describe others aspects like solute transport and membrane deformability.

### References

- [1] G.A. Zampogna and A. Bottaro. Fluid flow over and through a regular bundle of rigid fibres. *Journal of Fluid Mechanics* **792**, 5-35 (2016).
- [2] G.A. Zampogna, J. Magnaudet and A. Bottaro. Generalized slip condition over rough surfaces. *Journal of Fluid Mechanics* **858**, 407-436 (2019).
- [3] G.A. Zampogna and F. Gallaire. Effective stress jump across membranes. *Journal of Fluid Mechanics*, *submitted*.



## Observation of voltage-dependent contact angle hysteresis

Antoine Riaud<sup>1</sup>, Wei Wang<sup>1</sup>, Qi Wang<sup>1</sup>, and Jia Zhou<sup>1</sup>

<sup>1</sup>ASIC and System State Key Laboratory, School of Microelectronics, Fudan University, Shanghai 200433, China

E-mail: , URL: <http://homepage.fudan.edu.cn/ariaud/>

### Introduction

Contact angle hysteresis makes the difference between slippery and sticky surface. It originates from inhomogeneities on the surface energy landscape such as chemical impurities [1]. Besides chemistry, electric fields are also known to alter the energy landscape, as brilliantly demonstrated by the spreading of droplets of charged surfaces, namely the electrowetting effect. Given this ability, it is natural to expect that electric fields can also alter the contact angle hysteresis. However, multiple studies from the electrowetting community suggest that electric fields either do not increase the contact angle hysteresis [2], and may even reduce it [3].

We report experimental measurements of the contact angle hysteresis under various voltages applied to an interdigitated electrodes-based electrowetting system. In agreement with contact angle hysteresis thermodynamic theory, we show that inhomogeneous electric fields do increase the contact angle hysteresis. These observations are interpreted with an analytical model that quantitatively match the experimental data with no fitting parameters.

### Experimental setup

The experimental setup, shown in Fig. 1.a, is similar to the interdigitated electrodes previously used by McHale *et al.*[2]. A 40  $\mu\text{L}$  droplet of deionized (DI) water placed on an electrowetting chip is inflated or deflated by a syringe pump connected to an electrically floating needle tip. Addition and removal of liquid are performed at constant electric voltage  $U_0$  between the electrodes, and the contact angle is measured using a goniometer. The onset of droplet motion upon deflation and inflation are recorded as receding and advancing contact angles, respectively.

Even in the absence of voltage, the droplet exhibits a small contact angle hysteresis. In the following, we offset this contribution by measuring  $d \cos(\theta_i) = \cos(\theta_i)(U_0) - \cos(\theta_i)(U_0 = 0)$ , with  $i = A$  or  $R$  for the advancing and receding angle respectively.

### Physical model.

For the sake of simplicity, we first demonstrate the electrowetting effect while minimizing the contribution of the contact angle hysteresis. Hence, we consider  $d \cos(\theta_R) + d \cos(\theta_A)$ , which subtracts the opposite contributions of the hysteresis in advancing and receding angles (Fig. 2.a). Similarly to the classical electrowetting effect[2], the contact angle decreases for an increasing electrical voltage (cosine is a decreasing function on the considered interval). Next, we consider the contact angle hysteresis for a range of voltages. This is best visualized by  $d \cos(\theta_R) - d \cos(\theta_A)$ , which subtracts the average change in contact angle due to the electrowetting effect while adding up the contributions of the contact angle hysteresis from the advancing and receding angles (Fig. 2.b). The cloud of points represents individual measurements carried out at each different voltages. It appears that the contact

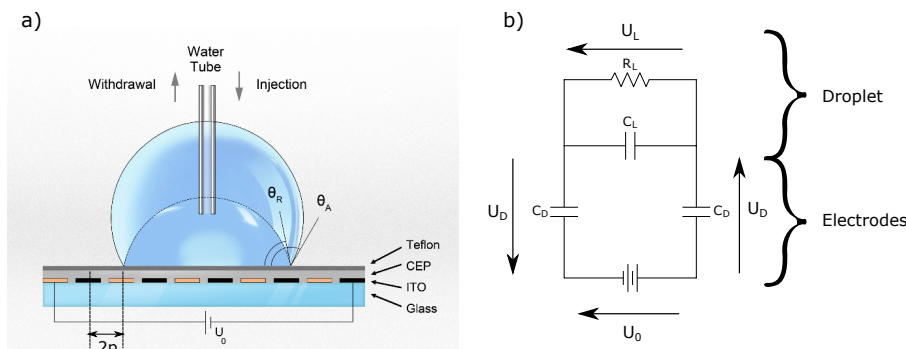


**Figure 1:** Experimental setup. (a) Overview of the experimental system. A DI water droplet is positioned on an interdigitated electrodes. The droplet is inflated/deflated at constant voltage while measuring the contact angle. (b) Equivalent electrical circuit. The CEP and Teflon are modeled as a pair of capacitors  $C_D$  while water is modeled by a capacitor and a resistor in parallel.

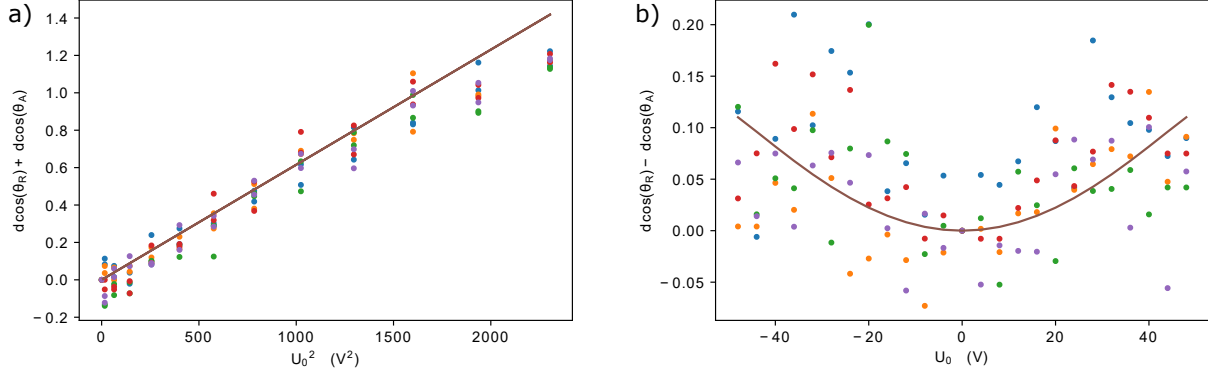


**Figure 2:** Contact angle variation at various electric fields. (a) Classical electrowetting effect (reduction of the contact angle for increasing actuation voltage). (b) electrowetting-induced contact angle hysteresis. Points are experimental measurements and solid lines are from Eq. (1).

angle hysteresis is indeed modified by the growing actuation voltage.

Starting from the equivalent circuit shown in Fig. 1.b and thermodynamic considerations, we derived a generalized Young-Lippmann equation to explain these observations:

$$\cos \theta_A(U_0 = 0) + \frac{1}{16} \frac{C_D U_0^2}{\gamma} - \frac{B}{16} \frac{C_D U_0^2}{\gamma} \leq \cos \theta \leq \cos \theta_R(U_0 = 0) + \frac{1}{16} \frac{C_D U_0^2}{\gamma} + \frac{B}{16} \frac{C_D U_0^2}{\gamma}, \quad (1)$$

$$B = \frac{4 - \sqrt{2}}{\pi^2} \zeta \left( \frac{3}{2} \right) \sqrt{\frac{p}{R}}, \quad (2)$$

with  $C_D$  the dielectric layer capacitance,  $R$  the droplet radius,  $p$  the electrode gap and  $\zeta$  the Riemann zeta function. Eq. (1) indicates that the contact angle is bounded by two extreme values, which are the advancing (left) and receding (right) contact angles. Each of those angles is the sum of three contributions: (i) natural contact angle at  $U_0 = 0$ , (ii) symmetric electrowetting contribution responsible for the reduction of the contact angle as shown in figure Fig. 2.a, (iii) antisymmetric contribution responsible for the electrowetting-induced contact angle hysteresis shown in Fig. 2.b. In both figures, the model predictions (without fitting parameters) agree well with experimental data as shown by the solid lines. Furthermore, Eq. (2) indicates that the contact angle hysteresis depends on the ratio between the droplet radius and the electrode gap. Hence, unlike the microscopic electrodes presented here, nanometric inhomogeneous electric fields such as the local polarization of ionic crystals should have a negligible influence on the contact angle hysteresis of macroscopic droplets.

## Conclusion

We have observed the contact angle hysteresis generated by an inhomogeneous electric field. To the best of our knowledge, it is the first demonstration that electrostatic fields can modify the contact angle hysteresis without considering visco-inertial effects. The analytical model accurately captures the contact angle hysteresis variation with the electric field. We are excited to share these findings and receive expert insights from the CMiF community.

## References

- [1] P.-G. De Gennes, "Wetting: statics and dynamics," *Reviews of modern physics*, vol. 57, no. 3, p. 827, 1985.
- [2] G. McHale, C. Brown, M. Newton, G. Wells, and N. Sampara, "Dielectrowetting driven spreading of droplets," *Physical review letters*, vol. 107, no. 18, p. 186101, 2011.
- [3] F. Li and F. Mugele, "How to make sticky surfaces slippery: Contact angle hysteresis in electrowetting with alternating voltage," *Applied Physics Letters*, vol. 92, no. 24, p. 244108, 2008.



## Drinking with an elastic strip

Joachim Delannoy<sup>1,2</sup>, Thierry Lengagne<sup>3</sup>, Christophe Clanet<sup>1,2</sup> & David Quéré<sup>1,2</sup>

<sup>1</sup> Physique & Mécanique des Milieux Hétérogènes, UMR 7636, ESPCI, 75005 Paris, France

<sup>2</sup> LadHyX, École polytechnique, UMR 7646, 91128 Palaiseau, France

<sup>3</sup> LEHNA, Université Lyon 1, UMR 5023, 69622 Villeurbanne, France

E-mail: joachim.delannoy@espci.fr, URL: <https://blog.espci.fr/interfaces/>

### Introduction

If hummingbirds' wings beat at 60 strokes per seconds, it is not only to parade with their acrobatic flight abilities, but also because it enables them to hover above flowers for harvesting nectar. This process is energy consuming, which forces hummingbirds to achieve efficient ways to drink the viscous nectar. While other birds fill their beak and then tilt the head to let liquid flow, hummingbirds rather use their tongue to drink. We investigate this unique feeding technique by direct observation of a hummingbird's tongue during harvesting.

### Hummingbird's feeding technic

We first observe how nectar is trapped into the tongue during a feeding cycle with a high-speed camera. We show in Fig.1 an overview of the experiment, where a hummingbird is harvesting an artificial nectar, consisting of 160 g of sucrose per litre of water, from a transparent feeder designed to observe the process.

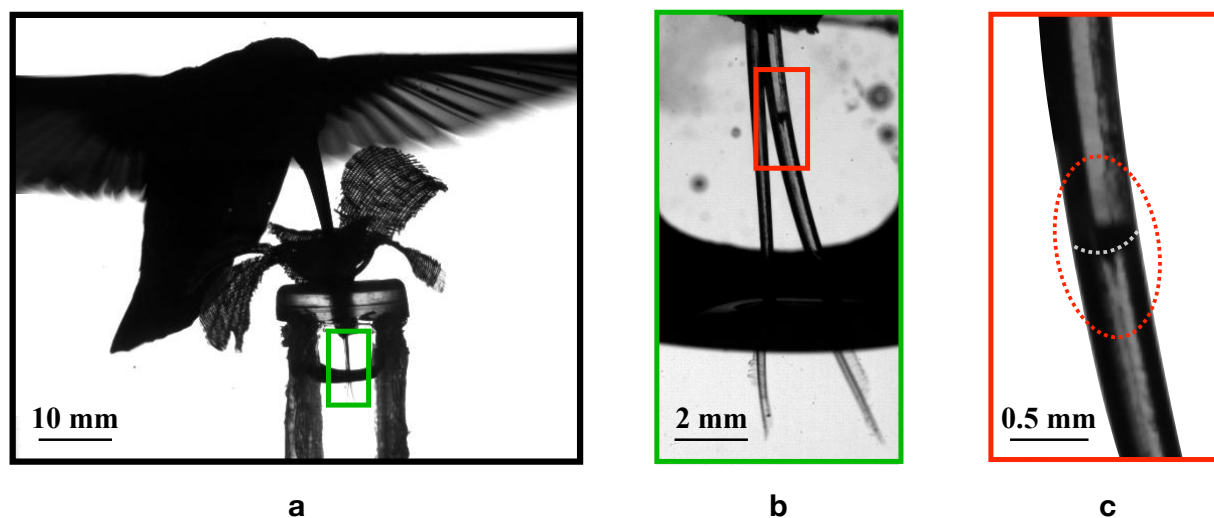


**Figure 1.** **a** Picture of a hummingbird harvesting a sucrose solution (160g/L). The beak tip is blocked 9 mm above the feeder aperture. The green frame indicates the acquisition field of the camera that was used to zoom on the tongue. **b** Emphasis on the nectar capture. We distinguished the two tines of the two-forked tongue plunging into the nectar below the millimetre-size meniscus (black) that hides a part of it. The right tine opening faces the camera, showing us distinctly the nectar rise and the tongue deformation. **c** Zoom on the liquid front in the tongue corresponding to the framed part in (b). We stress more particularly the tongue is reshaped: the photo shows the transition zone between the closed and open part of the tongue, below and above the liquid front (whose position is stressed with white dots).

The two-forked tongue, which was studied in [1], is plunged into the liquid for about 40 ms at a velocity of approximately 30 cm/s. The liquid meniscus rises a short time after contact, while the tongue is still deepening into the liquid bath, suggesting a capillary mechanism that was also reported in [2]. In addition, we see that the nectar deforms the tine while rising (Fig.1c), an interesting feature that we reproduce and model in our study.

## Liquid capture with elastic strips

To investigate the feeding technic, we mimic hummingbirds' tongue with thin, deformable, hemi-cylindrical membrane. We plunge the membranes at a velocity  $V$  in a bath of soapy water and observe how the wetting liquid interacts with the elastic strip. The process is presented in Fig.2.

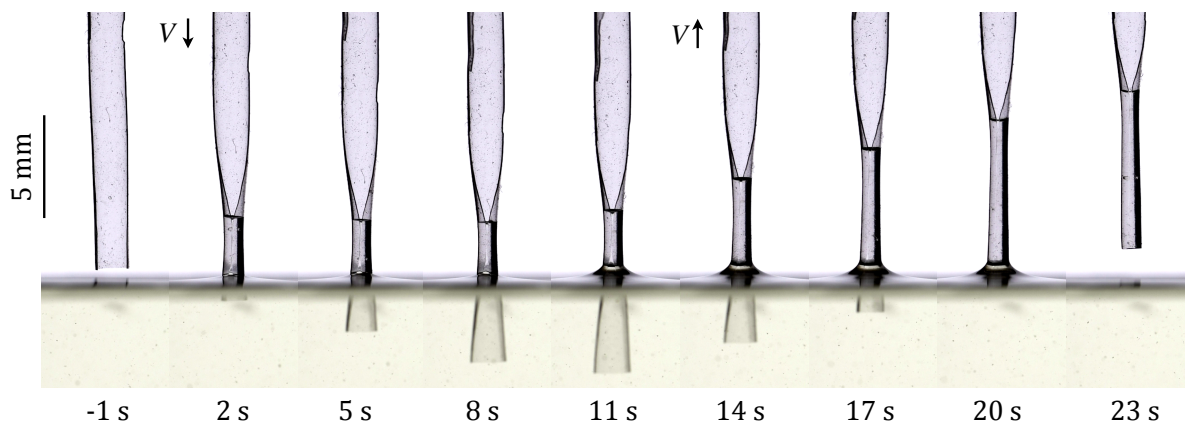


**Figure 2.** Replication of a drinking cycle of a hummingbird with an elastic strip with width 2.5 mm, thickness 45  $\mu\text{m}$ , and Young's modulus 200 kPa. The strip is first plunged at a velocity  $V = 0.6$  mm/s in a bath of soapy water, a phase during which the height of the liquid front plateaus at approximately 3 mm; in a second phase, the tongue is withdrawn of the bath at  $V = 0.6$  mm/s, which allows the system to entrain about twice more liquid than in the first phase. The height of the capture column is about 7.7 mm. Intervals between successive images is 3 s.

Shortly after contact, the liquid rises in the membrane and 'zips' the strip while the part of the membrane plunged into the bath reopens – a feature also observed in Fig.1b. Finally, as we retract the strip out of the bath, the lower part of the membrane closes and captures a quantity of liquid that we can measure. With our biomimetic device, we investigate and model how the membrane elasticity, thinness and velocity influences the quantity of liquid captured in the strip.

## Conclusion

We show that hummingbirds use their tongues not only as a capillary pump but also as an elastic trap to capture liquid. In addition, our artificial device allows us to characterize the details of the capture, specifically how the tongue withdrawal allows the birds to harvest more liquid – a rare case where contact angle hysteresis is turned in an advantage.

## References

- [1] A. Rico-Guevara, PeerJ, **5**, e3449 (2017).
- [2] W. Kim, F. Peaudcerf, J.W.M. Bush. Proc. R. Soc. B, **279**, 4990-4996 (2012).



## Study of a vortex free-surface instability maintained by a Marangoni flow.

Gabriel Le Doudic<sup>1</sup>, Matthieu Labousse<sup>2</sup>, Isabelle Cantat<sup>3</sup>, Arnaud Saint Jalmes<sup>3</sup>, Corentin Tregouet<sup>3</sup>, Stéphane Perrard<sup>4</sup>, Matthieu Roché<sup>1</sup>

<sup>1</sup>Matière et Systèmes Complexes, Université Paris-Diderot, Paris, FRANCE

E-mail: [gabriel.le-doudic@univ-paris-diderot.fr](mailto:gabriel.le-doudic@univ-paris-diderot.fr), URL: <http://www.fysik.dtu.dk/CMiF2019>

<sup>2</sup>ESPCI, Université Paris-Sciences-et-Lettres, Paris, FRANCE

<sup>3</sup>Institut de Physique de Rennes, Université de Rennes, Rennes, FRANCE

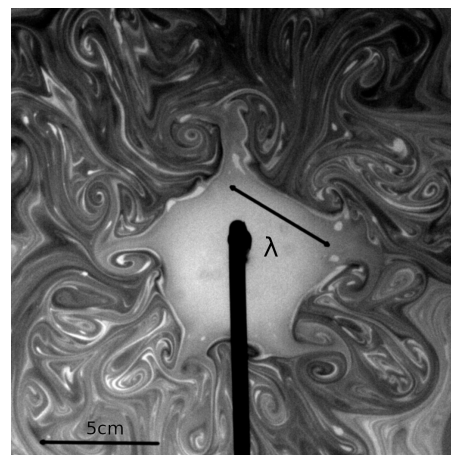
<sup>4</sup>Laboratoire de Physique de l'ENS, Paris, FRANCE

### Introduction

A local deposition of a soluble surfactant solution on a water layer creates a surface tension difference. The generated gradient of surface tension sets in motion the fluid on each side of the interface. This effect is called the solutal Marangoni effect. When the surfactant solution is injected continuously on the water a Marangoni flow of finite size  $R_M$  results.  $R_M$  increases with the injection flow rate  $Q$  and with the decrease of the cmc (the critical micellar concentration *i.e.* the concentration at which the surfactant self-assemble in water) [1,2]. Then we can observe the creation of a toroidal vortex below the surface of the water and pairs of 2D swirling structures around the Marangoni flow. Thus, the Marangoni flow offers the opportunity to investigate the interaction between vortices and a free interface. The aim of this study is to understand the generation of geometric shapes (Fig. 1) linked to the toroidal vortex below the surface of water (Fig. 2.(b)) and to the emission of vortices at the surface (Fig. 1).



(a) Squared Marangoni flow,  $h = 15$  mm,  $Q = 0.74 \mu\text{mol.s}^{-1}$ .



(b) Pentagonal Marangoni flow,  $h = 15$  mm,  $Q = 1.16 \mu\text{mol.s}^{-1}$ .

**Figure 1:** We inject the foam made of 60% of oil and 40% of surfactant solution at the the surface of the water tank. After 30 seconds we get the stationnary Marangoni flow. With given initial condition of flow rate and height of water in the tank the flow take geometrical configurations: (a) a square, (b) a pentagone. These are instantaneous photos taken with a camera above the tank.

### The Marangoni flow and its surface vortices

We create a Marangoni flow by injecting an aqueous solution of surfactant tetradecyltrimethylammonium bromide (TTAB, concentration  $c = 0.2 \text{ mol.L}^{-1}$ ) at constant flow rate  $0.2 < Qa < 2 \mu\text{mol.s}^{-1}$  at the surface of a water layer contained in a tank. When the Marangoni effect starts, it creates a radial surface flow from the point of injection outwards with a velocity  $U_S \approx 0.1 \text{ m.s}^{-1}$  over a finite distance  $R_M$  (Fig.2(a)). At  $R_M$  the surface velocity decreases abruptly by more than one order of magnitude. We characterise the flow field inside the water layer using 3D particle image velocimetry (PIV) and we observe the existence of a vortex ring (Fig.2 (b)). This vortex ring is strong enough to deform the free

interface. Measurements performed using free-surface Synthetic Schlieren profilometry (FS-SS) shows that the vortex ring induces a deformation of the air/water interface, similar to a scar (Fig.2.(a)). The scar has an average depth of several tens  $\mu\text{m}$ . Starting from the base state troughs and crests grow along the perimeter. They reach a maximum and then relax to the base state again. The relaxation is accompanied by the emission from the troughs pairs of surface depressions with a depths comparable to that of the polygon.

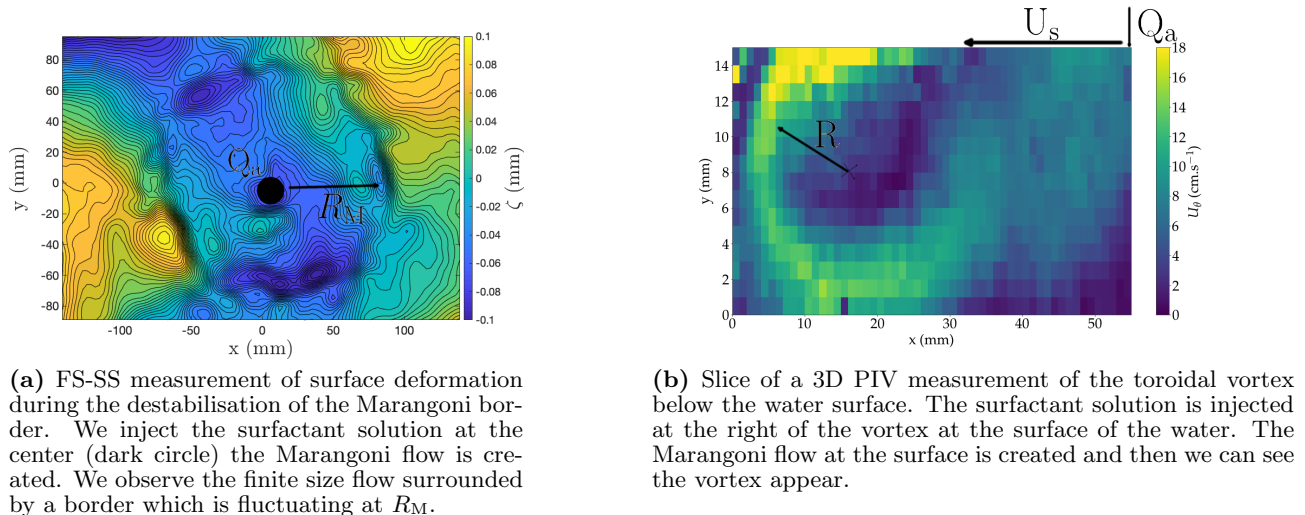


**Figure 2:** Coupling between surface deformation and the toroidal vortex below the surface.

A top view of the flow with tracers dispersed in the surfactant solution indicates that these dimples are associated to the whirl pairs emitted from the vortices of the polygon. It provides a direct measurement of the emission time  $t_w$ . We also use the direct visualisation to characterise the dependance of  $\lambda$  on both the molar flow rate  $Q_a$  and the initial thickness  $h$  of the water layer.

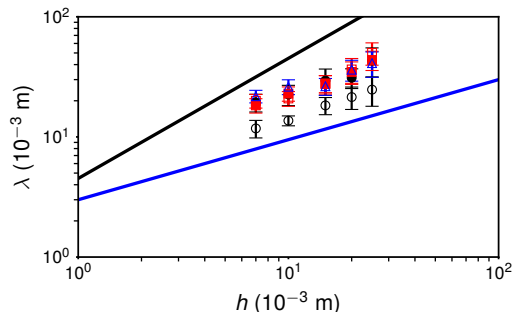


**Figure 3:** Dependence of the wavelength  $\lambda$  compared to the height of water, (—) scaling with a slope of 1, (—) scaling with a slope of  $\frac{1}{2}$

The wavelength of the instability scales in  $\sqrt{h}$ , with  $h$  the depth of the water layer. This scaling differ from the litterature on the elliptical instabilities which are porportional to  $R$  the radius of the vortex. These results will be discussed in the light of the litterature on interaction between fluid/fluid interfaces and vortices [3].

## Conclusion

We have the opportunity to study a solutocapillary flow that generates very beautiful geometric shapes which are the consequence of the interaction between a vortex ring and a free surface. I am looking forward to present and discuss our work at the summer school *Complex Motion in Fluids 2019* at Kysthusene, near Gilleleje, Denmark, on 18 - 24 August 2019.

## References

- [1] M. Roché, Z. Li, I. M. Griffiths, S. Le Roux, I. Cantat, A. Saint-Jalmes, H. A. Stone. *Physics of Fluids* **25**, 091108 (2013).
- [2] S. Le Roux, M. Roché, I. Cantat, A. Saint-Jalmes. *Physical Review E* (2016).
- [3] Douglas G. Dommermuth, Dick K.P. Yue. *Eighteen symposium on Naval hydrodynamics*, (1990).



## Jetting in axisymmetric surface-gravity waves

Saswata Basak<sup>1</sup> and Ratul Dasgupta<sup>1</sup>

<sup>1</sup>Department of Chemical Engineering, Indian Institute of Technology Bombay, Mumbai, India  
E-mail: [dasgupta.ratul@gmail.com](mailto:dasgupta.ratul@gmail.com)

### Introduction

The phenomenon of jetting and accompanying droplet ejection is known to occur in many fluid dynamical situations involving collapse of a gaseous cavity at a liquid-gas interface [1]. In a recent study of free, capillary-gravity oscillations on a quiescent cylindrical pool of liquid [2], it has been shown using Direct Numerical Simulations (DNS) that jetting may be obtained with an initial interfacial perturbation taken to be a Bessel mode (primary mode) of the form  $\eta(r, 0) = a_0 J_0(l_p r/R_0)$  with  $R_0$  being the radius of the domain (see definition of  $l_p$  below). For sufficiently large values of  $\epsilon \equiv a_0 l_p/R_0$ , it was found that waves at the interface produce a jet at the axis of symmetry which can eject droplets from its tip. It was shown in [2] that this jetting is a nonlinear phenomena involving the generation of higher modes and energy to these. We present here, a weakly nonlinear, irrotational, inviscid theory which is able to capture the initiation of jetting and shows the energy transfer to the higher modes.

### Formulation of a weakly nonlinear initial-value problem

The process of incipient jetting coincides temporally with the appearance of higher harmonics of the primary mode [2]. In order to understand this transfer of energy, we solve the nonlinear, inviscid-irrotational, *initial-value problem* using  $\epsilon$  as a small parameter upto  $\mathcal{O}(\epsilon^3)$ , for surface-gravity waves (neglecting capillary effects) in axisymmetric cylindrical coordinates. Our calculation uses the Dini series expansion [3] for the Laplace equation and the Poincaré-Lindstedt method [4] to eliminate secular terms and builds upon a similar weakly nonlinear calculation by [5]. Presently, our calculation has been done assuming a radially bounded system. In terms of non-dimensional variables upto  $\mathcal{O}(\epsilon^3)$ , it is found that the perturbed free surface at time,  $t$  has the following form,

$$\begin{aligned} \eta(r, t) = & \epsilon \cos(\omega_p t) J_0(r) + \epsilon^2 \sum_{j=0}^{\infty} \left[ A^{(j)} + B^{(j)} \cos(2\omega_p t) + C^{(j)} \cos(\omega_j t) \right] J_0\left(\frac{l_j}{l_p} r\right) + \\ & \epsilon^3 \sum_{j=0}^{\infty} \left[ D^{(j)} \cos(\omega_p t) + E^{(j)} \cos(3\omega_p t) + \sum_{m=1}^{\infty} \left\{ F_m^{(j)} \cos[(\omega_m + \omega_p) t] + \right. \right. \\ & \left. \left. G_m^{(j)} \cos[(\omega_m - \omega_p) t] \right\} + H^{(j)} \cos(\omega_j t) \right] J_0\left(\frac{l_j}{l_p} r\right) + \mathcal{O}(\epsilon^4) \end{aligned} \quad (1)$$

where  $\omega_p \equiv 1 + \epsilon^2 \mathcal{K}[l_0, l_1, l_2, \dots, R_0]$ ,  $\omega_j \equiv \sqrt{\frac{l_j}{l_p}} (1 + \epsilon^2 \mathcal{K}[l_0, l_1, l_2, \dots, R_0])$  while  $\{l_p\}$  is the set of zeroes of the Bessel function,  $J_1(\cdot)$  with  $q = 1, 2, 3, \dots$  and  $\mathcal{K}$  being a (complicated) function of its arguments involving integral over products of Bessel functions. The coefficients  $A^{(j)}, B^{(j)}$ , etc. in (1) have lengthy expressions and are not provided here.

### Comparison with DNS

Comparison of analytical results from expression (1) truncated at  $\mathcal{O}(\epsilon)$  (linear) and the full expression (weakly nonlinear) to DNS (axisymmetric) obtained using the open-source code Basilisk [6] is shown in Figure 1 (next page). For DNS, the parameters are (in CGS units)  $l_q = 25.90367$ ,  $g = 981$ , (density of gas)  $\rho_g = 10^{-3}$ , (density of liquid)  $\rho_l = 1.0$ ,  $R_0 = 8$  and  $a_0 = 0.1853$ . For expression (1), the density of gas is taken to be zero while all other parameters have the same value as DNS. An uniform grid of  $512 \times 512$  with undisturbed fluid depth of 5 has been used in DNS. The figure shows that the complete expression (1) is able to predict the onset of jetting. However, expression (1) when truncated at linear order is unable to do so.

### Conclusion

We present a weakly nonlinear inviscid theory which solves the initial value problem for a single Bessel mode and captures the onset of jetting and energy transfer to higher modes. A more detailed calculation including capillary effects will be presented in the summer school including further comparisons with Direct Numerical Simulations of the Navier-Stokes equations.

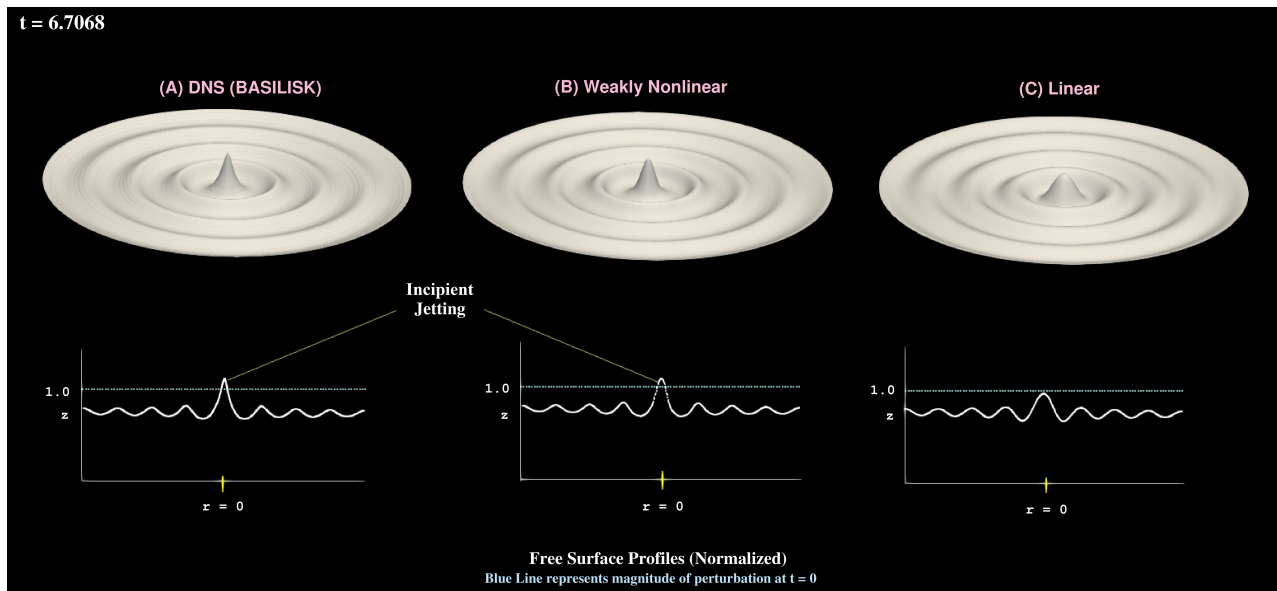


**Figure 1:** Comparison of (a) axisymmetric DNS (b) weakly nonlinear theory and (c) linear theory. (Lower panel) Instantaneous snapshot of the interface on the  $r$ - $z$  plane at  $t = 6.7068$  from (a) DNS (b) Expression (1) (c) Expression (1) truncated to  $\mathcal{O}(\epsilon)$ . (Upper panel) Three dimensional visualisation of the lower panel images.

## References

- [1] Veron, Fabrice. “Ocean spray”, *Ann. Rev. Fluid Mech.* 47 (2015): 507-538.
- [2] Farsoiyya, Palas Kumar, Y. S. Mayya, and Ratul Dasgupta. “Axisymmetric viscous interfacial oscillations-theory and simulations” *J. Fluid Mech.* 826 (2017): 797-818.
- [3] Mack, Lawrence R. “Periodic, finite-amplitude, axisymmetric gravity waves.” *J. Geophys. Res.* 67.2 (1962): 829-843.
- [4] Nayfeh, Ali H. *Perturbation methods*. John Wiley & Sons, 2008.
- [5] Jacobs, J. W., and I. Catton. “Three-dimensional Rayleigh-Taylor instability Part 1. Weakly nonlinear theory.” *J. Fluid Mech.* 187 (1988): 329-352.
- [6] Basilisk, Popinet, Stephane, 2014, <http://basilisk.fr>.



## General Defocusing Particle Tracking - Part I: Theoretical background

Massimiliano Rossi<sup>1</sup> and Rune Barnkob<sup>2</sup>

<sup>1</sup>Department of Physics, Technical University of Denmark, Kongens Lyngby, Denmark  
E-mail: [rossi@fysik.dtu.dk](mailto:rossi@fysik.dtu.dk), URL: [www.staff.dtu.dk/rossi](http://www.staff.dtu.dk/rossi)

<sup>2</sup>Heinz-Nixdorf-Chair of Biomedical Electronics, Department of Electrical and Computer Engineering, Technical University of Munich, Munich, Germany

General Defocusing Particle Tracking (GDPT) is a single-camera method to track in time and space the 3D position of small particles dispersed in a fluid [1]. The physical background behind this method is that images of particles that are out of focus show distinct patterns depending on the axial distance of the particles from the lens. GDPT uses a look-up table approach to match the defocusing patterns with the corresponding axial coordinates of the particles. We assume here a coordinate system where  $x$  and  $y$  are the coordinates perpendicular to the optical axis of the lens, and  $z$  is the coordinate parallel to the optical axis (Fig. 1). In this contribution, we will revise and discuss the basic concepts in optics and particle tracking that are needed to understand and apply the GDPT method.

Firstly, a brief review and history of velocimetry methods based on particle tracking will be presented, and basic concepts like difference between Particle Image Velocimetry (PIV) and Particle Tracking Velocimetry (PTV) will be revised. Secondly, the main components of a defocusing particle tracking system will be analyzed, including objective lenses, tracer particles, digital image acquisition and processing, illumination sources. Afterwards, the theoretical background of defocusing imaging and astigmatic imaging will be explained. Astigmatism is an optical aberration that can be used to enhance the efficiency of the defocusing information by breaking the symmetry of the optical system [2]. Finally, examples of experimental and synthetic defocused particle images will be provided.

The working principle of GDPT and its application on real cases will be presented in the following-up contribution.

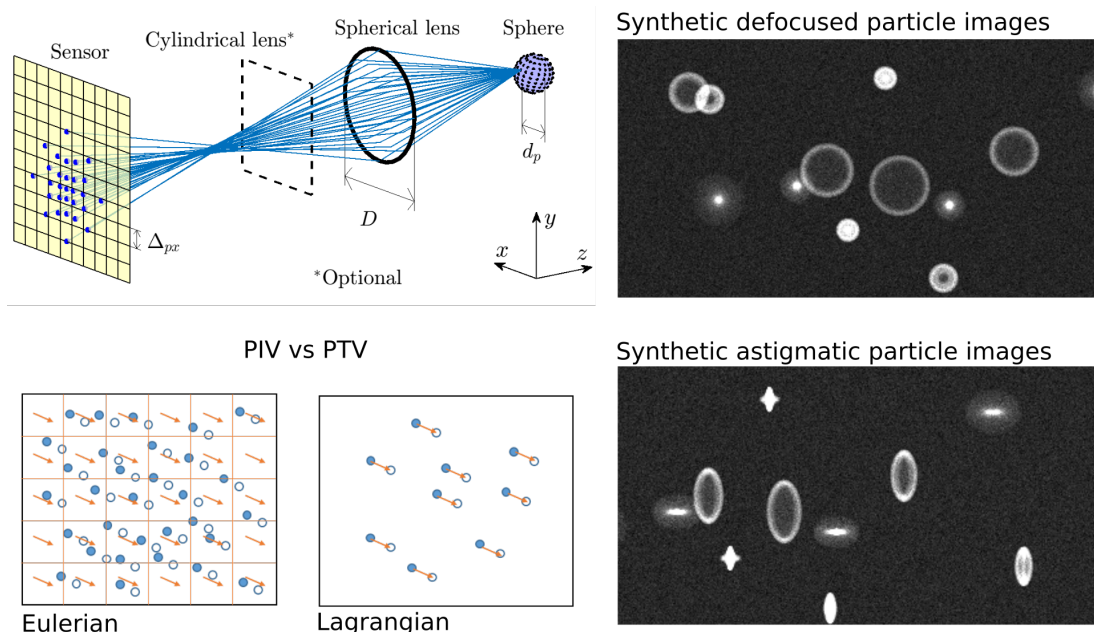


**Figure 1:** (Top-left) Schematic of an optical system used for defocusing or astigmatic 3D particle tracking. (Right) Example of defocused and astigmatic particle images obtained with a synthetic particle image generator [3]. (Bottom-left) Illustration of the basic idea behind PIV and PTV approaches.

### References

- [1] R. Barnkob, C.J. Kähler, and M. Rossi. Lab on a Chip **15**, 3556-3560 (2015).
- [2] M. Rossi, and C.J. Kähler. Experiments in Fluids **55**, 1809 (2014).
- [3] M. Rossi. Synthetic image generator for defocusing and astigmatic PIV/PTV, *Submitted*.





## General Defocusing Particle Tracking - Part II: Working principle and applications

Rune Barnkob<sup>1</sup> and Massimiliano Rossi<sup>2</sup>

<sup>1</sup>Heinz-Nixdorf-Chair of Biomedical Electronics, Department of Electrical and Computer Engineering, Technical University of Munich, Munich, Germany

E-mail: [rune.barnkob@tum.de](mailto:rune.barnkob@tum.de), URL: <http://www.lbe.ei.tum.de>

<sup>2</sup>Department of Physics, Technical University of Denmark, Kongens Lyngby, Denmark

In this contribution we outline and discuss the basic working principles, advantages, and microfluidic applications of the General Defocusing Particle Tracking (GDPT). An introduction to the basic theory and concepts in defocusing particle tracking will be given in the contribution *General Defocusing Particle Tracking - Part I: Theoretical background*.

GDPT is a single-camera method to track in time and space the 3D position of small particles dispersed in a fluid [1]. The physical background behind this method is that images of particles that are out of focus show distinct patterns depending on the axial distance of the particles from the lens. GDPT uses a look-up table approach to match the defocusing patterns with the axial ( $z$ -position) of the particles. We assume here a coordinate system where  $x$  and  $y$  are the coordinates perpendicular to the optical axis of the lens, and  $z$  is the coordinate parallel to the optical axis (Fig. 1).

We discuss the GDPT working principle with emphasis on understanding the calibration stack and the resulting measurement volume. In comparison to other 3D particle tracking methods, we outline GDPT's advantages, which include (i) being applicable to defocused particle images of any shape, (ii) requiring only standard microfluidics equipment, (iii) being easy-to-use for non-velocimetry experts, (iv) being robust against outliers and overlapping particles, and (v) holding the potential for expansion for use on non-spherical and non-monodisperse particle suspensions, such as cell suspensions. Furthermore, the quality and reliability of GDPT can easily be controlled by one single parameter, namely the magnitude of the normalized cross-correlation peak. We show a selection of microfluidic applications including the use for tracking living cells. Finally, we introduce GDPTlab, which is an open-access and ready-to-use Matlab implementation, which is currently receiving increasing attention in the microfluidics research community [2].

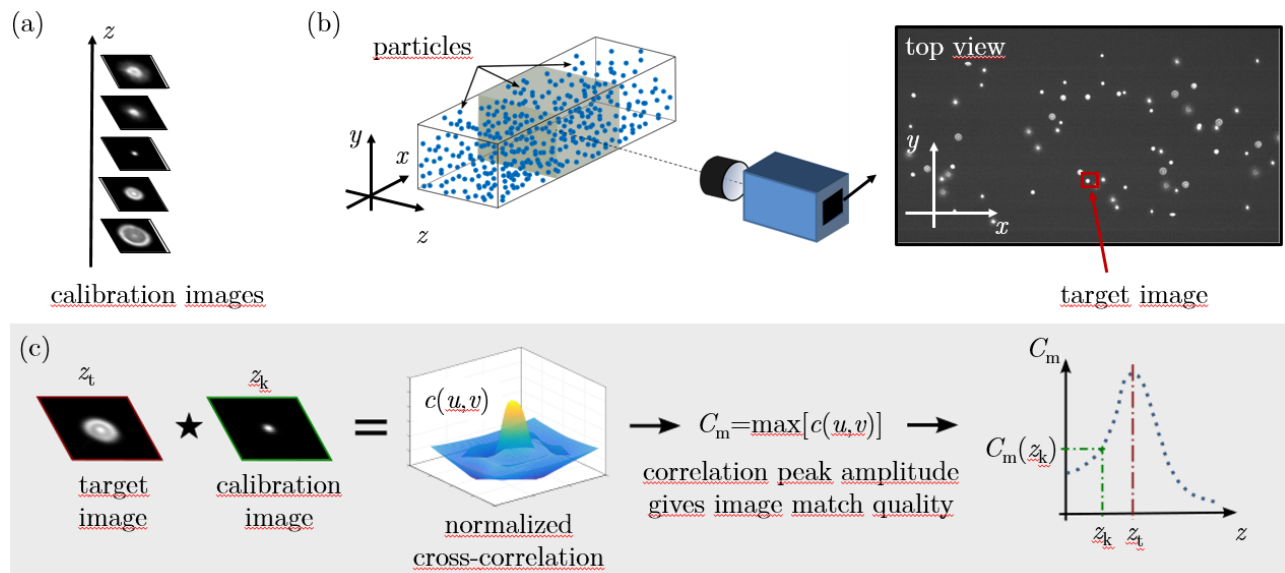


**Figure 1:** Working principle of the General Defocusing Particle Tracking (GDPT), which relies on having a (a) set of calibration images, which correlates the defocused particle images with their out-of-plane  $z$ -position in a (b) volume-illuminated single-camera measurement. (c) GDPT based on the normalized cross-correlation.

### References

- [1] R. Barnkob, C.J. Kähler, and M. Rossi. Lab on a Chip **15**, 3556-3560 (2015).
- [2] R. Barnkob and M. Rossi. Workshop on "How to do 3D microparticle tracking in microfluidics", MicroTAS 2018, Kaohsiung, Taiwan, (2018).





## Fluid manipulation in microfluidics using acoustic body force

Wei Qiu<sup>1,2</sup>, Jason P. Beech<sup>3</sup>, Jonas O. Tegenfeldt<sup>3</sup>, Henrik Bruus<sup>2</sup>, and Per Augustsson<sup>1</sup>

<sup>1</sup>Department of Biomedical Engineering, Lund University, Lund, Sweden

E-mail: wei.qiu@bme.lth.se, URL: <http://bme.lth.se/research-pages/nanobiotechnology-and-lab-on-a-chip/>

<sup>2</sup>Department of Physics, Technical University of Denmark, Kongens Lyngby, Denmark

<sup>3</sup>Division of Solid State Physics and NanoLund, Lund University, Lund, Sweden

### Introduction

Inhomogeneities in density and speed of sound between miscible aqueous solutions in microscale acoustofluidic devices induce an acoustic body force  $\mathbf{f}_{ac}$  acting on the fluids [1]. Several associated phenomena, e.g. fluid stabilization [2] and streaming suppression [3,4], lead to new approaches for bio-particle manipulation. A recent theoretical study predicts that  $\mathbf{f}_{ac}$  can be used to spatiotemporally pattern and manipulate concentration fields [5]. However, this concept has not been validated experimentally, mainly due to the difficulty in fast imaging in three dimensions. Here, using a new method of inclined confocal microscopy, the dynamics of fast fluid motion induced by  $\mathbf{f}_{ac}$  is captured in real time, and the patterning of concentration fields is validated.

### Materials and experimental methods

A standard silicon-glass chip with a 150- $\mu\text{m}$ -high and 375- $\mu\text{m}$ -wide long straight channel is used, under which two PZT transducers with different thicknesses are bonded side by side, see Fig. 1(a). The so-called  $n_y n_z$ -mode, is a standing wave with  $n_y$  and  $n_z$  half-waves in the horizontal and vertical direction, respectively. Driving the 1-mm-thick PZT at 1.94 MHz and 3.84 MHz excites the 10- and 20-modes, respectively, while the 0.4-mm-thick PZT run at 4.78 MHz excites the 01-mode. A laminated flow of two liquids is injected into the channel (Milli-Q water at the side and 10 wt% FITC labeled Ficoll PM400 at the center) to form a concentration gradient at a flow rate of 0.5  $\mu\text{L/s}$ .

To confirm the patterning of the concentration fields at each acoustic eigenmode, we first mapped the cross-section of the channel using a slow confocal microscopic unit equipped with a galvanometer mirror scanner. The confocal scan started after the fluid patterning was stabilized, and the total scanning time for the whole cross-section was around 20 s for a step size in the depth coordinate  $z$  of 1  $\mu\text{m}$ . A sequential excitation of the eigenmodes (10  $\rightarrow$  01  $\rightarrow$  20) was controlled using LabVIEW to demonstrate the spatiotemporal patterning. Each eigenmode was actuated for less than 1 s, and the corresponding energy density for each mode was  $48.3 \pm 2.3$ ,  $16.6 \pm 1.3$ , and  $7.2 \pm 0.7$   $\text{J/m}^3$ , respectively. To capture the fast dynamics of fluid patterning, which is invariant in the length coordinate  $x$ , we propose the method of inclined confocal microscopy, wherein the channel is tilted by  $10^\circ$  and hence the focal plane crosses the whole channel depth, see Fig. 1(b). Performed with a 5000-rpm spinning disk confocal microscope, this technique enables fast imaging in  $z$  coordinate with a frame rate of 31

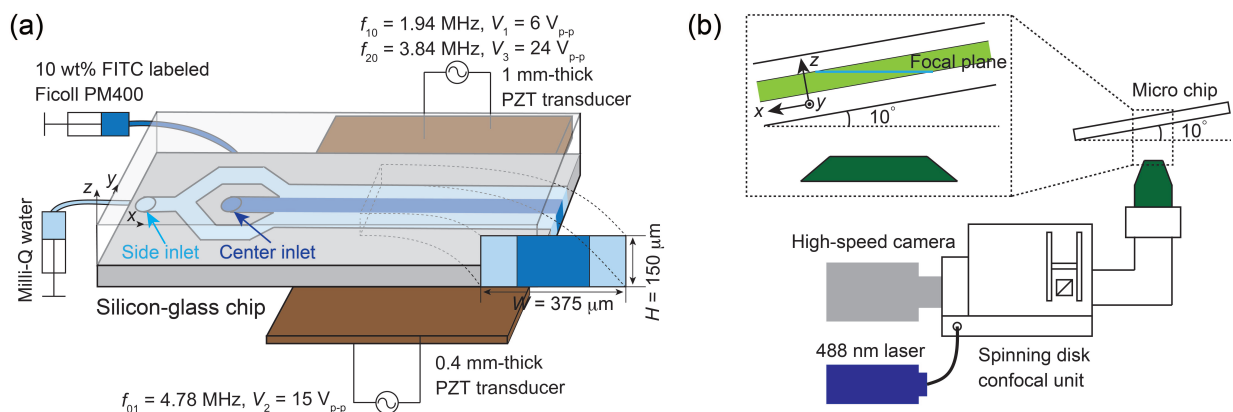


**Figure 1:** (a) Sketch of the silicon-glass chip with a rectangular-cross-section channel ( $W = 375 \mu\text{m}$ ,  $H = 150 \mu\text{m}$ ). A 10 wt% FITC labeled Ficoll PM400 solution (dark blue) is injected into the center and laminated by Milli-Q water (light blue). Two PZT transducers with different thickness (brown) are bonded on the bottom of the chip to generate three different modes. (b) Sketch of inclined confocal microscopy where the chip is tilted by  $10^\circ$ , and hence the focal plane crosses the whole channel depth. By integrating with a spinning disk confocal microscope, fast imaging in  $z$  coordinate is achieved.

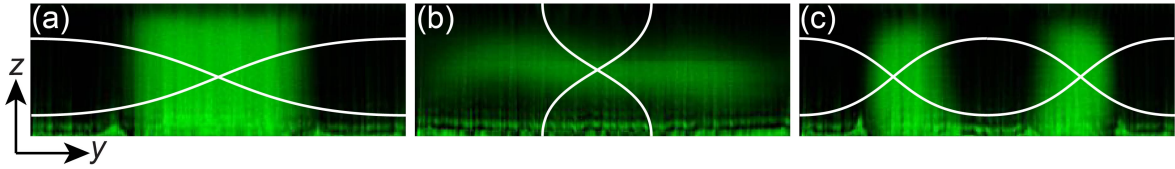


**Figure 2:** Conventional confocal microscopy. Patterning of concentration fields at (a) 10-, (b) 01-, and (c) 20-modes. The corresponding pressure field in each acoustic eigenmode is indicated by white lines. Images are acquired by slowly scanning the cross-section of the channel using confocal microscope.

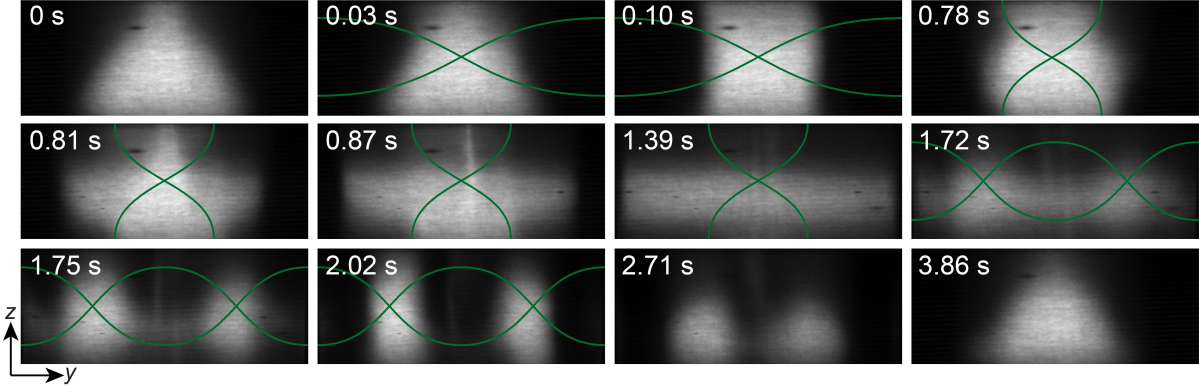


**Figure 3:** Real-time measurement of spatiotemporal patterning of concentration fields using inclined spinning disk confocal microscopy, which follows the sequence 00 (no acoustics)  $\rightarrow$  10  $\rightarrow$  01  $\rightarrow$  20  $\rightarrow$  00. The corresponding acoustic eigenmode at each frame is indicated by dark green lines. Video will be shown in the conference.

fps (higher frame rates are also feasible by sacrificing the spatial resolution).

## Results

We first investigated the patterning of concentration fields by slowly scanning the channel cross-section using scanning mirror confocal microscopy, see Fig. 2. It takes  $\sim 2$  s for the liquids to reach the observation region after being laminated, and hence Ficoll solution (possessing higher density and speed of sound) collapses due to the gravity. After exciting each mode, the Ficoll solution relocates to the pressure minima in all three cases, which agrees with the theoretical expressions of  $f_{ac}$  in each mode [5]. Then, a spatiotemporal patterning of the concentration fields is performed by switching the modes in the sequence of 00 (no acoustics)  $\rightarrow$  10  $\rightarrow$  01  $\rightarrow$  20  $\rightarrow$  00, and its dynamic evolution is recorded in real time by the inclined spinning disk confocal microscopy, see Fig. 3. This sequence is chosen because theoretical study predicts that orthogonal relocation (from vertical layer to horizontal or vice versa) is the most effective way to pattern concentration fields. Starting from the initial condition at 0 s, the formation of the vertical layer in 10-mode is completed within 100 ms. When the acoustic field is switched to 01-mode, the vertical layer formed at 10-mode starts to relocate from its center, and the Ficoll solution layer is stretched until the horizontal layer covers the whole channel width. In both static and dynamic measurements, the center of the horizontal layer is below the channel mid-height, which is due to the relatively low acoustic energy at 01-mode which leads to that  $f_{ac}$  cannot completely lift Ficoll solution against gravity at the pressure minima. The completion of the switches from 10-mode to 01-mode and from 01-mode to 20-mode takes less than 300 ms, showing that the time for relocation induced by  $f_{ac}$  is in the order of hundred milliseconds and that the acoustic energy affects the relocation time.

## Conclusion

We have experimentally validated that concentration fields can be patterned and manipulated spatiotemporally by an inhomogeneity-induced acoustic body force  $f_{ac}$ . The newly proposed inclined confocal microscopy enables real-time imaging of fast fluid motion, which catches the dynamics of fluid relocation in the  $z$  coordinate. The obtained results have good agreement with theory, and the application of this novel approach for manipulating miscible fluids will be further explored.

## References

- [1] J. T. Karlsen, P. Augustsson, and H. Bruus. Phys. Rev. Lett. **117**, 114504 1-6 (2016).
- [2] P. Augustsson, J. T. Karlsen, H.-W. Su, H. Bruus, and J. Voldman. Nat. Commun. **7**, 11556 1-9 (2016).
- [3] J. T. Karlsen, W. Qiu, P. Augustsson, and H. Bruus. Phys. Rev. Lett. **120**, 054501 1-6 (2018).
- [4] W. Qiu, J. T. Karlsen, P. Augustsson, and H. Bruus. Phys. Rev. Appl. **11**, 024018 1-11 (2019).
- [5] J. T. Karlsen and H. Bruus. Phys. Rev. Appl. **7**, 034017 1-10 (2017).



## Miscible fluids patterning and displacement with acoustic tweezers

Udita U. Ghosh<sup>1</sup>, J-C. Geberdoen<sup>2</sup>, Jonas T. Karlsen<sup>3</sup>, Henrik Bruus<sup>3</sup> and Michael Baudoin<sup>4</sup>

<sup>1,4</sup>Univ. Lille, CNRS, Centrale Lille, ISEN, Univ. Valenciennes, UMR 8520-IEMN, International laboratory LIA/LICS, Lille, France; Email : [udita-uday.ghosh@iemn.fr](mailto:udita-uday.ghosh@iemn.fr) [michael.baudoin@univ-lille1.fr](mailto:michael.baudoin@univ-lille1.fr)

<sup>2</sup>SATT Nord, IEMN, Lille, France.

<sup>3</sup>Department of Physics, Technical University of Denmark

### Introduction

Microfluidic systems are now the ubiquitous choice for complex fluid and particle manipulation. Manipulation of fluid packets in the form of droplets wherein the fluid immiscible interface is strictly defined has developed into a sub-domain known as discrete or digital microfluidics. However, this active mode of manipulation fails for the interface of miscible fluids and control of solute concentration fields is the underlying basic requirement in bio-molecular processes that are the building blocks in mechanisms like cell signaling. Acoustical Tweezers [1] are a solution to manipulate such inhomogeneous fluid interfaces by cornering the disadvantage of deleterious heating offered by their close cousins, optical tweezers. The theoretical framework [2] for such inhomogeneous fluid flows under the action of imposed acoustic fields has been investigated recently. In particular, the fields generated by Bessel-function (zero and higher orders) acoustic vortices have been shown to possess capabilities of translation as well as relocation of fluid inhomogeneity in rectangular micro-channels. However, experimental demonstration of the same is still lacking.

In the present study, we demonstrate the experimental validation of the theoretical predictions wherein we employ acoustic tweezers to produce myriad concentration based miscible fluid patterns that are in tune with the applied acoustic energy field. More importantly, these operations are governed only by a single experimental parameter that is the applied acoustic energy or acoustic energy density.

### Theory

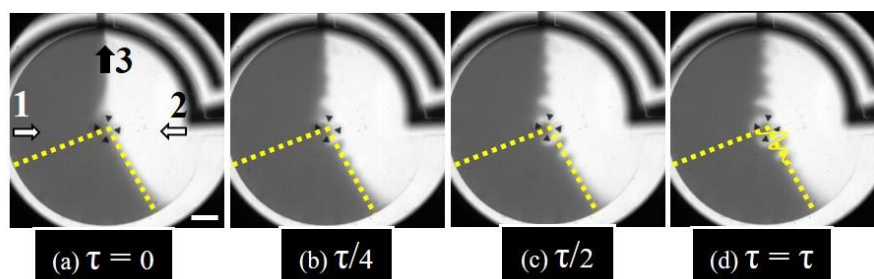
In the experiments that follow, we define an inhomogeneous fluid which has a dissolved solute that produces a quantifiable alteration in the localized fluid density and such spatial variations are reflected in the corresponding altered speed of sound through the fluid. Particularly, for the inhomogeneous fluids, the variation in density and compressibility leads to a non-zero divergence in the nonlinear momentum-flux-density tensor that arises in the second order of approximation which translates in to a variant overall acoustic force density. This acoustic force density can be related to the topology of the applied acoustic field as [3],

$f_{ac}^1 = E_{ac}^{(0)}[R(\vec{r}, \tau)\nabla\hat{\rho} + C(\vec{r}, \tau)\nabla\hat{c}] - eq(1)$  where  $R(\vec{r}, \tau)$  and  $C(\vec{r}, \tau)$  are the field shape functions and  $E_{ac}^{(0)}$  is the time averaged acoustic energy density for homogeneous fluids.

**Materials, methods and experimental procedure** Experimentally, the system comprises of acoustic tweezers that contain embedded spiraling metallic electrodes capable of producing focalized vortices of topological order 1 (Bessel order 1) when operated at frequency  $f = \omega/2\pi = 4.8$  MHz, 0dbm (driven by a function generator, AFG3022B, Tektronix, Inc., Beaverton, Oregon). Details of the fabrication of the acoustic tweezers can be found in a recent publication [1]. These tweezers are connected with a droplet of oil to a microchip containing a microchannel with two inlets, one each for the denser (Ficoll<sup>TM</sup>PM400, GE Healthcare, 50% (v/v) in de-ionized water Fig.1, inlet 1, 200-250 $\mu$ l/hr) and lighter fluid (deionized water, Millipore, Fig.1, inlet 2, 3-5  $\mu$ l/hr) and a single outlet (Fig.1, outlet 3). These two miscible fluids are then pumped into the microchannels using syringe pumps and the flowrates are optimized to obtain a clean and stable interface. At this juncture, the flow is stalled and the amplifier is activated to generate Bessel focalized acoustic vortices through the underlying acoustic tweezers and a camera (5 $\times$ , 1024 $\times$ 1024 resolution) attached to the microscope is used to capture (50 fps) the creation of the concentration pattern that resembles the Bessel pattern of order 1 embedded into the transducer structure. Care must be taken to place the marker at the interface of the two fluids. This ensures generation of the density-based gradient (equation 1) that causes an imbalance in the sound speed ( $\nabla\hat{c}$ ) and thereby drives the creation of the fluid patterns.

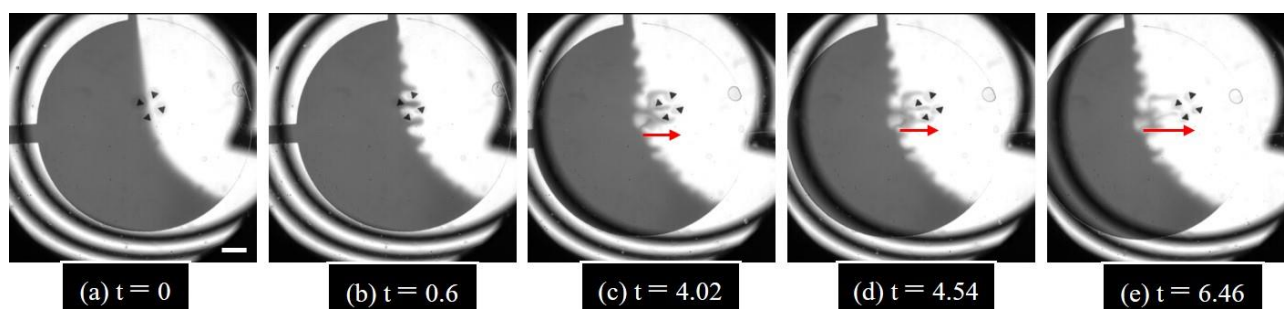
## Results and discussions

Fig.1 depicts the creation of a pattern and its temporal evolution by the manipulation of the concentration fields of the miscible fluids in presence of the Bessel-function acoustic vortex fields within the circular microfluidic chamber. These results pertain to the minimum actuation power for the designed acoustic tweezer. Panel (a) of Fig.1 indicates the instant when the tweezer is just actuated and the total time period for complete evolution of the pattern is denoted as  $\tau$ . It is evident that the pattern evolves with time at a fixed location with the denser fluid focused in the central region (Fig.1. panel (c)). This is in tune with theoretical prediction where in we know that for Bessel of orders greater than zero, the pressure minima lie in the center and thereof the central region acts as a trap for a fluid packet of higher density in a pair of fluids.



**Figure 1:** Temporal evolution (a-d) of the Bessel (order 1) pattern concentration field for minimum acoustic power (Gain = 0 of the driving amplifier) of the acoustic tweezer. The axes (in yellow, ----) indicate the growth of the Bessel pattern. 1- Inlets for Ficoll, denser fluid and deionized water are indicated as 1,2 respectively. 3 – channel outlet. Panel(d) also shows the expected field shape function  $R(\vec{r}, \tau)$  **Scale bar:** 1mm.

This trap has been further exploited to test the feasibility of spatial translation of such a trapped fluid packet from denser to lighter regions.



**Figure 2:** Feasibility of fluid translation using focalized acoustic Bessel vortices of orders greater than zero. **Scale bar:** 1mm.

Fig. 2 demonstrates a typical result of such an attempt where in panel (b) the creation of the trap is shown and the trapped fluid packet is translated (panels c-e) from the denser region into the lighter region. Panel (e) indicates that after a time interval, the effect of diffusion overtakes the externally applied acoustic field and the trap is broken. This implies that the parameters of rate of translation or translation speed, employed acoustic force and the rate of equimolar counter diffusion has to be optimized to obtain a stable trap capable of sustaining fluid translation.

## Conclusion

We present experimental results of the manipulation of inhomogeneous miscible fluids by controlling the topology and driving gain of the underlying acoustic vortices.

## References

- [1] Michael Baudoin, et al. *Sci. Adv.* **5**, eaav1967 (2019).
- [2] J.T. Karlsen and H. Bruus. *Phys. Rev. Appl.* **7**, 034017 (2017).
- [3] J.T. Karlsen, P. Augustsson and H. Bruus. *Phys. Rev. Lett.* **117**, 114504 (2016).



## Oscillatory force generation in non-equilibrium systems from peaked energy spectra

Anthony Bonfils<sup>1</sup>, Woosok Moon<sup>1</sup>, Dhrubaditya Mitra<sup>1</sup> and John S. Wettlaufer<sup>1,2,3</sup>

<sup>1</sup>Nordic Institute for Theoretical Physics, SE-10691 Stockholm, Sweden

<sup>2</sup>Yale University, New Haven, USA

<sup>3</sup>Mathematical Institute, Andrew Wiles Building, University of Oxford, Woodstock Road, Oxford OX2 6GG, UK

### Introduction

In 1948, Casimir predicted a net attractive force between two parallel conductive plates due to electromagnetic vacuum fluctuations. By analogy, the interaction of two boats on a wavy sea has been named Maritime Casimir effect. This is an example of force generation in non-equilibrium systems. According to Lee et al. [1], a key to force generation between two walls embedded in such systems is encoded in their energy fluctuation spectra. Furthermore, when the spectrum has a narrow peak, this force oscillates between repulsion and attraction as a function of wall separation. Although the ocean wave spectrum was measured in the sixties by Pierson and Moskowitz [2] for a fully developed sea, a theory explaining their observations - that is consistent with the argument of Lee et al. about the Maritime Casimir effect - has been lacking. The purpose of this ongoing work is to provide such a theory and apply it to systems displaying the same kind of fluctuations. In particular, the wave spectrum is believed to be the solution of a Fokker-Planck equation that should also be valid for active matter.

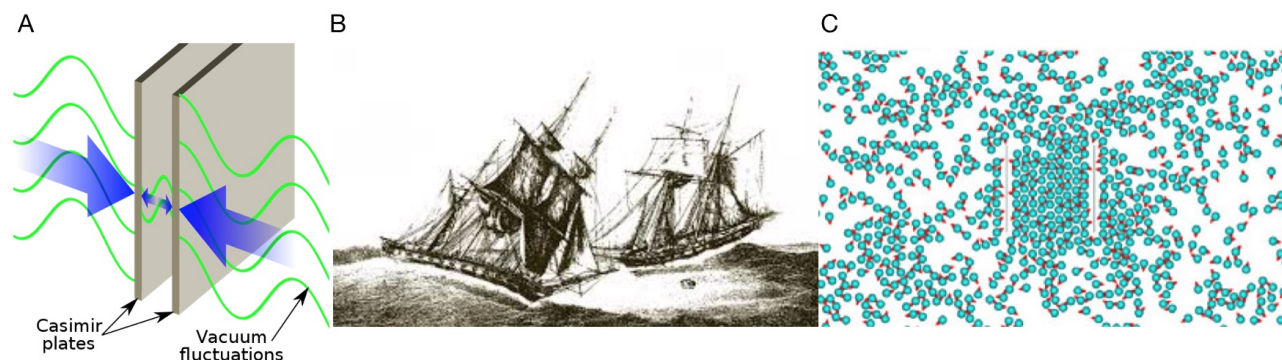


**Figure 1:** A) Original Casimir effect. B) Maritime Casimir effect. C) Force generation between plates in active matter.

### A hydrodynamic perspective

For centuries, scientists and sailors have been vexed by how the wind and the sea conspire to create the waves upon the oceans. Nonetheless, three main phenomena have been identified in the evolution of the wave spectrum: wave-wave interactions, direct energy input from the wind and dissipation by wave breaking (wave breaking involves processes beyond the scope of this work). On the one hand, wave-wave interactions are the framework of wave turbulence, which yields exact results for Hamiltonian systems. On the other hand, the direct growth of waves due to a turbulent wind is well described by the Phillips-Miles mechanism at short times. However, for a fully developed sea, there is a coupling between surface gravity waves and the turbulence of the wind that we believe plays an important role. The natural small parameter in this system is the air/water density ratio, which introduces a scale separation in wind-wave generation. Whereas the evolution of water waves occurs on a short (fast) time scale, the energy transfer from the wind occurs on a long (slow) time scale. The feedback of growing ocean waves on the wind profile occurs on an intermediate time scale and is described by a quasi-linear model proposed by Janssen [3], which is an assessment of the Miles theory for single mode growth. We show that Janssen's equations have similarity solutions and study them numerically. In particular, this involves the solution of the hydrodynamic Rayleigh equation at the critical level, which is the height at

which the phase speed of the wave is equal to the wind speed. We provide a general scheme to treat this sort of problem. In parallel, we explore the influence on the growth of waves of a viscous sublayer in the initial wind profile and discuss the agreement of Miles theory with Plant's experimental results [4].

### Application to active matter

Another example of force generation arises from micro-swimmers confined by a soft boundary, whose fluctuation spectrum is still the subject of study. However, Ni et al. [5] simulated self-propelled Brownian hard spheres confined between hard walls and found an oscillatory decay in the disjoining force, suggesting that the corresponding spectrum is unimodal. This prediction should be confirmed by analysis of Fokker-Planck equations of the same class as the one suggested for the ocean wave spectrum. Then, the duality between the Fokker-Planck and Langevin equations will yield a model for active matter elaborated so as to reproduce macroscopic properties.

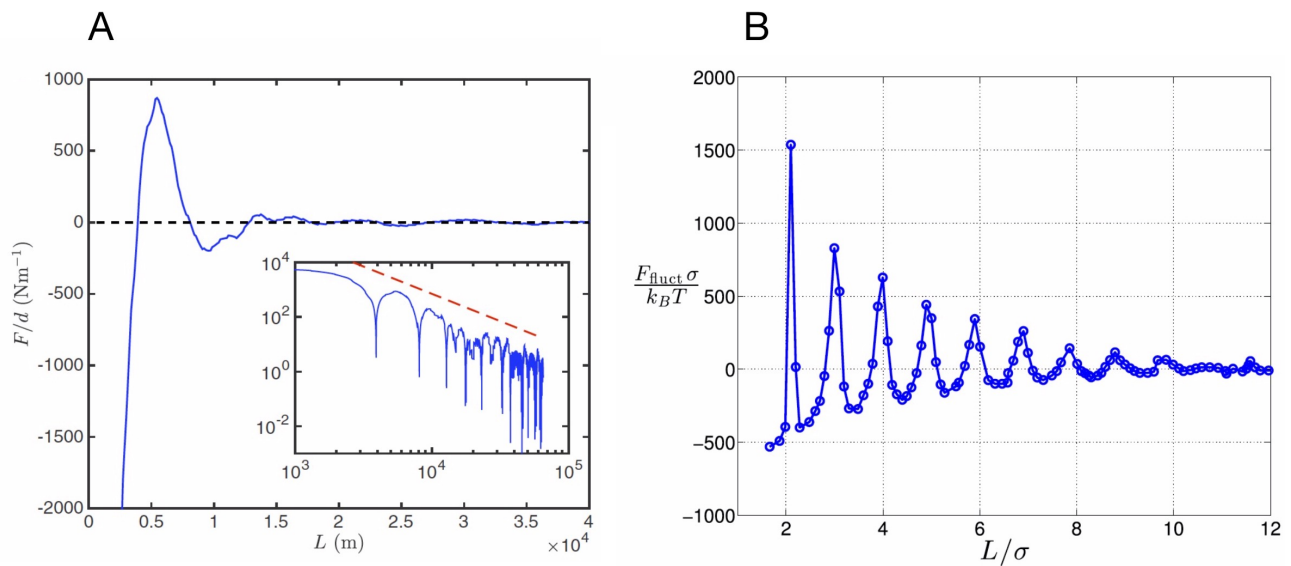


**Figure 2:** A) Force induced by the Pierson and Moskowitz spectrum as a function of the distance  $L$  between the ships [1]. B) Oscillatory force between hard walls in a suspension of self-propelled Brownian spheres of diameter  $\sigma$  [5].

### Conclusion

Inspired by the old riddle of the Maritime Casimir effect, we wish to connect bottom-up numerical and analytical approaches of the nonlinear non-local ocean waves problem back to a top-down statistical mechanical perspective, that might be useful for wave forecasting. This is based on a dual description of the spectrum of fluctuations that should be applicable to active matter as it seems to display fluctuations of the same kind, even though of completely different origin. The construction of a general theory for fluctuation spectra is a key focus both because of the ability to explain the origin of an oscillatory Casimir interaction and because of the top-down approach to treating the key processes of force generation in active matter, without appeal to a myriad of model specific details.

### References

- [1] A. Lee, D. Vella, and J. S. Wettlaufer. Fluctuation spectra and force generation in nonequilibrium systems. *PNAS; Proceedings of the National Academy of Sciences*, 114(35):9255–9260, 2017.
- [2] W.J. Pierson and L. Moskowitz. A proposed spectral form for fully developed wind seas based on the similarity theory of S.A. Kitaigorodskii. *J. Geophys. Res.*, 69:5181–5190, 1964.
- [3] Peter A. E. M. Janssen. Quasilinear approximation for the spectrum of wind-generated water waves. *Journal of Fluid Mechanics*, 117(-1):493, Apr 1982.
- [4] William J. Plant. A relationship between wind stress and wave slope. *J. Geophys. Res.*, 87(C3):1961–1967, March 1982.
- [5] R. Ni, MAC Stuart, and P.G. Bolhuis. Tunable long range forces mediated by selfpropelled colloidal hard spheres. *Phys Rev Lett*, 114:018302, 2015.



## Elastocapillary deformations of a superhydrophobic micropillar array

Diana Garcia-Gonzalez<sup>1,2</sup>, Jacco Snoeijer<sup>1</sup>, Michael Kapp<sup>1</sup> and Hans-Jürgen Butt<sup>2</sup>

<sup>1</sup>Physics of Fluids group, Max-Planck Center Twente for Complex Fluid Dynamics, Department of Science and Technology, University of Twente, Enschede, Netherlands.

<sup>2</sup>Max Planck Institute for Polymer Research, Mainz, Germany

E-mail: d.m.garciagonzalez@utwente.nl, garciagonzalez@mpip-mainz.mpg.de

### Introduction

Microstructured materials are interesting and common in science and industry because of their broad range in applications, yet their mechanical stability can be challenged in many ways. The possible applications are found in diverse industries such as anti-icing [1], fog harvesting [2], self-cleaning [3], and microelectromechanical systems (MEMS) [4]. These applications make use of periodical arrays of structures such that the total surface area of the material is maximized. In most cases involving photolithography, long thin elements are etched and then rinsed with different solvents in order to develop the final structures. During the rinsing process, many structures can deform and even break off from the substrate as a result from the coupling of capillary, elastic, and adhesive forces. This deformation of the structures can have different consequences, depending on its magnitude and the intended purpose of the structures. For example, the collapse of the structures can degrade the superhydrophobic properties of the material or, in the case of MEMS, it can completely impair its functionality.

As contact with a liquid—besides from mechanical stress—is one of the major causes for the material's structure break down, it is necessary to investigate further on the liquid-solid interplay of the microstructures. In this regard, important work has been done by Papadopoulos & Pinchasik [5] who investigated how adding flexibility to these microstructures impacts the advancing and receding contact angles of a glycerol-water droplet.

In this project, we aim to investigate the forces related to the collapsing microstructures and correlate the microscopic view with the shape of the liquid interface. We approach this question experimentally by creating soft polydimethylsiloxane (PDMS) micropillar arrays, and imaging their interaction with water using laser scanning confocal microscopy (LSCM).

As a first step towards understanding the collapse of the structures, we deposit a water droplet on top of the micropillar array. The evaporating droplet is then imaged under LSCM where vertical ( $xz$ ) and horizontal ( $xy$ ) cross-sections of the process are imaged.

In Figure 1(a) we show a sketch of the pillars when the droplet was just deposited on the surface. The pillars in contact with the contact line are initially undeformed by the fluid. When the drop evaporates, the liquid will pull on the pillars, leading to visible bending (Figure 1(b)).

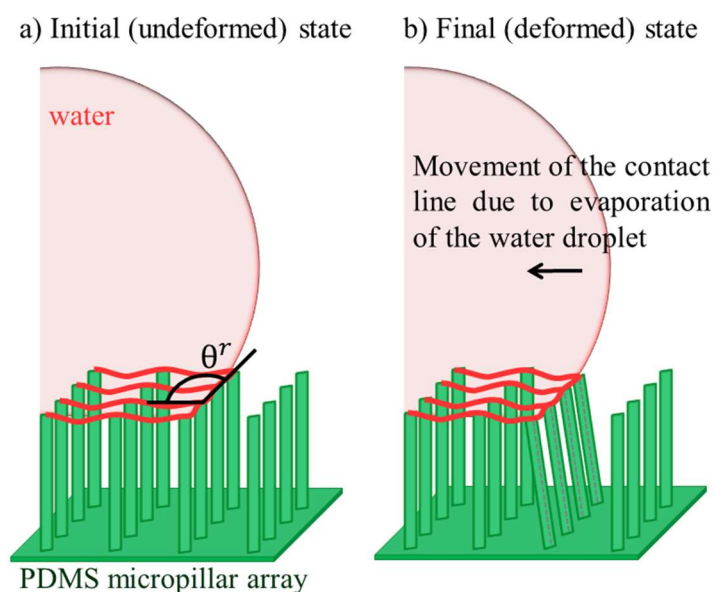


**Figure 1:** Sketch of a water droplet on top of the soft PDMS micropillar array. (a) The initial state after deposition, the pillars do not deform. (b) After some time, evaporation takes place and the contact line recedes. The pillars are deformed due to the elasto-capillary coupling between the droplet and the substrate.

### Experimental section

Polydimethylsiloxane (PDMS) cylindrical micropillar arrays are patterned onto a 170  $\mu\text{m}$  thick glass slide. The height,  $h$ , of the structures is 20  $\mu\text{m}$ , their diameter,  $d$ , is 20  $\mu\text{m}$ , and the center-to-center spacing

between structures is  $40\ \mu\text{m}$ . The structures are fabricated via a two-step soft-lithography process based on the protocol by Qin, Xia, & Whitesides (2010) [6].

The LSCM is an inverted microscope used to image the water drops on top of the micropillar array. For imaging, we used a  $20\times 0.75$  multi-immersion objective (water) and a combination of 458, 476 and 633 nm laser excitation lines. Four different photomultipliers are used to record reflection, two fluorescence signals and brightfield top-view images of the system (transmitted light).

### First results

The vertical cross-sections of the water droplet are processed such that the contour of the interface can be tracked in time. Afterwards, a second order polynomial is fitted to the curve such that measurements of the receding contact angle can be made.

Figure 2 shows the variation of the receding contact angle ( $\theta_r$ ) as a function of the horizontal displacement of the contact line ( $x$ ). Tracking of the water interface as it moves across the pillar tops is shown in the inset of the figure. The deformation of the pillars ( $\sim 5\ \mu\text{m}$ ) delays the depinning of the contact line from the pillar tops. However, when depinning occurs, the contact angle jumps to a higher value and continues to decrease monotonically until the next depinning event happens.

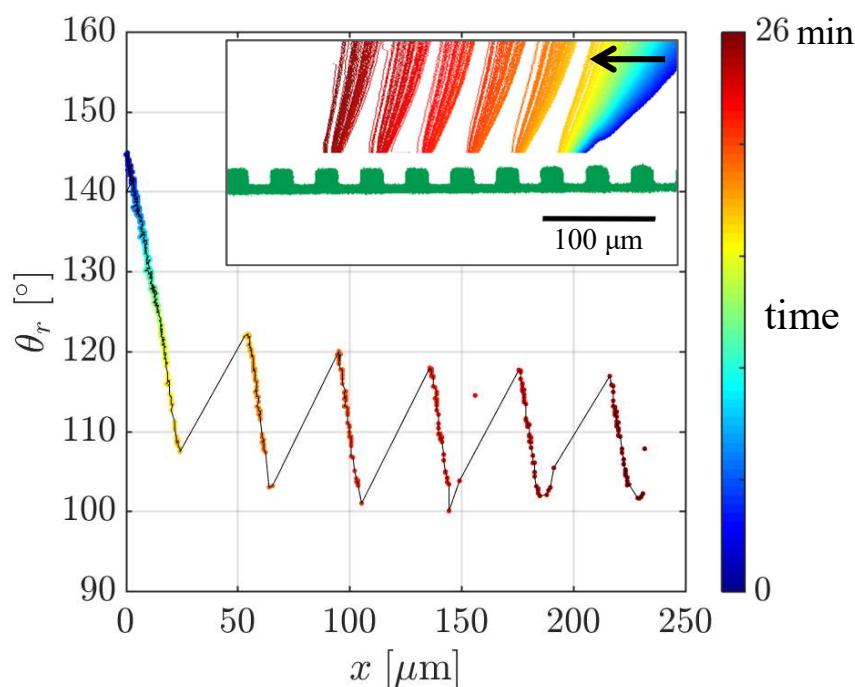


**Figure 2:** Variation of the receding contact angle of a water droplet evaporating on a PDMS micropillar array as a function of the horizontal displacement of the contact line. Measurements of the contact angle and contact line position are taken  $10\ \mu\text{m}$  above the pillar tops to avoid noise derived from the possible overlap of the fluorescence channels.

### Conclusion

Using confocal microscopy, we are able to characterize in high detail the movement of both the contact line, and the deformation of the soft micropillars. As the droplet evaporates, its radius decreases causing its contact line to contract and move over the surface. The coupling between the moving contact line and the pillars results in the bending of the micropillars as the contact line recedes.

Higher aspect ratio pillars should be probed as higher bending from the structures will influence the movement of the droplet's contact line.

### References

- [1] Kreder, M. J., Alvarenga, J., Kim, P., & Aizenberg, J. (2016). Design of anti-icing surfaces: smooth, textured or slippery?. *Nature Reviews Materials*, 1(1), 15003.
- [2] Zhang, L., Wu, J., Hedhili, M. N., Yang, X., & Wang, P. (2015). Inkjet printing for direct micropatterning of a superhydrophobic surface: toward biomimetic fog harvesting surfaces. *Journal of Materials Chemistry A*, 3(6), 2844-2852.
- [3] Blossey, R. (2003). Self-cleaning surfaces—virtual realities. *Nature materials*, 2(5), 301.
- [4] Tanaka, T., Morigami, M., & Atoda, N. (1993). Mechanism of resist pattern collapse during development process. *Japanese Journal of Applied Physics*, 32(12S), 6059.
- [5] Papadopoulos, P., Pinchasik, B. E., Tress, M., Vollmer, D., Kappl, M., & Butt, H. J. (2018). Wetting of soft superhydrophobic micropillar arrays. *Soft matter*, 14(36), 7429-7434.
- [6] Qin, D., Xia, Y., & Whitesides, G. M. (2010). Soft lithography for micro-and nanoscale patterning. *Nature protocols*, 5(3), 491.



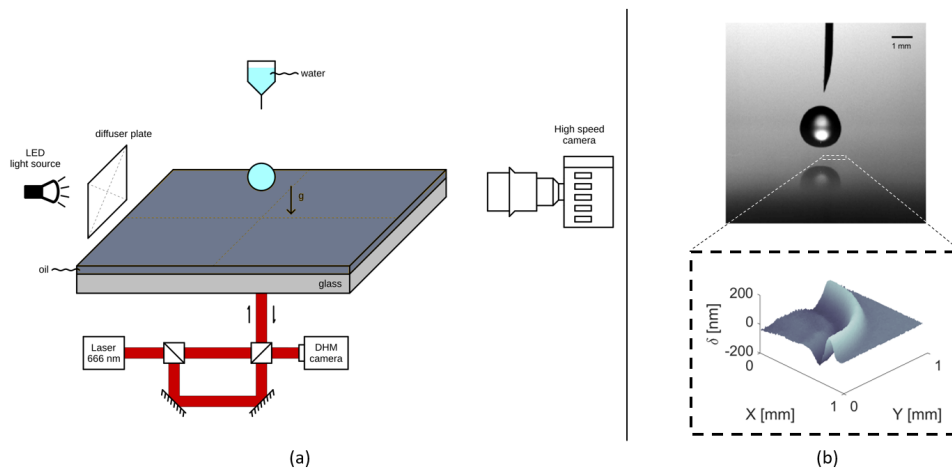
## Liquid free-surface deformations under bouncing drops

Srinath Lakshman<sup>1</sup>, Walter Tewes<sup>1</sup>, Kirsten Harth<sup>1</sup>, Jacco Snoeijer<sup>1</sup>, and Detlef Lohse<sup>1</sup>

<sup>1</sup>Faculty of Science and Technology, University of Twente, Enschede, The Netherlands  
E-mail: s.lakshman@utwente.nl

### Introduction

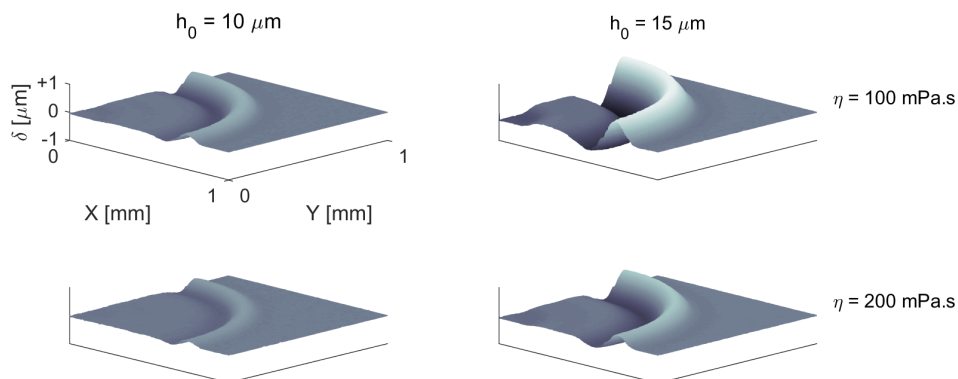
Surfaces coated with thin and viscous liquids can provide hydrodynamic lubrication much desired in many industrial applications. However, such liquid coatings can develop stability issues through the action of externally imposed pressures thereby losing their useful properties. In the present study, we investigate liquid free-surface deformations due to dynamic gas pressure buildup under bouncing drops,  $We \approx 1$ . Water drops of radius,  $R \approx 1 \text{ mm}$  and impact speed,  $v \approx 0.2 \text{ m/s}$  are made to bounce over thin and viscous silicone oil films of initial film height,  $h_0 \approx 5 - 15 \mu\text{m}$  and film viscosity,  $\eta \approx 50 - 350 \text{ mPa}\cdot\text{s}$ . Figure 1 show a schematic of the experimental setup and snapshot of a drop rebound experiment. Using Digital Holographic Microscopy technique, we measure 3D surface topography of the perturbed film immediately after drop rebound and its subsequent slow relaxation.



**Figure 1:** (a) Schematic diagram of the experimental setup (b) Side view and bottom view snapshots of a drop rebound experiment,  $h_0 = 10 \mu\text{m}$  and  $\eta = 350 \text{ mPa}\cdot\text{s}$

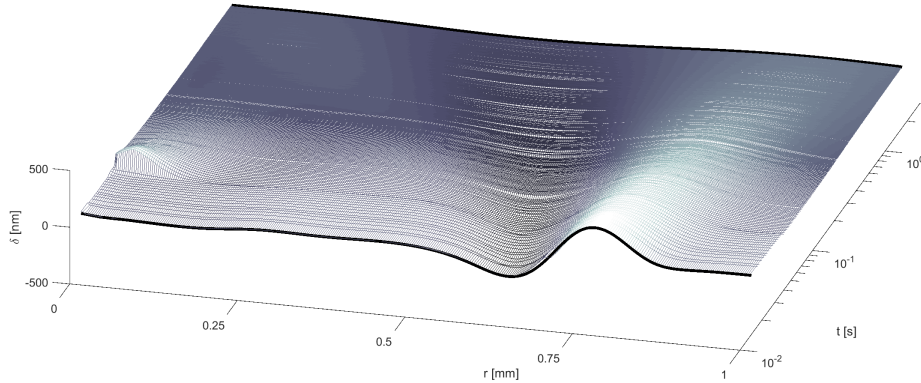
### Results

Figure 2 shows liquid free-surface deformations obtained immediately after drop rebound. The deformations increase with an increase in initial film height and decrease with an increase in film viscosity. The zero cross over point i.e., the radial location between the crest and the trough which reads  $\delta = 0$ , is around  $0.7 \text{ mm}$  in all the experiments hinting at bouncing dynamics unaffected by the underlying film properties[1].



**Figure 2:** Liquid free-surface deformations obtained immediately after drop rebound for varying film properties

Following this, the deformed surface heals itself when the droplet is sufficiently far away from the liquid film. Figure 3 shows a space-time plot of the slow healing dynamics. Using lubrication equation, we try and identify scaling laws for the visco-capillary wave spreading and its decay. The wave spreading shows a clear  $t^{1/4}$  scaling for two decades in time ( $\sim 0.01 - 1$  s). However, the wave decay does not show any clear scaling law because the late time asymptotic scaling requires larger decades in time which are not reached in the present experiments. Some previous publications also report similar trends in the wave spreading[2] and its decay[3].



**Figure 3:** Space-time diagram of the slow relaxation dynamics,  $h_0 = 10 \mu m$  and  $\eta = 100 mPa.s$

Numerical simulations are also performed to study the relaxation process, employing deformation profiles in Figure 2 as the initial condition. Figure 4 shows the amplitude decay comparison between experiment and numerics. The experimentally found relaxation dynamics is in good agreement with numerical simulations of the lubrication equation.

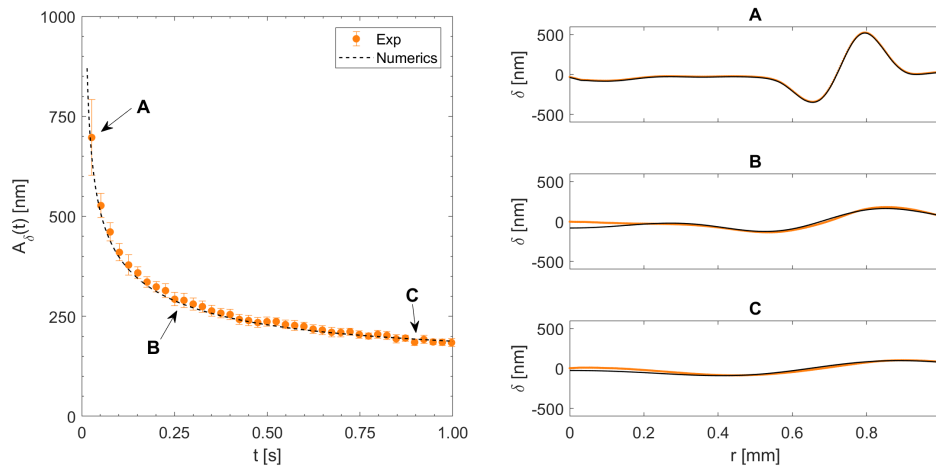


**Figure 4:** Amplitude decay comparison between experimental and numerical simulations,  $h_0 = 10 \mu m$  and  $\eta = 50 mPa.s$ . Direct comparison between experimental and numerical film profiles at 3 instances in time corresponding to **A** = 14 ms, **B** = 252 ms and **C** = 966 ms

## Conclusion

Liquid free-surface deformations under bouncing drops are studied. Thicker and low viscosity liquid films show larger surface deformations. The space-time plot of slow relaxation dynamics show clear visco-capillary wave spreading and its decay, obtained for two decades in time. The experimentally obtained relaxation dynamics show good agreement with the numerical simulations using lubrication equation.

## References

- [1] Hao, C., et al. *Nat. Commun.* **6**, 7986 (2015)
- [2] Hack, M. A., et al. *Appl. Phys. Lett.* **113**, 183701 (2018)
- [3] Benzaquen, M., et al. *Appl. Phys. Lett.* **107**, 053103 (2015)



## Self-similar coalescence of liquid lenses

Walter Tewes<sup>1</sup>, Michiel Hack<sup>1</sup>, Kirsten Harth<sup>1</sup> and Jacco Snoeijer<sup>1</sup>

<sup>1</sup>Physics of Fluids Group, University of Twente, 7500AE Enschede, The Netherlands  
E-mail: [w.b.h.tewes@utwente.nl](mailto:w.b.h.tewes@utwente.nl)

### Introduction

While the initial stage of surface tension-driven coalescence of sessile droplets on solid substrates is well understood [1], no such investigations have been previously reported on for the coalescence of viscous liquid lenses floating on a liquid bath (Fig. 1). Here, we study both experimentally and theoretically the time evolution of the liquid bridge connecting the two lenses. A self-similar evolution of the interface of the bridge is found and a theoretical description in terms of viscous sheet equations (cf. [2,3]) is proposed.

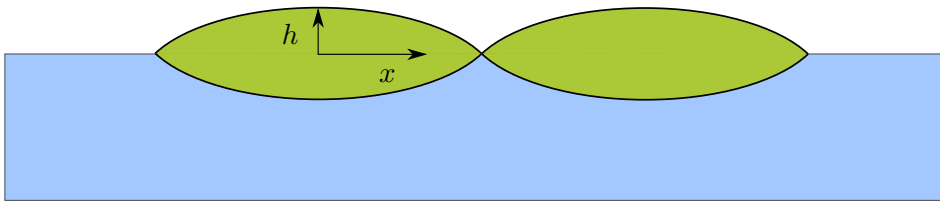


**Figure 1:** Sketch of the investigated system: Two viscous lenses of oil floating on a bath of water are brought into contact. The subsequent initial stage of the coalescence process is studied both experimentally and theoretically.

### Experimental results

We consider the coalescence of liquid lenses ( $\eta \sim 1.2$  Pa.s) of  $d \sim 8$ mm diameter and  $h_l \sim 0.8$ mm height floating on a bath of water. In order to address the small time-scales of the initial coalescence, the interfaces of liquid bridges are extracted from high-speed imaging of the plane perpendicular to the bath-air interface. Exemplary experimental results can be seen in Fig. 2 (left). The velocity at which the minimum  $h_0$  of the interface evolves is found to be in good approximation constant for the first  $\sim 0.1$ s of the process (Fig. 2 (right)). Furthermore, a good collapse of the measured interfaces at different instances in time is found (Fig. 2 (center)) when rescaling the height as  $H = h/h_0$  and the lateral spatial coordinate  $x$  as  $\xi = \theta x/h_0$ , where  $\theta$  denotes the equilibrium contact angle of the two floating lenses.

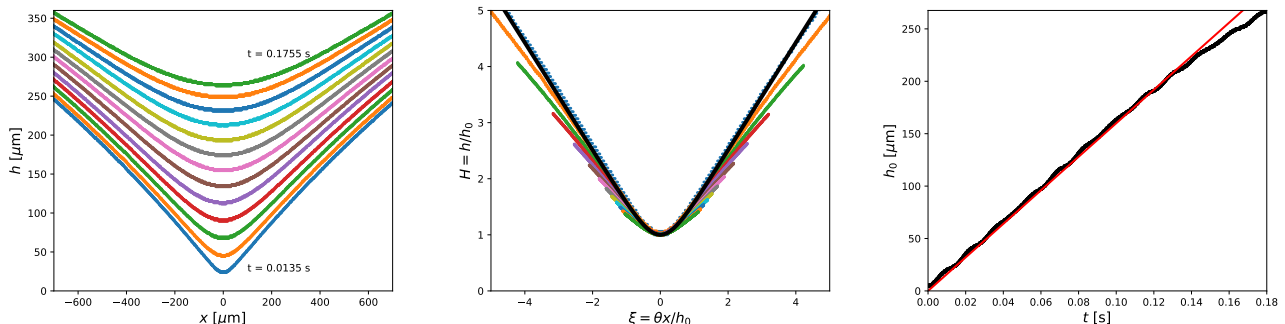


**Figure 2:** (left) Oil-water interface of the bridge between the liquid lenses at different instances in time. (center) Collapsed interfaces, by rescaling the lateral spatial coordinate and the height. The black line is the theoretical similarity solution. (right) The experimentally measured time evolution of the height minimum  $h_0$  is found to be initially linear.

### Theoretical and numerical results

In order to model the time evolution of the bridge during the initial coalescence, we propose to consider two-dimensional thin viscous sheet equations, which build on two important properties of the system: We make use of the *slender geometry* of the system, i.e., the separation of vertical and lateral length scales to reduce the governing hydrodynamic equations for the free surface flow. Furthermore, since the lenses consist of a liquid which is *significantly more viscous* than both air and water, the flow in the bridge region is assumed to be well described by *plug flow* (i.e. constant flow velocity in vertical direction). The resulting equations are coupled PDEs for the time evolution of the interface  $h(x, t)$  and the plug flow velocity  $u(x, t)$  (cf. [2,3]). In the overdamped (viscosity-dominated) limit, these equations allow for similarity solutions of the form

$$h(x, t) = v_0 t H(\xi), \quad u(x, t) = \frac{v_0}{\theta} U(\xi), \quad \xi = \frac{\theta x}{v_0 t} \quad (1)$$

in accordance with the scaling observed experimentally (Fig. 2).

We conduct numerical simulations of the thin viscous sheet equations in the overdamped limit starting from an initial condition close to the theoretical initial singularity. For sufficiently small times, we find a good match of the full numerical solutions and the similarity solutions obtained numerically from a system of ODEs which follow from the similarity ansatz (1) (Fig. 3 (center, right)). The slow departure from the similarity solution is studied and an approximately constant coalescence speed is obtained for several orders of magnitude in time (Fig. 3 (left)).

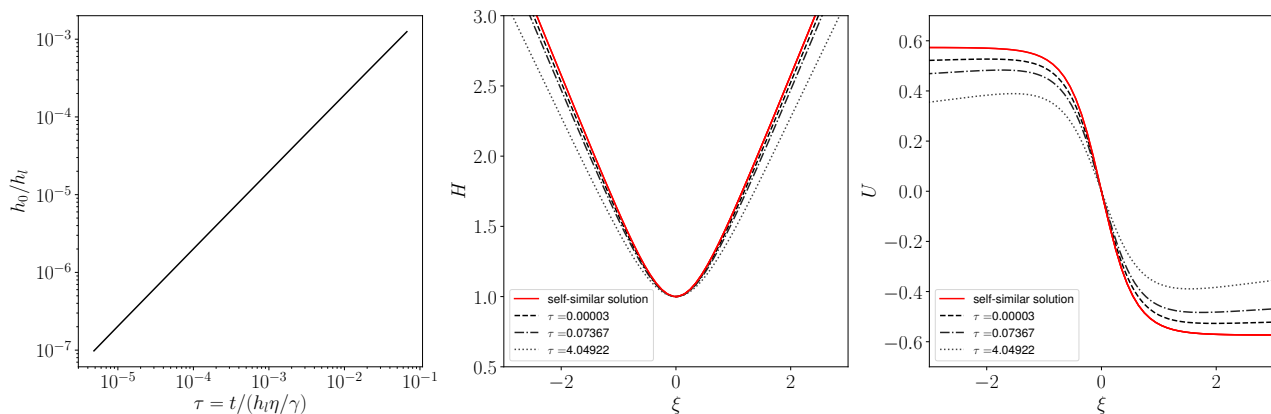


**Figure 3:** Results of numerical time simulations of the employed thin sheet model equations. (left) An approximately linear time evolution of  $h_0$  is found for several orders of magnitude in time. (center, right) Approach of the rescaled height and velocity profiles and the similarity solutions (red lines) for small times.

### Conclusion

The self-similar initial coalescence of viscous liquid lenses has been studied experimentally and in terms of simple thin viscous sheet equations. Experimentally, a good collapse of interface profiles at different instances in time has been found for the similarity scaling implied by the viscous sheet equations. The latter have been investigated in terms of full numerical time simulations, and a good match with similarity solutions obtained from ODEs has been found. In addition to these results, we will investigate the extension of symmetric viscous sheet equations to the asymmetric case of two interfaces of different surface tensions and the inertia-dominated regime.

### References

- [1] J. F. Hernández-Sánchez, L. A. Lubbers, A. Eddi, and J. H. Snoeijer, Physical Review Letters **109**, 184502 (2012).
- [2] N. Savva and J. W. M. Bush, Journal of Fluid Mechanics **626**, 211-240 (2009).
- [3] T. Erneux and S. H. Davis, Physics of Fluids A: Fluid Dynamics, **5(5)**, 1117-1122 (1993).



## Evolution of wetting ridge on liquid infused surfaces

Abhinav Naga, Anke Kaltbeitzel, William Wong, Lukas Hauer, Katharina Hegner, Maria D'Acunzi, Doris Vollmer

Max Planck Institute for Polymer Research, Mainz, Germany  
E-mail: nagaa@mpip-mainz.mpg.de

### Introduction

Liquid-infused surfaces form a class of functional materials that repel almost any type of solid or liquid. Inspired by the Nepenthes pitcher plant, these surfaces can be used in anti-icing, anti-biofouling, and to make easy-to-clean materials. Despite the already-existing technological applications in the medical, food and packaging industries, a fundamental understanding of how the lubricant reorganizes when drops are placed on liquid infused surfaces is still lacking. A simple way to produce a model liquid-infused surface is by impregnating a micropillar array with a wetting lubricant, typically an oil. A drop of an immiscible liquid placed on a such a surface gives rise to the formation of a wetting ridge and thus the creation of new interfaces. In this study, we use confocal microscopy to highlight the shape of the interfaces involved in the problem and to image the evolution of the wetting ridge when the level of impregnated lubricant is increased starting from an underfilled case.

### Preparation of liquid-infused surfaces

SU-8 micropillar arrays are produced on microscope coverslips by photolithography. Before impregnation, the substrates are coated with PDMS brushes to enhance the chemical compatibility with the 1000 mPa s silicone oil lubricant. The pillars used in the study have a cylindrical geometry with diameter  $30\ \mu\text{m}$ , height  $10\ \mu\text{m}$ , and pitch distance  $60\ \mu\text{m}$ .

### Imaging technique

The challenge with visualising drops on liquid-infused surfaces is that the drop and lubricant are indistinguishable when imaged using a regular optical camera, as showing in figure 1 (left). Using laser scanning confocal microscopy, we can image the wetting ridge and resolve the drop-lubricant interface (figure 1, right).

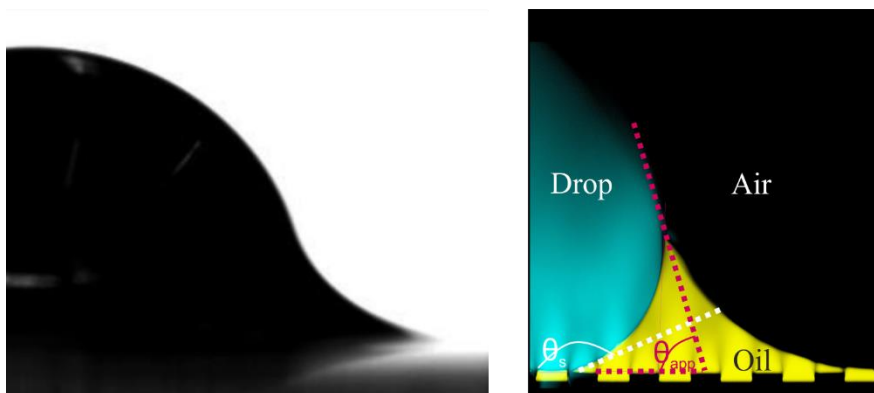


**Figure 1:** **Left:** Photo showing part of a drop on an oil-infused surface, taken with a standard goniometer camera. **Right:** Image of part of a drop (cyan) on an oil (yellow) infused surface constructed using a laser scanning confocal microscope. The oil and water phase can be distinguished by adding different fluorescent dyes in each phase. The red and white dashed lines illustrate two possible ways of defining a contact angle.

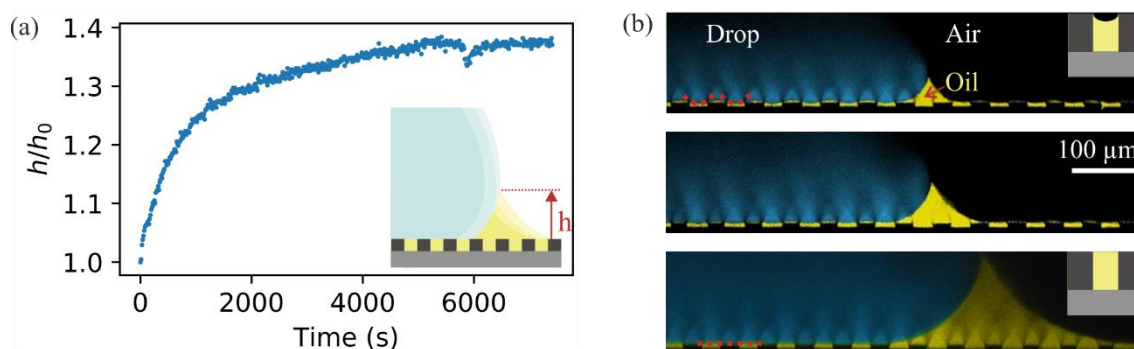


**Figure 2:** (a) Evolution of normalised height of the wetting ridge when oil is added to an initially underfilled liquid-infused surface. We define an oil-infused surface to be ‘underfilled’ if the oil-air interface is curved inwards as shown in the top figure of 2 (b).  $h_0$  is the height of the wetting ridge in the underfilled state before the addition of extra oil. (b) shows how the wetting ridge changes over time when the surface is filled with more oil. Notice the change in curvature of the drop-oil interface between the top and bottommost images which were taken around 2 hours apart.

### Shape of interfaces

The drop-vapour and drop-lubricant interfaces are described by circular arcs whose radii can be related by calculating the Laplace pressures at these interfaces.<sup>1</sup> The lubricant-vapour interface takes the shape of a catenoid. There are several possible ways of defining a contact angle and two of them are shown in Figure 1.  $\theta_{app}$  has the advantage that it can be extracted from an image taken by a standard camera whereas  $\theta_S$  requires an imaging technique capable of distinguishing the drop from the oil, such as a fluorescence microscope. However,  $\theta_{app}$  should be defined with care as it is a function of the height of the wetting ridge which can take several minutes to equilibrate after drop deposition.

### Evolution of the wetting ridge

The equilibrium size of the wetting ridge is a function of numerous parameters including the level of filling of the substrate. To investigate the influence of filling, we place a glycerol drop on an underfilled liquid-infused surface, wait for the system to equilibrate, and then add more lubricant to completely fill the micropillar array. The height of the wetting ridge is monitored as a function of time as shown in figure 2 (a). Note that the volume of oil available within the substrate is always much larger than the volume of oil in the wetting ridge.

### Conclusion

The wetting ridge surrounding a drop takes the shape of a circular arc at the drop-lubricant interface and a catenary curve at the lubricant-vapour interface. Drops on underfilled surfaces are surrounded by relatively smaller wetting ridges. We qualitatively show that the height of the wetting ridge increases at a decreasing rate when further lubricant is added to an initially underfilled state. The results highlight the sensitivity of the geometry of a wetting ridge on the level of lubricant contained in a liquid-infused surface.

### References

1. Sempredon, C., McHale, G. & Kusumaatmaja, H. Apparent contact angle and contact angle hysteresis on liquid infused surfaces. *Soft Matter* **13**, 101–110 (2016).
2. Schellenberger, F. *et al.* Direct observation of drops on slippery lubricant-infused surfaces. *Soft Matter* **11**, 7617–7626 (2015).



## Bubble spreading on liquid-infused surfaces

Alexandros T. Oratis<sup>1</sup>, Mark Menesses<sup>1</sup> and James C. Bird<sup>1</sup>

<sup>1</sup>Department of Mechanical Engineering, Boston University, Boston, United States  
E-mail: aoratis@bu.edu, URL: <http://www.bu.edu/fluidlab>

### Introduction

Understanding the spreading dynamics of drops and bubbles on solid surfaces is important for a variety of applications, ranging from ink-jet printing to biofouling. When an air bubble comes slowly into contact with a submerged solid surface, it will initiate the drainage of the intermediate thin liquid film. At some critical thickness, the film will rupture and as a result the bubble will spread on the surface. For a partially wetting surface the bubble will spread within tens of milliseconds (Fig. 1a). In contrast, if the surface is superhydrophobic, the bubble comes into contact with the air film trapped within the texture of the surface and spreads much faster (Fig. 1b). The dynamics are very similar to the coalescence of bubbles, which depend on the competition between capillarity and inertia [1]. This balance can be extended to the spreading of a bubble on a surface, where the resulting spreading radius will depend on the equilibrium contact angle  $\theta_{eq}$  [2]. While the existing models can accurately describe the spreading behavior of a bubble on a superhydrophobic surface, they fail when it comes to partially wetting surfaces (Fig. 1c). This lack of agreement can be attributed to the heterogeneous surface chemistry and texture, which leads to contact line pinning. Therefore, it becomes evident that the contact line dynamics affect the behavior of bubbles spreading on a solid surface. Here, we propose to bridge the mechanisms of bubble contact to an air layer and a solid surface by experimentally studying the spreading dynamics of bubbles on liquid-infused surfaces. Indeed, liquid-infused surfaces are compelling to use due their ability to suppress contact line pinning [3].

### Experiments

Liquid-infused surfaces consist of a microtexture through which a lubricant, typically a silicone oil, can be infused and remain stable due to the capillary interaction with the solid defects. We carry out experiments by first developing superhydrophobic surfaces using the commercially available coating Ultra-Ever Dry (UltraTech International Inc.) The surface is then lubricated with silicone oil of density  $\rho$  and viscosity  $\mu$  through spontaneous imbibition. The lubricated surface is then placed in a bath of water, in which an air bubble is slowly brought into to contact with the surface. We vary the silicone oil's viscosity in the range  $10 \text{ mPa} \cdot \text{s} \leq \mu \leq 10^6 \text{ mPa} \cdot \text{s}$ . As the bubble begins to spread, the motion is recorded with a high speed camera, with frame rates ranging between 5,000-25,000 frames per second depending on the film's viscosity.

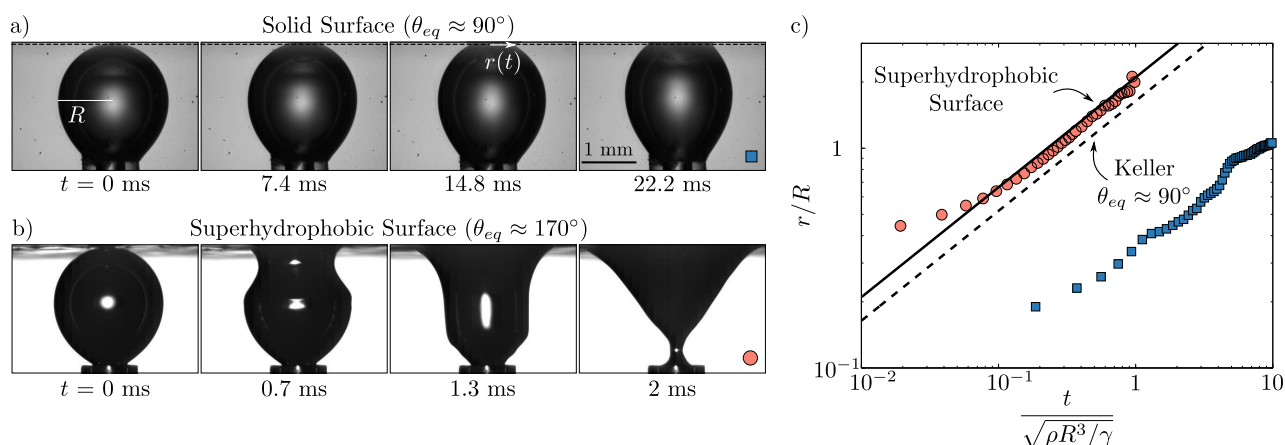


**Figure 1:** Bubble spreading on a solid and superhydrophobic surfaces. a) For a partially-wetting surface with equilibrium contact angle  $\theta_{eq} \approx 90^\circ$ , a bubble with initial radius  $R = 1 \text{ mm}$  will spread within tens of milliseconds. b) For a superhydrophobic surface, a bubble with the same radius will spread much faster. c) Current models for the evolution of the spreading radius  $r$  agree well for the spreading behavior on the superhydrophobic surface but not for the partially-wetting surface.

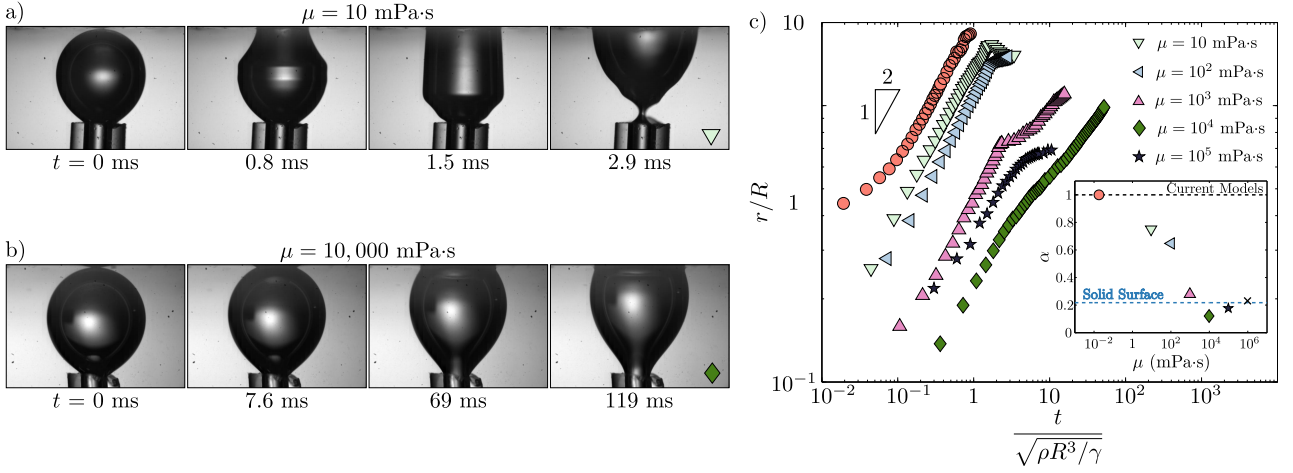


**Figure 2:** Bubble spreading on liquid-infused surfaces. a) A bubble spreading on a liquid-infused surface with a lubricant viscosity of  $\mu = 10$  mPa-s, spreads relatively fast within a couple of milliseconds. b) If the lubricant viscosity is increased to  $\mu = 10^4$  mPa-s, the bubble spreads much slower. c) The spreading radius  $r$  follows a power-law that scales as  $t^{1/2}$  at early stages, regardless of the lubricant viscosity. Inset: The dimensionless prefactor  $\alpha$  of the power law follows a non-monotonic relationship with respect to the lubricant's viscosity.

## Results

A bubble coming into contact with a lubricated surface with relatively small viscosity of  $\mu = 10$  mPa-s manifests fast spreading rates, only slightly slower than the superhydrophobic surface (Fig. 2a). In contrast, when the lubricant's viscosity is increased to  $\mu = 10^4$  mPa-s, the bubble will spread a hundred times slower (Fig. 2b). When the spreading radii against time are plotted on logarithmic scales, we observe that they initially follow a power law with the same exponent of  $1/2$ , which is independent of the lubricant viscosity (Fig. 2c). Yet, the radii do not collapse using an inertial time scale of  $\sqrt{\rho R^3/\gamma}$ , where  $\gamma$  is water-air surface tension, nor when a viscous time scale is used. The lack of a collapse using either time scale, indicates the combined effects of the liquid's inertia and the lubricant's viscosity. It is therefore more constructive to consider a dimensionless prefactor for the power law to investigate the effects of the surface's viscosity. As the viscosity increases the prefactor decreases and the bubble spreads progressively slower. However, as the viscosity of the lubricant exceeds a critical value, the prefactor reverses and starts increasing again. These results can be quantified using Keller's inertial model of a bubble spreading on a solid surface:

$$\frac{r}{R} = \left[ \frac{32}{3} (1 - \cos \theta_{eq}) \right]^{1/4} \left( \frac{t}{\sqrt{\rho_w R^3/\gamma}} \right)^{1/2}, \quad (1)$$

Because the equilibrium contact angle does not vary with viscosity, Eq. 1 predicts that the prefactor for each lubricated surface should remain constant. Yet, our experimental results suggest otherwise, and could potentially be resolved by replacing the equilibrium contact angle with a dynamic contact angle. Indeed, a dynamic contact angle is known to depend on the viscosity near the contact line and affect the dynamics of drops and bubbles on a liquid-infused surfaces.

## Conclusion

Bubbles coming into with liquid-infused surfaces, spread with a power law reminiscent of bubble-coalescence. While the dynamics of during bubble coalescence can be described using a combination of inertial and viscous time scales [4], this does not describe the spreading dynamics on liquid-infused surfaces. A better understanding of the nature of the viscous dissipation near the contact line can provide better insight on the effect of the surface's viscosity on the spreading dynamics, and potentially be extended to understand the spreading behavior on solid surfaces.

## References

- [1] H. de Maleprade, C. Clanet, and D. Quere. Physical Review Letters **117**, 094501 (2016).
- [2] J.B. Keller. The Physics of Fluids **26**, 3451-3453 (1983).
- [2] A. Lafuma and, D Quere Europhysics Letters **96**, 56001 (2011).
- [4] J.D. Paulsen, R. Carmigniani, A. Kannan, and J.C. Burton, and S.R. Nagel. Nature Communications **5**, 3182 (2014).



# Differential impedance spectra analysis reveals optimal actuation frequency in bulk mode acoustophoresis

Valentina Vitali, Giulia Core, Fabio Garofalo, Thomas Laurell, Andreas Lenshof

Department of Biomedical Engineering, Lund University, Lund, Sweden  
 Email: valentina.vitali@bme.lth.se

## Introduction

Acoustophoretic devices are designed to operate at a specific frequency. However, there are always slight deviations in operating frequency due to details in the manufacturing and assembly processes that are difficult to precisely control. The channel resonance frequency is thus commonly found by visual inspection of particle band formation while scanning the frequency. This method is operator dependent and can be time consuming. It would be advantageous to assess the acoustophoretic component automatically by measuring the electrical impedance. Dual et al. [1] suggested measuring the electrical impedance to characterize ultrasonic systems and to select optimal operation frequency based on the difference between an air filled and fluid filled component. Hammarström et al. [2] managed to track the resonance frequency, given a pre-annotated impedance minimum, when actuating a simple glass capillary in an acoustic trapping system [2]. Garofalo et al. [3] proposed a set of empirical criterions to predict the resonance frequencies in the microchannel of a silicon-glass acoustophoretic device based on theoretical electromechanical simulations. Neither of these approaches have, however, proven successful in tuning the operating frequency in an arbitrary acoustophoretic setup. We present a new method to select the optimal actuation frequency in bulk acoustophoretic devices, by means of differential impedance spectra analysis measured via the actuating piezoelectric transducer (piezo).

## Results and discussion

Four devices of different designs and materials were tested. Water and a 20 % cesium chloride (CsCl, a buffer density modifier) solution were sequentially infused into the microchannel designed for  $\approx 2$  MHz resonance in width, and impedance spectra were collected in the range approx. 1.5 - 2.8 MHz (Fig. 1b). The two fluids induced measurable differences in the impedance spectra associated with the horizontal channel resonance mode. The differences are presented as the absolute value of the complex-valued impedance difference, normalized to the absolute value of the water filled channel impedance spectrum (Normalized Differential Spectrum, NDS), Fig. 1d. As a comparison, an air and water filled channel was also measured, Fig. 1c.

The optimal actuation frequency is achieved when the microchannel becomes a resonator that drives the suspended particles to the pressure nodal plane (particle focusing). The resonance modes that provided good acoustic focusing of 5  $\mu\text{m}$  polystyrene microbeads were identified using an in-house developed automatic setup, FocuScan. This setup permitted the identification of the best working frequency by an automatic actuation of the device, image acquisition and post processing (Figure 2). More specifically, the FocuScan software was used to perform a frequency sweep from 1.5 MHz to 2.8 MHz with a frequency step of 5 kHz and a delay time between sweeps of 4s. This process was repeated for different peak-to-peak voltages (2, 4, 6 and 8 Vpp). Additionally, the FocuScan software was used to control the camera data acquisition. A total of ten images were acquired at each frequency step. The images acquired at the same frequency were subsequently averaged and the full width at half maximum of the focused particle band was computed and normalized over the width of the microchannel (Normalized Particle Bandwidth, NPB). In order to identify the best working frequency, the NPB vs actuation frequency was plotted. The minima of the NPB indicate the best working frequency.

Figures 1d and 3a-c show the comparison between the NDS (black solid line) and the results of the FocuScan experiments (colored bands). The different colors are used to indicate the different actuation voltages (2, 4, 6 and 8 Vpp), while the intensity of the color indicates the grade of focusing. Light colored bars indicate modest acoustic particle focusing ( $0.4 < \text{NPB} < 0.2$ ). Dark colored bars indicate regions of efficient acoustic particle focusing ( $\text{NPB} < 0.2$ ). It can be noticed that at the lowest actuation voltage, 2 Vpp, particle focusing (dark red colored bands) is found in close proximity to the NDS peak. As expected by increasing the applied voltage, the frequency region of good particle focusing widens around the NDS peak.

In contrast to earlier reports [1], we find that the differential impedance spectra for an air vs fluid filled channel is non-conclusive, whereas the region of good particle focusing agrees very well with the differential impedance peaks for water vs. CsCl filled channels (Fig 1c, 3a-c).

## Conclusion

The developed method enables a rapid, reproducible and precise determination of the optimal working frequency of bulk acoustophoretic devices.

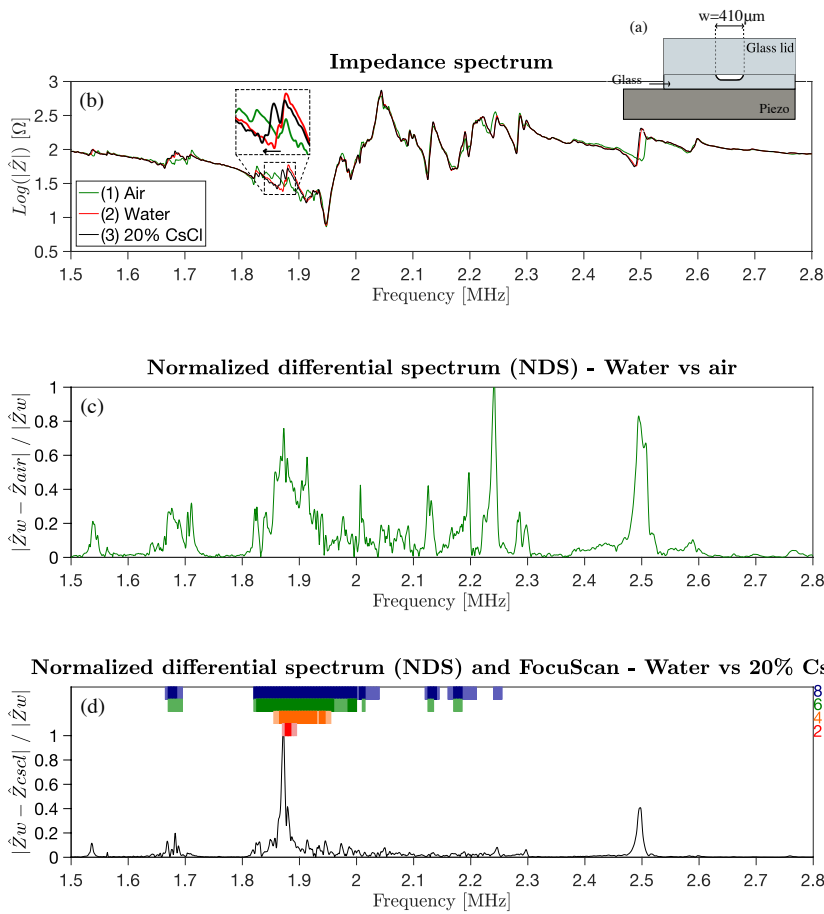


**Figure 1.** (a) Sketch of the cross-section of a glass-glass device. The device has a straight channel design with one inlet and one outlet. (b) Impedance magnitude spectrum of the (1) air filled, (2) water filled and (3) 20% CsCl filled device. (c) Normalized Differential Spectrum (NDS) water vs air. (d) NDS water vs 20% CsCl. It can be seen that the NDS water vs 20% CsCl presents one main peak that agrees with the best focusing region. Instead, the noisier diagram for NDS water vs air does not give any clear indication of a channel resonance.

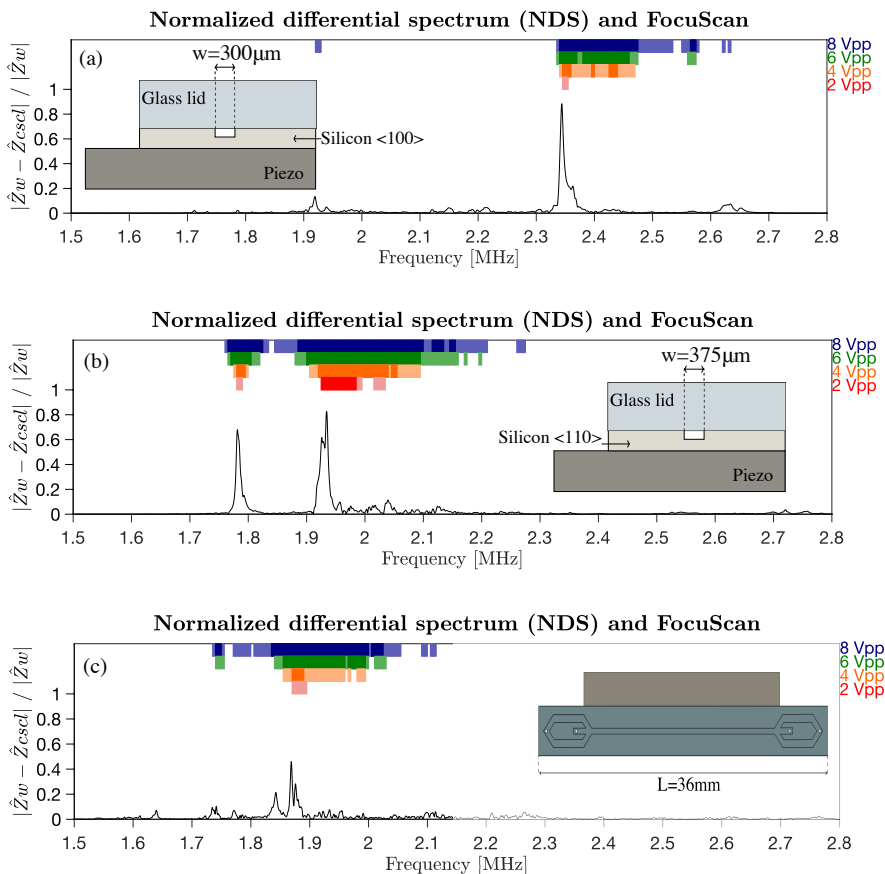


**Figure 3.** Normalized Differential Spectrum, NDS, (black solid line) water vs 20% CsCl and FocuScan results (colored bars) for three different devices (a-c). Light color bars indicate modest acoustic particle focusing. Dark colored bars indicate regions of efficient acoustic particle focusing at actuation voltages from 2-8 Vpp. The differential impedance peak agrees with the best focusing region. Devices a and b have a straight channel design. Device c has the same cross-section as device b.

## References

- [1] J. Dual et al., Lab on a Chip, 12(5):852–862, 2012.
- [2] B. Hammarström et al., Lab on a Chip, 14(5):1005–1013, 2014.
- [3] F. Garofalo et al., Physical Review Applied, 7(5):054026, 2017.

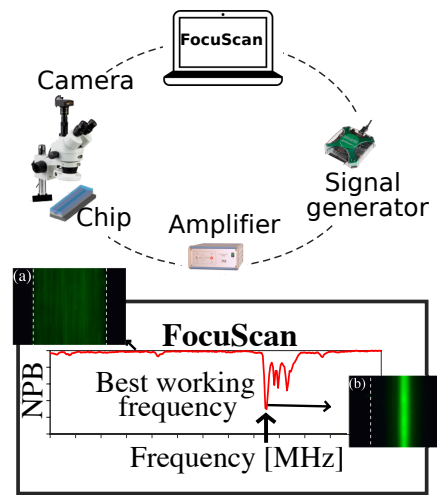


**Figure 2.** Sketch of the FocuScan setup. The FocuScan software was used (1) to operate the device through a signal generator and an in-house designed amplifier and (2) to control the camera data acquisition. A frequency sweep was performed, and images were acquired at each frequency step. For each actuation frequency, the Normalized Particle Bandwidth (NPB) was computed. The NPB is close to 1 when particles occupy the full width of the microchannel (a). When particles are acoustically focused, the NPB gets smaller (b). In order to identify the best working frequency, the NPB vs actuation frequency was plotted. The minimum of the NPB indicates the best working frequency. White dashed lines indicate the channel boundary.



# Bulk-driven acoustic streaming induced by weak symmetry breaking of the geometry or by a rotating actuation

Jacob S. Bach and Henrik Bruus

Department of Physics, Technical University of Denmark, Kongens Lyngby, Denmark  
E-mail: [jasoba@fysik.dtu.dk](mailto:jasoba@fysik.dtu.dk), URL: [www.fysik.dtu.dk/microfluidics](http://www.fysik.dtu.dk/microfluidics)

## Introduction

Bulk-driven (Eckart) acoustic streaming is a phenomenon which is driven by dissipation in the bulk of a fluid. It is often neglected relative to the boundary-driven (Rayleigh) streaming in micro-acoustofluidic devices of length scales comparable with the acoustic wave length. However, bulk-driven streaming was observed by Antfolk *et al.* [1] as a single vortex in a nearly-square capillary, and from a direct simulation they showed that this phenomenon could be explained if two perpendicular single modes oscillates with a quarter-period phase difference. We study theoretically bulk-driven acoustic streaming at resonance in a box with viscous boundary layers. We find that this phenomenon occurs, if the acoustic resonance is rotating, *i.e.* carries a non-zero angular momentum density  $\mathcal{L}_{ac}$ . We determine the conditions on the actuation and geometry, where the bulk-driven acoustic streaming is largest. We also investigate when the acoustic streaming is bulk- and when it is boundary-driven.

## Rotating double-mode resonances including viscous boundary layers

For a hard-walled box-shaped cavity with sidelengths  $L_x$ ,  $L_y$ , and  $L_z$ , and viscous boundary layers, we have derived analytical expressions for the single-mode resonances  $p_1^{lmn}$  with integer numbers  $l$ ,  $m$ , and  $n$  of half waves in the  $x$ ,  $y$  and  $z$ -direction, respectively [2]. The phase  $\phi^{lmn}$  and amplitude  $|p_1^{lmn}|$  of these modes are determined by the actuation at the boundaries and by an internal frequency dependency. The latter is responsible for a phase shift from  $-\pi$  to 0, as the actuation frequency  $f$  is swept past a resonance frequency  $f_{res}^{lmn}$ . In certain geometries, two modes may have similar resonance frequencies and may therefore be excited at the same frequency, forming a so-called double-mode resonance  $p_{l'mn}^{lmn}$  [2]. In contrast to a single mode, a double mode may lead to a non-zero acoustic angular momentum density  $\mathcal{L}_{ac}$ , and a corresponding body force  $\mathbf{f}_{ac}$  that drives the bulk-driven streaming  $\mathbf{v}_2^{blk}$ . In Fig. 1 we study this phenomena by exciting the double mode  $p_{020}^{200}$  in a nearly-square cavity of aspect ratio  $A = \frac{L_x}{L_y} \approx 1$ . We use both (a1) a non-rotating and (a2) a rotating actuation. Remarkably, the non-rotating actuation leads to a rotating resonance when the aspect ratio  $A$  deviates by 0.2% from unity, see Fig. 1(b1) and (d1). At this particular aspect ratio, the resonance frequencies  $f_{res}^{200}$

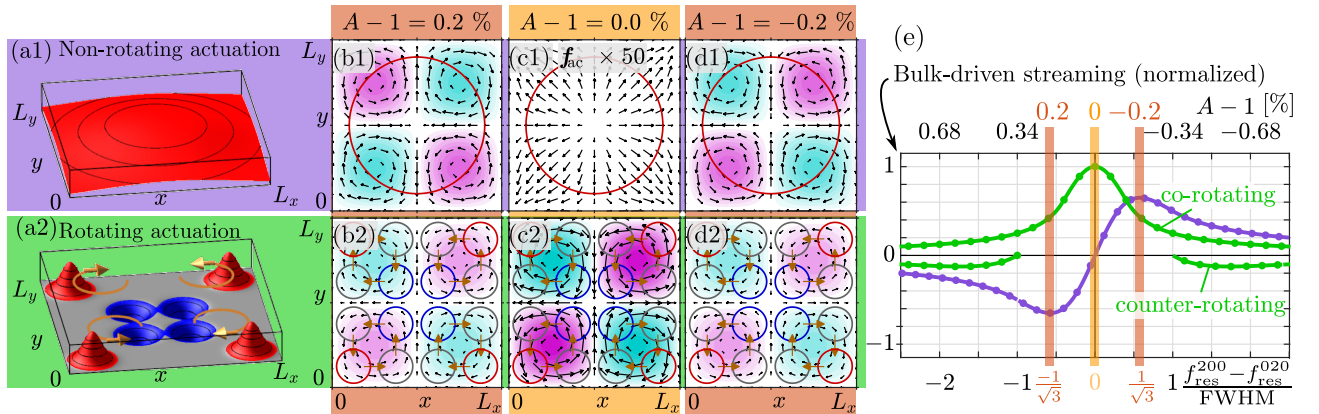


**Figure 1:** Study of the acoustic rotation in a shallow nearly-square cavity excited by a non-rotating (purple), or a rotating actuation (green), at the bottom surface. (a) The two actuation displacement profiles. (b)-(d) The body force  $\mathbf{f}_{ac}$  (arrows) and the acoustic angular momentum density  $\mathcal{L}_{ac}$  (cyan is negative and magenta is positive) for three different aspect ratios  $A = \frac{L_x}{L_y}$ . The red and blue circles correspond to the surface displacement up and down, respectively, as shown in (a). (e) Normalized bulk-driven streaming velocity as a function of the mode separation  $\frac{f_{res}^{200} - f_{res}^{020}}{FWHM}$  (lower axis), or equivalently, the aspect ratio  $A$  (upper axis) for the non-rotating (purple) and rotating actuation (green). Solid curves are numerical and dots are analytical results. The red and golden vertical slaps correspond to the aspect ratios shown in (b)-(d) of same color.

and  $f_{\text{res}}^{020}$  are separated optimally, such that they oscillate out of phase while maintaining a significant mode overlap. The rotating actuation shown in Fig. 1(a2)-(d2) gives maximized rotation in the perfect square as expected. In Fig. 1(e) we plot the signed magnitude of the acoustic rotation ( $\mathcal{L}_{\text{ac}}$ ,  $\mathbf{f}_{\text{ac}}$ , or  $\mathbf{v}_2^{\text{blk}}$ ) versus the aspect ratio  $A$  (upper axes) and mode separation  $f_{\text{res}}^{200} - f_{\text{res}}^{020}$  (lower axis). For the non-rotating actuation (purple) we localize an optimal mode separation of  $\frac{1}{\sqrt{3}}$  of the full width at half maximum (FWHM). For the rotating actuation (green) we find both co-rotating and, surprisingly, counter-rotating double modes, relative to the actuation rotation.

### Bulk-driven versus boundary-driven acoustic streaming

The acoustic rotation of double-mode resonances is directly related to the body force  $\mathbf{f}_{\text{ac}}$ , which is the source of the bulk-driven streaming  $\mathbf{v}_2^{\text{blk}}$ . In Fig. 2, we show simulation results of the acoustic streaming  $\mathbf{v}_2$  induced by the rotating double modes  $p_{0l0}^{l00}$  with  $l = 2, 4$ , and  $6$ , and thus increasing frequency. Similar to the experiment by Hagsäter *et al.* [3], the cavity has dimension  $L_x \approx L_y \approx 2000 \mu\text{m}$  and  $L_z = 200 \mu\text{m}$ , and we have optimized the aspect ratio  $A = \frac{L_x}{L_y}$  to maximize the acoustic rotation for the non-rotating actuation shown in Fig. 1(a1). We find that the bulk-driven streaming  $\mathbf{v}_2^{\text{blk}}$  in Fig. 2(a)-(c) increases with frequency, whereas the boundary-driven streaming  $\mathbf{v}_2^{\text{bdr}}$  in Fig. 2(d)-(f) is almost frequency-independent. Consequently, the total streaming  $\mathbf{v}_2$  for  $l = 2$  in Fig. 2(g) is boundary-driven whereas the total streaming  $\mathbf{v}_2$  for  $l = 6$  in Fig. 2(i) is bulk-driven.

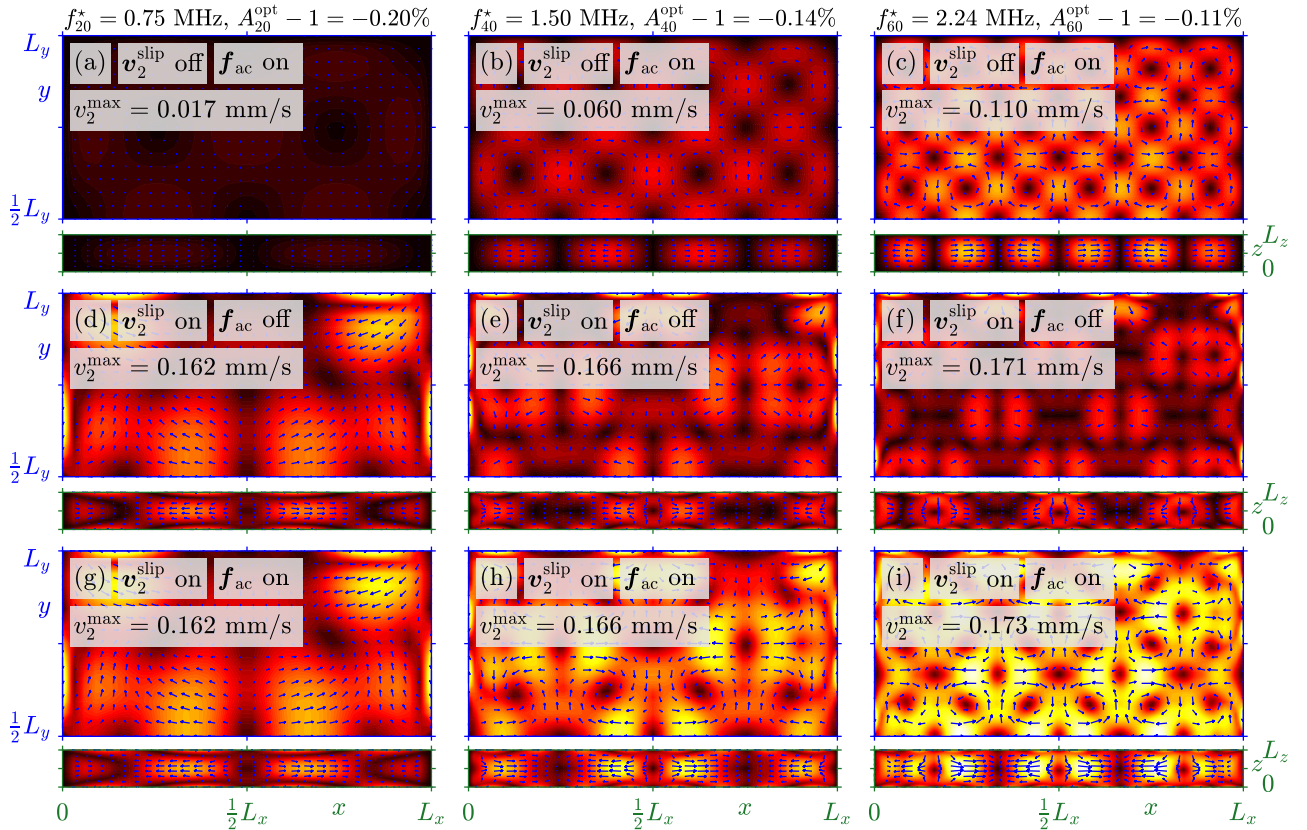


**Figure 2:** Simulation of the acoustic streaming  $\mathbf{v}_2$  in water from 0 (black) to 0.17 mm/s (white) in the horizontal ( $x$ - $y$ ) center plane at  $z = \frac{1}{2}L_z$  and the vertical ( $x$ - $z$ ) center plane at  $y = \frac{1}{2}L_y$ , where we have used the non-rotating actuation shown in Fig. 1(a1) at the bottom surface. In each column, the double mode  $l00 + 0l0$  is excited for  $l = 2, 4$ , and  $6$ , respectively. The first row (a)-(c) shows the bulk-driven streaming  $\mathbf{v}_2^{\text{blk}}$ , the second row (d)-(f) shows the boundary-driven streaming  $\mathbf{v}_2^{\text{bdr}}$ , and the third row (g)-(i) shows the total streaming  $\mathbf{v}_2$ .

### Conclusion

We have studied bulk-driven acoustic streaming induced by rotating double-mode resonances in a closed microcavity, and have shown that it may dominate over boundary-driven streaming. Our analysis shows that the rotation can be induced either by the actuation or by the geometry, and the bulk-driven streaming increases with actuation frequency, bulk viscosity, and cavity volume [2].

### References

- [1] M. Antfolk, P. B. Muller, P. Augustsson, H. Bruus, and T. Laurell, *Lab Chip* **14**, 2791 (2014).
- [2] J. S. Bach and H. Bruus, *Phys Rev E*, submitted (2019), arXiv preprint [arxiv.org/abs/1905.09132](https://arxiv.org/abs/1905.09132).
- [3] S. M. Hagsäter, T. G. Jensen, H. Bruus, and J. P. Kutter, *Lab Chip* **10**, 1336–1344 (2007).



## Characterization of Surface Acoustic Waves Diffraction Driven Mechanisms in Microfluidic Systems

Armaghan Fakhfouri<sup>1,2</sup>, Citsabehsan Devendran<sup>2</sup>, David J. Collins<sup>3</sup>, Andreas Winkler<sup>1</sup>, Hagen Schmidt<sup>1</sup>, Julio Soria<sup>4</sup> and Adrian Neild<sup>2</sup>

<sup>1</sup>Leibniz IFW Dresden, SAWLab Saxony, 01069 Dresden, Germany

E-mail: [a.fakhfouri@ifw-dresden.de](mailto:a.fakhfouri@ifw-dresden.de)

<sup>2</sup>Department of Mechanical and Aerospace Engineering, Monash University, Clayton 3800, Victoria, Australia

<sup>3</sup>Department of Biomedical Engineering, University of Melbourne, Parkville 3052, Victoria, Australia

<sup>4</sup>Laboratory for Turbulence Research in Aerospace and Combustion (LTRAC), Department of Mechanical and Aerospace Engineering, Monash University, Clayton, Victoria 3800, Australia

### Introduction

Acoustic forces arising from high-frequency surface acoustic waves (SAWs) underpin a broad range of promising techniques for a versatile, yet contactless manipulation of particles and cells in microfluidic systems. The acoustic effects exploited for manipulation, typically include acoustic radiation and acoustic streaming force fields that are often assumed to result from wave propagation in a simple planar fashion. However, the finite realm of a microsystem substantially increases the significance of diffraction, causing a far richer range of physical effects. This work aims to seek an in-depth understanding of the mechanisms arising due to the incidence of a travelling SAW (TSAW), emanating from finite-width interdigitated transducers (IDT), in a microfluidic channel. For particles within a certain size range, the current literature broadly reports continuous unidirectional migration along the TSAW propagation direction [1], however, here we show that this effect is only one amongst many. Through numerical prediction and experimental validation, five distinct acoustofluidic mechanisms have been identified and characterized. The influence of particle size, in particular, is explored.

### Characterization of traveling SAW driven mechanisms

Here, a finite-width IDT with a wavelength of  $21\ \mu\text{m}$  (operating at 180 MHz) is employed to generate TSAWs. Upon interaction of  $1\ \mu\text{m}$  polystyrene particles with the generated TSAW field, five distinct mechanisms are observed (Fig. 1) [2]. In particular, a scenario is realized wherein trapping of particles into stable locations (in two orthogonal directions) occurs, though the periodic nature of this outcome is typically only expected for standing SAW systems. The periodic trapping of particles parallel to the propagation direction in a TSAW system (parallel trapping), is caused by the diffractive effects at the wafer/liquid intersection. This phenomenon is predicted by simulation using finite element analysis (FEA) of a cross-section through the channel, indicating the complexity of the resultant time-averaged absolute pressure field (Fig. 1b). The trapping of particles orthogonal to the SAW propagation direction (orthogonal trapping), however, is caused by the diffractive patterns on the substrate surface due to the finite width of the incident SAW. Additionally, an

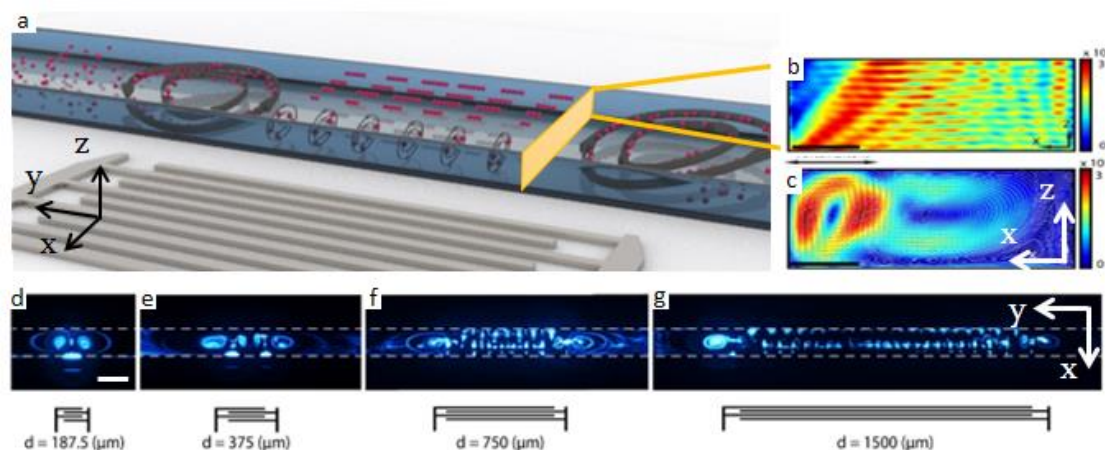


**Figure 1:** (a) Conceptual illustration of SAW-driven mechanisms (b) time-averaged absolute pressure field  $\langle |P_1| \rangle$  across channel width. Scale bar is  $20\ \mu\text{m}$ , (c) streamlines illustrating the simulated streaming field along the channel width.  $\lambda_{\text{SAW}} = 21\ \mu\text{m}$ , Scale bar is  $20\ \mu\text{m}$ , (d-g) Experimental visualization of particles' behavior (top view). Scale bar is  $100\ \mu\text{m}$ .

acoustic streaming field is developed in the irradiated fluid that gives rise to fluid swirling in two orthogonal planes; lateral vortices at the peripheral regions of the SAW beam, here termed peripheral streaming (Fig. 1a), and vertical vortices within the extent of the SAW beam, here termed lobe streaming (Fig. 1a, Fig. 1c). Finally, unidirectional translation of particles appears along the SAW-propagation direction, the most reported effect in such systems. The dominance of these mechanisms, however, depends on the particles' size and their spatial location in the channel.

### Size-dependent behavior of particles

To investigate the size-dependent nature of the diffractive driven mechanisms, here we focus on the central region of the channel, between the peripheral streaming and beyond the extent of the lobe streaming. The present literature predominantly discusses two main behaviors in a TSAW driven system [3]. These include particle drifting along TSAW propagation direction and particle swirling in continuous vortices. However, the periodic trapping of particles induced by TSAW is yet to be fully elucidated. The acoustophoretic mechanisms, discussed above, can cause particles to display three distinct responses as their relative size varies. These include particle drift in the direction of SAW propagation, patterning in stable locations, and continuous motion in circular trajectories along with two transitional regions (Fig. 2) [4]. At a constant frequency and power, particles below a certain size only experience streaming, though their behavior shifts to the first transitional region, i.e. streaming and patterning (Fig. 2c-e), as their size increases, then to the patterning dominant region (Fig. 2f). By further increasing of the size, particles represent the second transitional behavior, i.e. patterning and drifting (Fig. 3g), and beyond a second critical diameter, they only experience drifting (Fig. 2h).

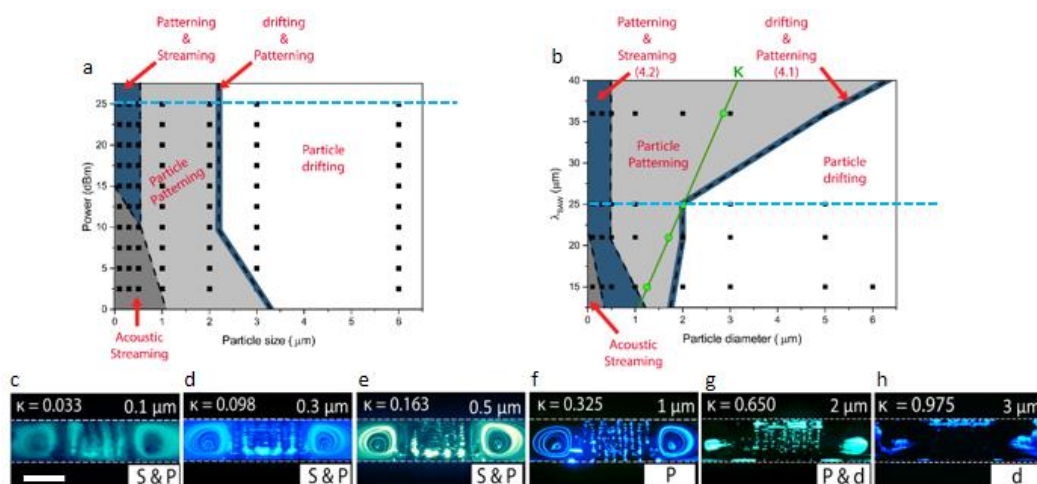


**Figure 2:** The transitional behavior of particles with different diameter as a function of (a) applied power and (b) wavelength of TSAW, where each region (indicated by different colour) shows the dominant mechanism dictating particle behavior. Black squares represent the conducted experiments, dashed lines show the transitional borders, green circles represent the cross-over from streaming dominated to radiation dominated behavior predicted based on  $\kappa$  value (the dimensionless constant) as explained by Skowronek *et al.* [3]. The blue dashed lines show the location of (c-h) experimental observations illustrating the transition in particle behavior as their diameter increases from 0.1  $\mu\text{m}$  to 3  $\mu\text{m}$ . S, P and d are streaming, patterning and drifting respectively. Scale bar is 200  $\mu\text{m}$ .

### Conclusion

The inherent diffractive effects along with the size-dependent acoustic mechanism interplay leads to a diversity in particle behavior within SAW-driven systems. A deeper understanding of these phenomena lays foundational building blocks that unlock new applications that are currently not feasible.

### References

- [1] G. Destgeer, B.H. Ha, J. Park, J.H. Jung, A. Alazzam, and H.J. Sung. *Physics Procedia* **70**, 34-37 (2015).
- [2] A. Fakhfour, C. Devendran, T. Albrecht, D. J. Collins, A. Winkler, H. Schmidt, and A. Neild. *Lab on a Chip* **18**, 2214-2224 (2018).
- [3] V. Skowronek, R.W. Rambach, L. Schmid, K. Haase, and T. Franke. *Analytical chemistry*, **85**, 9955-9959 (2013).
- [4] A. Fakhfour, C. Devendran, A. Ahmed, J. Soria, and A. Neild. *Lab on a Chip* **18**, 3926-3938 (2018).

### Acknowledgement

We gratefully acknowledge support received from the Australian Research Council, Grant No. DP160101263. This work was partially supported by EFRE InfraPro project "ChAMP – Chip-based acoustofluidic Medtech Platform". All devices used in this work were fabricated at the Melbourne Centre for Nanofabrication (MCN).



# Generation of Fast Acoustic-Streaming in Microfluids with Gigahertz Acoustic Actuation

Weiwei Cui<sup>1,2</sup>, Mark Reed<sup>1,2</sup>, and Xuexin Duan<sup>1</sup>

<sup>1</sup> College of Precision Instrument and Optoelectronics Engineering, Tianjin University, China

E-mail: [weiweitsui@tju.edu.cn](mailto:weiweitsui@tju.edu.cn), [xduan@tju.edu.cn](mailto:xduan@tju.edu.cn)

<sup>2</sup> Department of Electrical Engineering, Yale University, United States.

## Introduction

Acoustic actuation for micro/nanoscale fluids have triggered a lot of interesting phenomenon and technologies, which potentially promote the development of life science, chemical synthesis, and medical diagnosis. Predicted by the scale law, increasing the working frequency of acoustic actuation by minimizing the device towards nanoscale may bring more surprise to this field. By merging ultrahigh frequency bulk acoustic wave resonators (BAW) with microfluidic systems, a gigahertz acoustofluidic system is constructed. As shown in Figure 1a, an acoustic device with frequency of 2000 MHz is integrated into a microfluidic chip to stimulate microfluids (the cross-section of the system is shown in Figure 1b). The fabricated device presented in Figure 1c. Particle-tracking experiments shows that fast rotating vortex stream is effectively generated within the microscale confinement. As shown in Figure 1d, there are totally 10 individual vortex “petals” inside the microfluid with a height of 100  $\mu\text{m}$ . Using the fast vortex stream, we developed some applications covering ultrafast mixing [1], micro/nanoscale particle tweezing [2], and cellar/vesicle surgery [3] in the past few years. However, the basic theory of the acoustic-fluids interaction still remains unclear and requires more theoretical and experimental characterizations. Here, the generation of the fast acoustic-streaming is carefully explored with the aim to figure out the physical principle of the ultrahigh frequency acoustofluidic phenomenon.

## Results and Discussions

We firstly present the generation process of acoustic stream based on the Rayleigh-Schlichting model [4] to explore the role of high frequency. As shown in Figure 2, when acoustic waves transport from air or solid into the microscale fluids, there would be standing waves formed inside the channel due to their similar size to the acoustic wavelength. The ultrathin viscous layer on the acoustic-fluid interface stores some energy, which is the driving force to trigger streaming. Generally, the acoustic streaming effect is so weak and even considered as interference factor to the standing wave. When the acoustic frequency goes up to ultrahigh region (300 MHz-3000 Mhz), things becomes different since the size mismatch between acoustic wave and microchannel. For 2000 MHz acoustic wave used in this work, the acoustic wave would decay within 7  $\mu\text{m}$ , resulting in no standing waves formed in the microfluidic (tens of micrometers). Meanwhile, the acoustic stimulation energy is mainly stored inside the viscous layer and plays a role in generating fast acoustic-stream.

Additionally, the process was described from the view of mechanical interaction. The vibrating amplitude of the BAW device is generally 1~10 nm (depending on the working power), which, however, has an acceleration up to an amazing value of  $10^{10}$   $\text{m/s}^2$ . We investigated the body force ( $F_B$ ) and conducted the expression as presented in the following.

$$F_B = \rho A^2 b \omega^4 / \rho_l c_l^3 \quad (1)$$

In equation (1),  $\rho$  and  $c_l$  represent the density and acoustic speed of the fluid respectively;  $A$  is the amplitude of the vibrating acoustic-fluid interface;  $b = 4/(3\mu + \mu')$  is a function of the dynamic ( $\mu$ ) and bulk ( $\mu'$ ) viscosity. Equation (1) reveals that body force scales with  $\omega^4$ . Figure 3a present the calculated body force distribution along the acoustic traveling direction. Such a strong body force gives rise to a jet flow above the acoustic source and a pair of closed vortices beside the boundaries. The finite simulation in Figure 3b furtherly present the vortex velocity field inside the acoustofluidic system. From the simulation, stream velocity up to the order of m/s is achieved.

## Conclusions

In conclusion, this study figures out the importance of frequency for micro/nanoscale fluidic streaming. By immersing the 2000 MHz acoustic waves into the microfluids, fast rotating vortex stream was effectively triggered with a velocity on the order of m/s. Both of indirect analysis based on the Rayleigh-Schlichting model and direct conduction on the body force give us a first impression on the ultrahigh frequency acoustofluidics. Even though, there are still many details about the theory needed to study for a deep understand of the acoustic-fluid interaction physics.

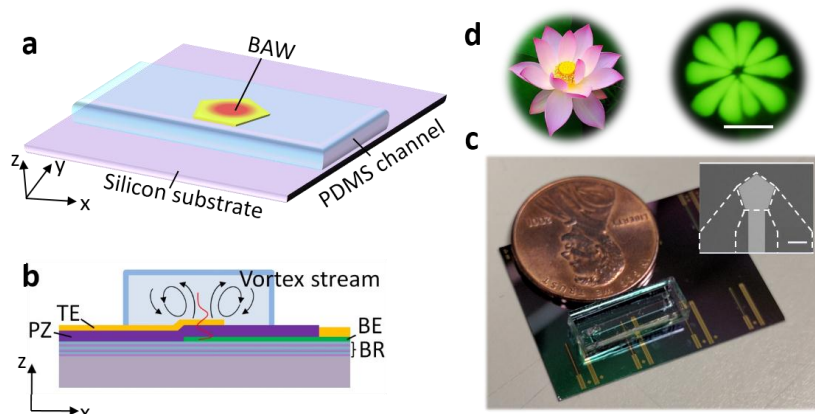


**Figure 1.** Schematic of (a) the gigahertz acoustofluidic chip and (b) its cross-section view. (c) Packaged chip with an inserted SEM photo of the 2000 MHz acoustic device. (d) Formation of the gigahertz acoustic triggered flower-shape vortex array. Green fluorescence labelled 210 nm nanoparticles were used. Scale bars in (c) and (d) are respectively 100  $\mu\text{m}$  and 150  $\mu\text{m}$ .

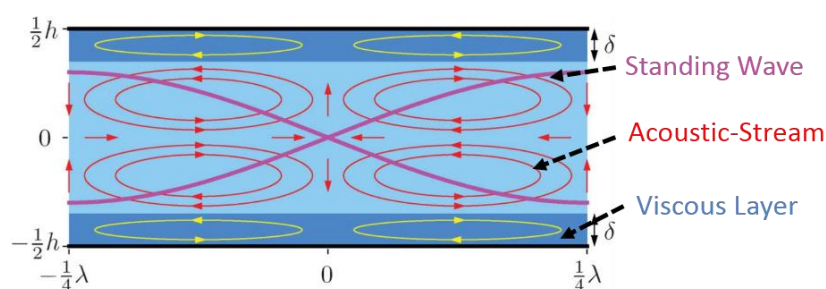


**Figure 2.** Schematic of the Rayleigh-Schlichting stream model [4]. Reproduced with permission. Copyright 2012 The Royal Society of Chemistry

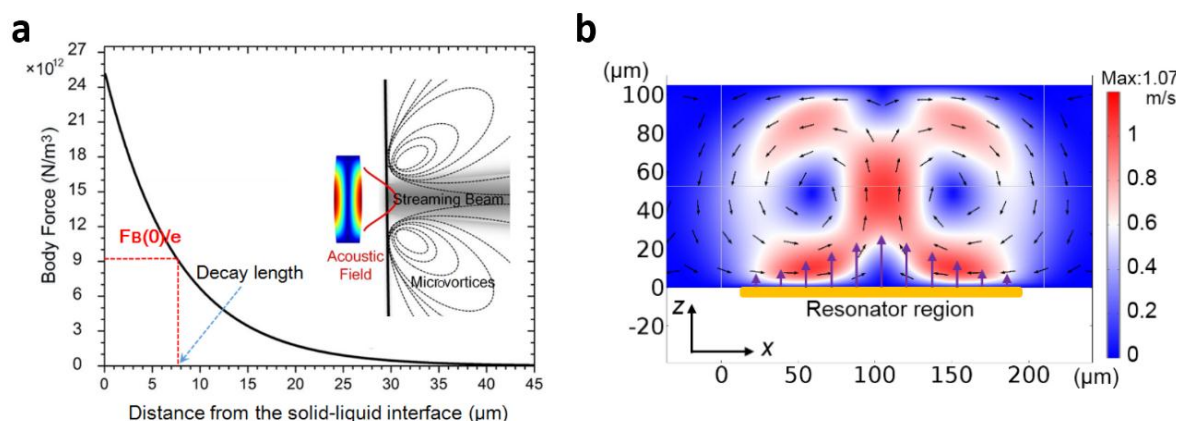


**Figure 3.** (a) Body force distribution above the SMR surface. The decay length is labelled where the body force decreases to  $1/e$  of the initial value. A two-dimensional finite element simulation of the acoustic field across the red line on the resonator presents the distribution of body force on the surface. And ultra-great body force generates a streaming beam into the liquid to drive the liquid above the SMR away. According to the mass continuous equation, the liquid from the surround would flow to the surface of the SMR and finally forms a closed rotating vortex. (b) Velocity field of the gigahertz acoustic-stream realized by COMSOL simulation.

## Reference

- [1] W. Cui, H. Zhang, H. Zhang, Y. Yang, M. He, H. Qu, W. Pang, D. Zhang, X. Duan, *Applied Physics Letters* **109**, 253503 (2016).
- [2] W. Cui, M. He, Y. Yang, H. Zhang, W. Pang, X. Duan. *Particle & Particle Systems Characterization* **1800068** (2018).
- [3] Z. Zhang, W. Wang, H. Zhang, Z. Tang, W. Liu, Y. Lu, Z. Wang, W. Pang, H. Zhang, D. Zhang, X. Duan. *Small*, **13(18)**, 1602962(2018).
- [4] P. B.Muller, R. Barnkob, M. J. H. Jensen, H. Bruus, *Lab on a Chip* **12**, 4617-4627(2012).



## Poration effects induced by gigahertz acoustic streaming: from lipid bilayers to vesicles and cells

Yao Lu <sup>a,b</sup>, Nico Overeem <sup>b</sup>, Xuexin Duan<sup>\*,a</sup>, Hongxiang Zhang <sup>a</sup>, Hao Zhang <sup>a</sup>, Wei Pang <sup>a</sup> and Jurriaan Huskens<sup>\*,b</sup>

<sup>a</sup> State Key Laboratory of Precision Measuring Technology & Instruments, Tianjin University, Tianjin 300072, China.

<sup>b</sup> Molecular Nanofabrication group, MESA+ Institute for Nanotechnology, University of Twente, 7500 AE, Enschede, The Netherlands.

Email: [xduan@tju.edu.cn](mailto:xduan@tju.edu.cn), [j.huskens@utwente.nl](mailto:j.huskens@utwente.nl)

### Introduction

In the past decades, membrane-disruption methods have been proposed as an important physical approach to address a subset of functions, specifically nucleic acid delivery to the certain primary cells.[1, 2] Recently, numerous studies have been focusing on the precision membrane disruption at the micro and nanoscale aiming to surmount current delivery limitations.[3, 4] In this work, hypersonic poration induced by the gigahertz (GHz) acoustic streaming is introduced as a new physical method to precisely control membrane permeability. The bulk acoustic wave (BAW) resonator was fabricated using microelectromechanical system (MEMS) technologies to generate hypersound of GHz frequency. The mechanism of streaming induced-hypersonic poration is analyzed step by step using a variety of model systems, from the supported lipid bilayer (SLB), to giant unilamellar vesicles (GUVs) and cancer cells. These experiments have provided a deep insight into the formation of hypersonic nanopores from planar lipid membranes to complex cell systems. This innovative poration method has the potential to be applied for intracellular delivery and other biomedical applications.

### Theory Consideration

The schematic of the bulk acoustic wave (BAW) resonator to generate hypersound is shown in Figure 1a and 1b. As the top view of the BAW resonator shows, a pentagonal-shaped electromechanical resonator with a working frequency of 1.56 GHz was designed and fabricated. The resonant part was composed of a piezoelectric layer sandwiched between two electrodes (sectional view in Figure 1b). When excited by a sinusoidal electric signal, hypersound of GHz frequency was generated, the propagation and attenuation of which would induce high-speed acoustic streaming in solution. Here, a 3D finite element model (FEM) was employed for theoretical simulations of the GHz acoustic streaming (Figure 1c). The liquid below the working area of the resonator will be accelerated, thus generating pressure on the lipid bilayer, vesicles or cells and inducing hypersonic poration on these soft materials.

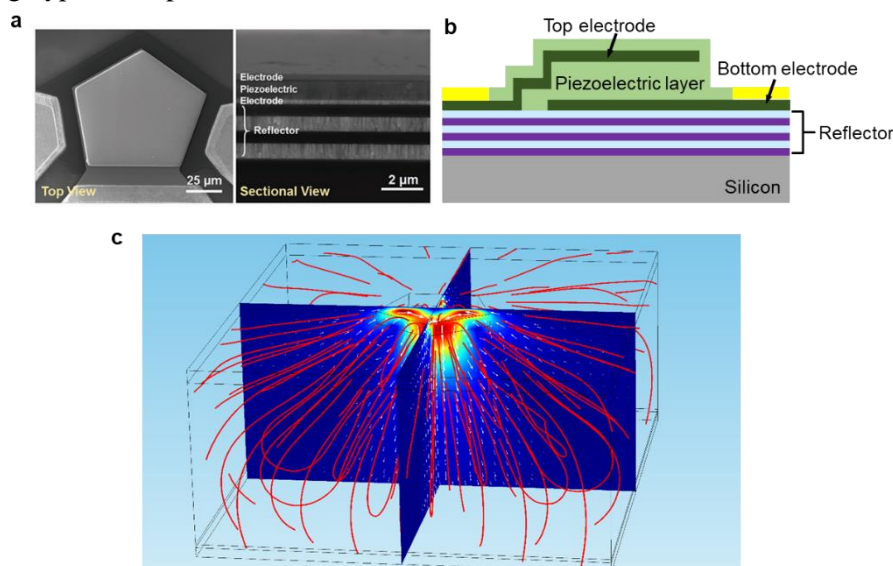


**Figure 1:** (a) SEM images of the polygon-shaped BAW resonator. The BAW resonator is a film-stacked structure with a piezoelectric layer of AlN sandwiched between two Mo electrodes. (b) Sectional view of the BAW resonator. (c) FEM simulations of the acoustic streaming induced by hypersound in solution. The frequency of the BAW resonator was 1.56 GHz. The power of hypersound was 250 mW.

### Hypersonic poration in different systems

As shown in Figure 2a, in the system of the supported lipid bilayer (SLB), the ion current through the SLB was generated by switching on hypersound and then recovered to the original value when the stimulation was switched off, and the ion current increased accordingly by improving the input power of hypersound. These results indicate that the GHz acoustic streaming induced by hypersound facilitated the SLB to become conductive by changing its membrane permeability, which can be attributed to hypersonic poration. Furthermore, in the system of giant unilamellar vesicles (GUVs), hypersound was applied to study the encapsulation of positively charged polystyrene (PS) beads into negatively charged GUVs under hypersound. As shown in Figure 2b, by switching on the hypersound of 300 mW, the blue fluorescence, emitted from 50 nm PS beads, was observed inside the GUV, suggesting that the PS beads of 50 nm were successfully taken up by GUVs upon applying hypersound, which in turn verifies the formation of transient nanopores induced by the GHz acoustic streaming from hypersound. It was found that the orange fluorescence, emitted from the PS beads of 100 nm, was also observed inside the GUV under hypersound of 300 mW. Finally, this acoustic method was applied to the cell system for drug delivery. As shown in Figure 2c, the red fluorescence emitted by Dox molecules was distributed in the HeLa cells after exposure to hypersound of 500 mW for 10 or 20 min, which indicates that a detectable quantity of Dox-loaded mesoporous silica nanoparticle (MSN) was internalized into the cells within this short time. In a control experiment, HeLa cells were incubated with the same amount of Dox-loaded MSNs without any hypersonic treatment for 10 or 20 min. The fluorescence intensity of Dox in these cases was much lower compared to that in the presence of hypersound.

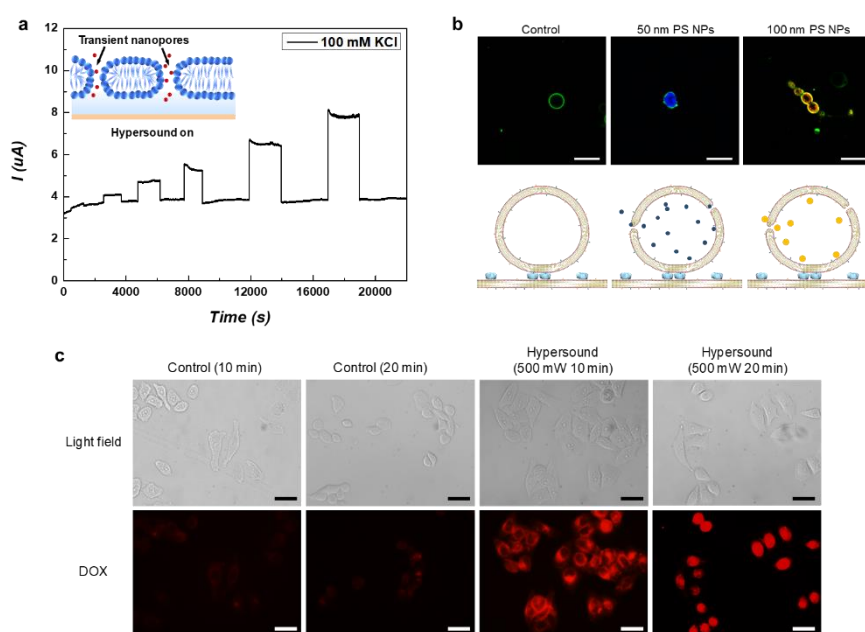


**Figure 2:** (a) Real-time detection of ion current through the SLB in 100 mM KCl solution by alternately switching on and off hypersound (the input powers were successively 10, 20, 32, 50, 100, 250 and 500 mW). Illustration of the formation of transient pores in the SLB in the inserted cartoon image. (b) Confocal laser scanning microscopy (CLSM) images of Top Fluor-labeled GUVs encapsulated with positively charged PS beads of 50 nm (blue fluorescence) and 100 nm (orange fluorescence) without (control) or with (300 mW) the stimulation of hypersound. Scale bars indicate 10  $\mu\text{m}$ . (c) Fluorescence images of the intracellular uptake and distribution of Dox-loaded PMSNs in HeLa cells. For the hypersound-treated groups, HeLa cells were incubated with Dox-loaded PMSNs and exposed to hypersound of 500 mW for 10 or 20 min. For the control group, HeLa cells were incubated with Dox-loaded PMSNs without any hypersonic treatment for 10 or 20 min. Scale bars indicate 20  $\mu\text{m}$ .

### Conclusion

In this work, the GHz acoustic streaming induced by hypersound has been applied to induce hypersonic poration in different assembled systems, including the supported lipid bilayer (SLB), giant unilamellar vesicles (GUVs), and cells. By carefully inducing shear stress by acoustic pressure, transient nanopores can be created in the membrane to obtain reversible membrane disruption. The application of this physical poration method can be directed toward controlled release/encapsulation and triggered intracellular delivery. On the other hand, when hypersonic poration is applied to a cell system, it can be used to control the permeability of cell membranes to enhance drug delivery.

### References

- [1] M. P. Stewart, A. Sharei, X. Ding, G. Sahay, R. Langer, K. F. Jensen, *Nature*, **538**, 183 (2016).
- [2] Y. C. Wu, T. H. Wu, D. L. Clemens, B. Y. Lee, X. Wen, M. A. Horwitz, M. A. Teitell, P. Y. Chiou, *Nat. Methods*, **12**, 439 (2015).
- [3] B. Judkewitz, M. Rizzi, K. Kitamura, M. Häusser, *Nat. Protoc.* **4**, 862, (2009).
- [4] S. Wang, L. J. Lee, *Biomicrofluidics*, **7**, 011301 (2013).



## Electrically driven instabilities in thin films

Élfego Ruiz-Gutiérrez<sup>1</sup>, and Rodrigo Ledesma-Aguilar<sup>1</sup>

<sup>1</sup>Smart Materials and Surfaces Laboratory, Northumbria University, Newcastle upon Tyne, UK.  
E-mail: [elfego.r.gutierrez@northumbria.ac.uk](mailto:elfego.r.gutierrez@northumbria.ac.uk)

### Introduction

When a voltage difference is applied between a conducting liquid and a conducting (solid) electrode, the liquid is observed to spread on the solid [1]. This phenomenon, generally referred to as electrowetting, has become a widely used technique to manipulate multiphase flows. This is due to the range of operating scales in which the technique can be applied, and notably due to the relatively fast response of the fluids to electrical actuation. Despite these important advances, the rich phenomenology of electrowetting remains to be fully understood [3]. Usually, one fluid is a conductor immersed in an ambient dielectric fluid. During electrowetting actuation, the conducting liquid is drawn towards the electrodes and then spreads (see Fig. 1(a)). During the actuation of liquids, the ambient fluid may form a thin film underneath the droplets that can become unstable and break up into small “bubbles” that remain in contact with the solid [2]. Such a transition introduces mobile contact lines, which can drastically affect the friction force acting on its overall dynamics. In this contribution, we explore the dynamical behaviour of contact lines driven by electrowetting.

### Methodology and Analysis

To model the dynamics, it is essential to develop computational methods that capture the multiphase fluid dynamics and that resolve the effect of electrostatic interactions, as these can help interpret experiments and inform theory. The lattice-Boltzmann method (LBM) has proved to be a powerful tool to study multiphase fluid dynamics [4]. For this, we equipped our LBM with a solver of the electric potential field, which allows us to analyse in detail the competition between viscous, capillary and electrostatic forces that act on the droplet [5]. We validate the method by comparing the electrowetting-induced spreading of a droplet to the classical theory of Young and Lippmann (inset in Fig. 1(a)).

We first analyse the stability of a liquid film of dielectric fluid that separates an electrically grounded solid conductor and an electrolytic solution at voltage  $V_0$ , as shown in Fig. 1(b). Using this setup we can model the stability of a static film and analyse the competition between capillary forces, that flatten the interface and the electric forces that destabilise it as a preliminary result.

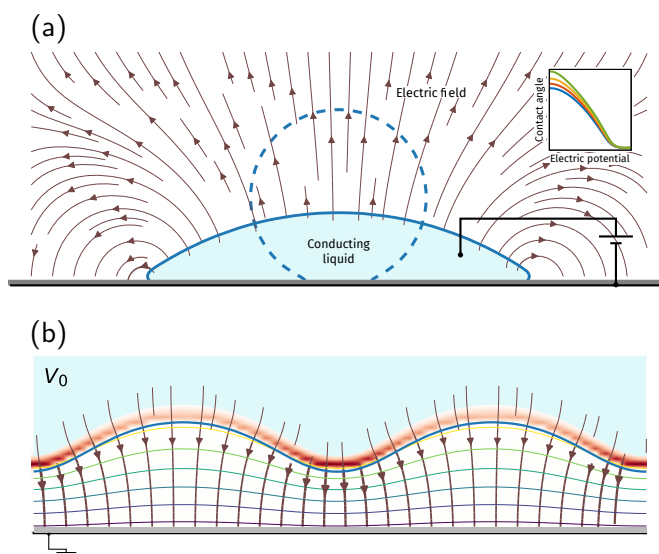


**Figure 1:** Lattice-Boltzmann simulation of electrowetting phenomena. A fluid of conducting fluid (light blue) is set to a voltage  $V_0$  against a grounded electrode on the bounding surface. This produces an electric field (stream lines) and an induced charge shown by the dark-red colour map. (a) Basic electrowetting on dielectric (EWOD). A droplet is raised at an electric potential with respect to an underneath solid surface causing it to spread. (b) Simulation setup of a thin dielectric film where the interface is perturbed in a sinusoidal shape.

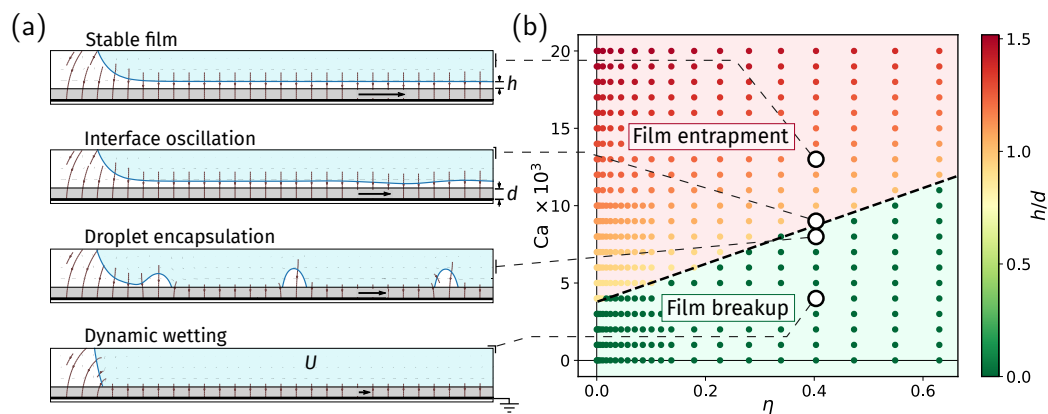


**Figure 2:** Lattice-Boltzmann simulations of contact line motion. (a) Spreading of a conducting fluid. At low speeds, a stable film oil of thickness  $h$  is entrapped between the droplet and the solid. As the speed is reduced the film develops oscillations driven by the electric field, which eventually develop as droplets. For sufficiently low speeds the film completely disappears and a stable contact line advances on the solid. The vertical axis has been expanded  $2\times$  for visibility. (b) Film-entrapment and film breakup regimes as a function of the capillary and electrowetting numbers. The configurations reported in (a) are indicated by the empty circles.

### The effect of electric forces in dynamic wetting

With the aid of the simulations, we now turn to investigate the effect of electric forces in dynamic wetting. For this, we consider a solid surface that moves at velocity  $U$  with respect to the front of a conducting liquid. The viscosity of the dielectric phase is set to four times the viscosity of the conducting fluid. We model the thin dielectric layer separating the liquids from the electrodes as a solid layer of uniform electric permittivity.

Panel (a) in Fig. 2 shows four representative examples of the configuration of the fluid-fluid interface as it moves with speed  $U$  with respect to the dielectric floor. For sufficiently large  $U$ , a stable oil film of constant thickness,  $h$ , is entrapped between the droplet and the solid wall. Decreasing the speed of the front with respect to the floor leads to a reduction of the thickness of the film, which might develop perturbations that grow as they travel downstream. These perturbations have a destabilising effect on the film, which eventually breaks up into small drops as the conducting fluid reaches the solid and creates a contact line. Once a contact line is formed, there is a range of speeds where the contact line lags behind the rest of the interface, leading to the deposition of droplets. Finally, at sufficiently low  $U$ , the speed of the contact line matches the rest of the interface, and the motion proceeds as dynamic wetting. The same transition from film-entrapment to dynamic wetting, as the front speed is reduced, occurs for different values of the applied potential. This is summarised in the phase diagram in Fig. 2 showing the thickness of the film for a given capillary number ( $\propto U$ ) and the electrowetting number ( $\propto V_0^2$ ).

### Conclusion

We have looked into the dynamics of thin films where electric fields are present and then into the dynamics of contact lines during an electrically-enhanced wetting. We have observed that the mobility of liquid fronts during electrowetting-dewetting is controlled by the film entrapment and contact-line motion, and the timescale of the large-scale flow. We expect that these results can be generalised to the behaviour of contact lines driven by electrowetting for a wide variety of applications, for example, in microfluidic platforms liquid displays.

### References

- [1] G. Lippmann, *Ph.D. thesis*, Gauthier-Villars, 1875.
- [2] A. Staicu and F. Mugele, *Phys. Rev. Lett.*, **97**, 167801, (2006).
- [3] F. Mugele, *Soft Matter*, **5**, 3377–3384, (2009).
- [4] T. Krüger, et al., *The Lattice Boltzmann Method: Principles and Practice*, Springer, 2016.
- [5] É. Ruiz-Gutiérrez and R. Ledesma-Aguilar, *Langmuir*, **35**, 4849–4859, (2019).



## Segregation in binary component droplet evaporation

Yaxing Li<sup>1</sup>, Christian Diddens<sup>1,2</sup>, Pengyu Lv<sup>1</sup>, Herman Wijshoff<sup>3</sup>, Michel Versluis<sup>1</sup>, and Detlef Lohse<sup>1,4</sup>

<sup>1</sup>Physics of Fluids group, Department of Science and Technology, Mesa+ Institute, Max Planck Center for Complex Fluid Dynamics and J. M. Burgers Center for Fluid Dynamics, University of Twente, P. O. Box 217, 7500 AE Enschede, Netherlands

E-mail: yaxing.li@utwente.nl

<sup>2</sup>Department of Mechanical Engineering, Eindhoven University of Technology, P.O. Box 513, 5600 MB Eindhoven, The Netherlands

<sup>3</sup>Océ Technologies B.V., P.O. Box 101, 5900 MA Venlo, The Netherlands

<sup>4</sup>Max Planck Institute for Dynamics and Self-Organization, 37077 Göttingen, Germany

The evaporation of a multicomponent microdroplet on a flat substrate has attracted a lot of attention recently [1,2], because of not only its beautiful fluid dynamics, but also its relevance in various technological applications. The complexity of a drying mixture system originates from the selective evaporation caused by the different volatilities of the components. The variation of the compositions due to selective evaporation may lead to instabilities: segregation of components. A paradigmatic system is so called “ouzo droplet” [3], which is a mixture of water, ethanol and oil with a certain equilibrium concentration. During the evaporation, the high volatility of ethanol varies the concentration ratio among the three liquids, oil nucleates as microdroplets and separates from the ternary system. Liquid-liquid separation during evaporation not only occurs for Ouzo drops but is omnipresent in nature and technology.

Recently, we studied two evaporating binary droplet systems, namely 1,2-hexanediol/water and glycerol/water mixture, which both involve segregation, but reveal completely different mechanisms. Note that 1,2-hexanediol and glycerol are both miscible with water in equilibrium state, but almost non-volatile in room condition as compared to water. For 1,2-hexanediol/water droplets [4], we observe an evaporation-triggered segregation of 1,2-hexanediol during the drying process, as shown in Fig. 1. The visualization of the flow field by PIV reveals that the Marangoni flow caused by the surface tension difference between water and 1,2-hexanediol, is too weak to remix the high concentration of 1,2-hexanediol at the droplet rim, eventually leading to segregation. For glycerol/water droplets [5], we show that in spite of the small droplet size (submillimeter,  $Bo \ll 1$ ), gravitational effects play a crucial role in controlling the flow fields by observing opposite radial flow directions for sessile and pendant droplets with PIV, as shown in Fig. 1. We reveal that the effect originates from the density gradient in the droplet bulk caused by the preferential evaporation of water component and propose Archimedes number  $Ar$  as the relevant nondimensional control parameter.

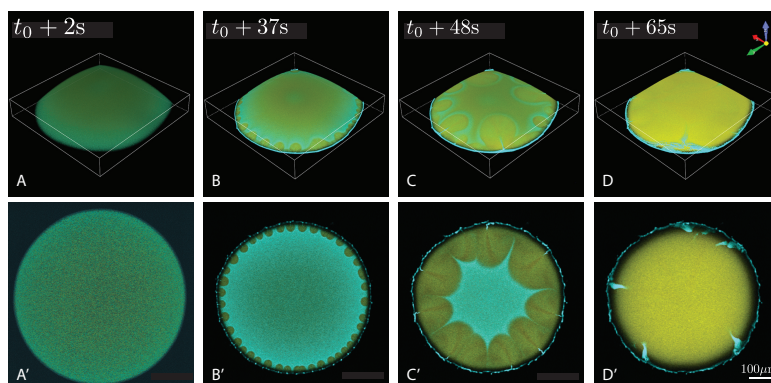


**Figure 1:** Confocal images of the segregation process during droplet evaporation in a semi-sideview (A-D) and bottom view (A'-D') taken at the same times. (A-D) The confocal microscope scans the rectangular box with the volume  $590 \mu\text{m} \times 590 \mu\text{m} \times 90 \mu\text{m}$ . Water (blue) and 1,2-hexanediol (yellow) are labeled with different dyes for the observation. (A and A') In the beginning, the droplet is homogeneously mixed. (B and B') At about 34 s after recording started, 1,2-hexanediol nucleates at the contact line of the droplet, which is revealed as yellow round shapes. (C and C') The nucleated microdroplets of 1,2-hexanediol gradually grow and coalesce. (D and D') The evaporation ends when 1,2-hexanediol fully covers the surface of the droplet.

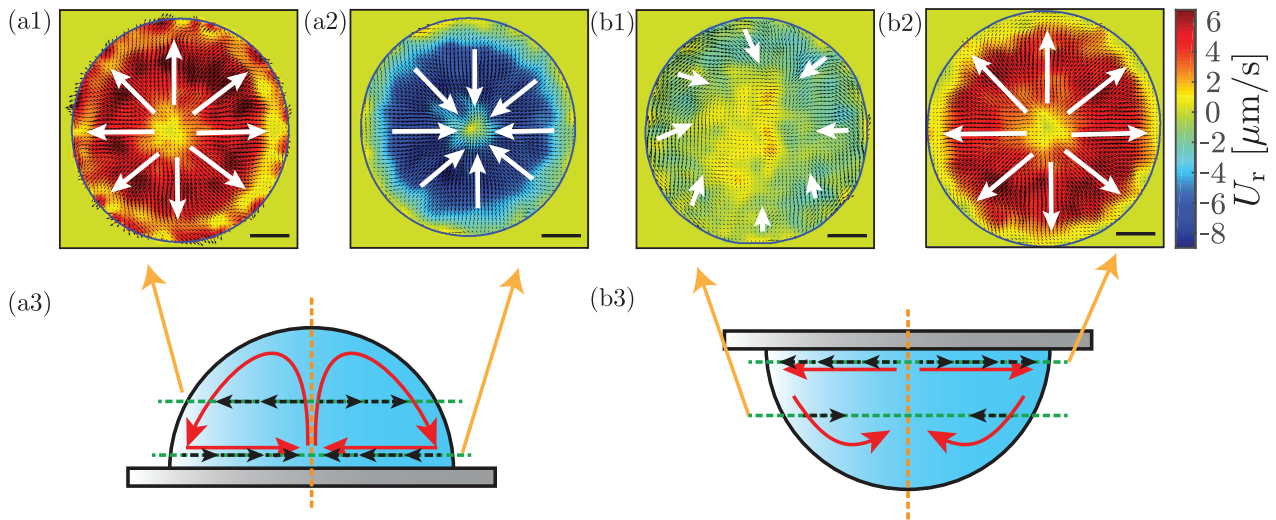


**Figure 2:** The micro-PIV measurement of flow fields in both sessile (a) and pendant (b) droplets. The scale bars represent  $200 \mu\text{m}$ . (a1 and a2) Flow fields in a sessile binary droplet measured at different heights:  $200 \mu\text{m}$  and  $10 \mu\text{m}$  away from the substrate, respectively. The white arrows represent the flow direction. (a2) The measurement near the substrate shows an inward radial flow, (a2) the one at larger height reveals an outward radial flow. (b1 and b2) Flow fields of a pendant binary droplet measured by the same method as the sessile droplets. (b2) The flow near the substrate follows outward radial direction, (b1) but the flow at midheight reveals an annular flow with deviations from axisymmetry near the edge and irregular flow within the inner part. The four PIV images were taken with four different droplets. (a3 and b3) The schematics of the flow pattern in side views of both sessile and pendant droplets.

## References

- [1] R.D. Deegan, O. Bakajin, T.F. Dupont, G. Huber, S.R. Nagel, and T.A. Witten. *Nature* **389**, 827 (1997).
- [2] H. Kim, F. Boulogne, E. Um, I. Jacobi, E. Button, and H. A. Stone. *Phys. Rev. Lett.* **116**, 124501 (2016).
- [3] H. Tan, C. Diddens, P. Lv, J. G. M. Kuerten, X. Zhang, and D. Lohse. *Proc. Natl. Acad. Sci. U.S.A.* **113**, 8642 (2016).
- [4] Y. Li, P. Lv, C. Diddens, H. Tan, H. Wijshoff, M. Versluis, and D. Lohse. *Phys. Rev. Lett.* **120**, 224501 (2018).
- [5] Y. Li, C. Diddens, P. Lv, H. Wijshoff, M. Versluis, and D. Lohse. *Phys. Rev. Lett.* **122**, 114501 (2019).



## Fast spreading of a droplet on a thin soap film

M. Motaghian<sup>1</sup>, R. Shirsavar<sup>2</sup>, E. van der Linden<sup>1</sup>, H. A. Stone<sup>3</sup>, D. Bonn<sup>4</sup>, M.Habibi<sup>1</sup>

<sup>1</sup>Physics and Physical Chemistry of Foods, Wageningen University, Wageningen, The Netherlands

E-mail: Melika.Motaghian@wur.nl

<sup>2</sup>Department of Physics, Faculty of Science, University of Zanjan, Zanjan, Iran

<sup>3</sup>Department of Mechanical and Aerospace Engineering, Princeton University, Princeton, NJ 08544, USA

<sup>4</sup>Institute of Physics, van der Waals-Zeeman Institute, University of Amsterdam, Science Park 904, 1098 XH Amsterdam, The Netherlands

### Introduction

Spreading a deposited droplet over a solid or liquid surface has received great attention in the past decades due to its importance in many different applications ranging from coating [1] to depositing pesticides on the plant leaves[2]. Although spreading has been studied under various conditions, spreading a droplet on a soap film of a few micrometres thickness, suspended in the air, hasn't been studied yet. In this method since liquids are suspended in the air, no-slip boundary condition doesn't apply anymore and viscous dissipation on the surface boundaries are minimized. We aim to understand how different parameters including surface tension of the droplet govern the dynamics of the spreading in this geometry.

### discussion:

In order to make a horizontal soap film we used sodium dodecyl sulfate (SDS) solution. Droplets of ammonium lauryl sulfate (ALS) solution with a range of concentrations (therefore range of surface tensions) were deposited on the initial soap film. In all cases when the droplet touches the soap film, it triggers a mechanical wave which propagates over the soap film. Sequence of photos in Fig.1(left) shows the evolution of this mechanical wave on the soap film. By measuring the radius of the spreading front in time, speed of the mechanical wave can be calculated. Fig.1 (Right) shows radius of mechanical wave as a function of time for soap film of 0.005 M SDS in experiment with different droplets.

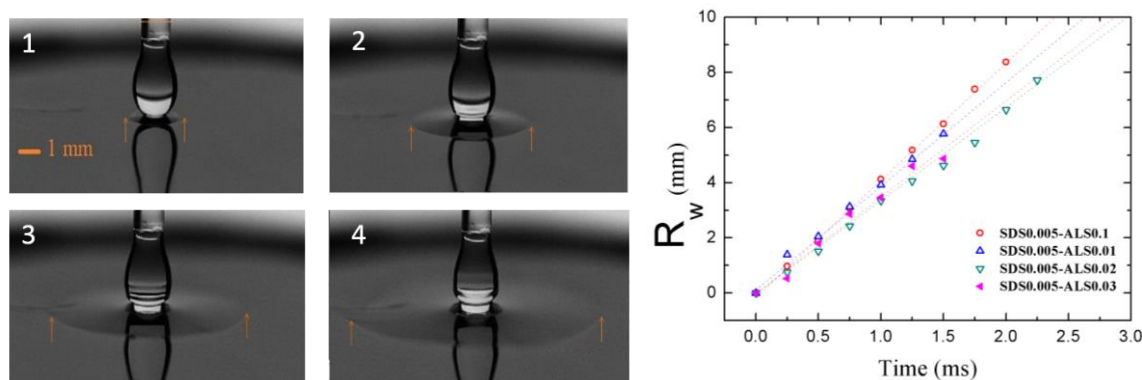


**Figure 1:** (Left) Immediately after droplet touches the soap film, a fast mechanical wave travels over the initial soap film. Images are captured at 1, 1.5, 2 and 2.5 ms after droplet touches the soap film. (Right) radius of mechanical wave as a function of time for soap film of 0.005 M SDS in different experiments.

On the other hand we know the speed of a mechanical wave on an elastic sheet is given by  $v = \sqrt{T/\rho h}$  where  $T$  is the tension in the sheet,  $\rho$  is the density and  $h$  is the thickness of the sheet. Here we have a fluid sheet (made of 0.005 M SDS) with surface tension of  $T \sim 47$  mN/m and density of water. Substituting these parameters into the above relation and also the average speed of the wave (calculated from fitted lines to data in Fig.1 right), gives the thickness of the soap film in each experiment. For the mechanical waves reported in the Fig.1 (right) thickness of the soap film was calculated 3.4, 2.6, 4.2 and 3.9  $\mu\text{m}$  for experiments with droplets Of ALS 0.1, 0.01, 0.02 and 0.03M respectively.

After initial touch, droplet formed a new layer in the center of the soap film. In the cases that surface tension of the droplet was lower than the soap film, the droplet was stretched by the soap film resulting in a fast spreading. Evolution of the spreading front was recorded using a high speed camera. When the surface tension of the droplet was equal to or higher than the soap film, although spreading was not energetically favorable for the system, a slow spreading was observed. Examples of radius of spreading front as a function of time for droplets with different concentration of ALS is shown in Fig.2. all the data sets followed a power-law behavior ( $R \propto t^\alpha$ ) with the exponent  $\alpha$  ranging from 0.1 to 1.

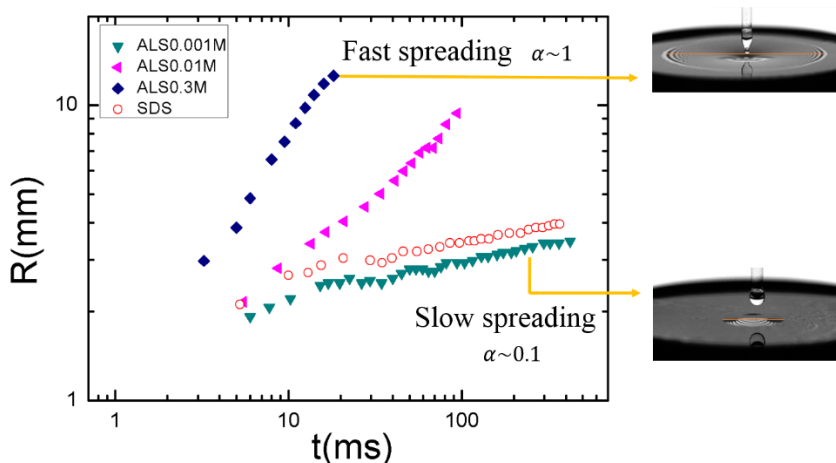


**Figure 2:** Droplet radius versus time for droplets of ALS with different concentrations (solid symbols) and SDS (open symbols) on a soap film of 0.005M SDS. All data sets showed a power law behavior ( $R \propto t^\alpha$ )

An interesting result was observed when a droplet of SDS solution was deposited on the soap film of the same solution. In many previous studies it has been shown theoretically [3] and experimentally [4] that when two droplets of the same solution are brought into contact, surface tension joins them into one bigger drop with a lower surface area. In contrary, in our experiments the deposited droplet stayed intact in the center of the soap film and only spread slowly in time. In the Fig.3 droplet of SDS is shown in the center of the soap film of the same solution, 100 ms after deposition.

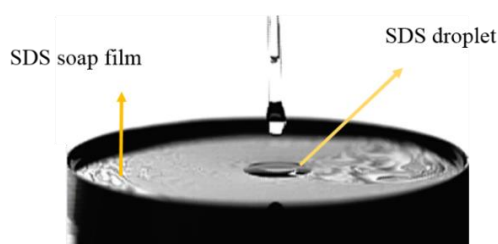


**Figure 3:** A droplet of 0.005 M SDS is deposited on the same soap film. After deposition a liquid lens is formed that spreads slowly in time.

### Conclusion:

Spreading a droplet on a soap film was studied. When a droplet touches a soap film at first a mechanical wave propagates over the soap film. Speed of this mechanical wave was measured and enabled us to calculate the thickness of the soap film. After initial mechanical wave, for the droplets that the surface tension difference between the droplet and the soap film was not favorable for spreading a slow spreading occurred with exponent  $\alpha$  close to 0.1 resembling Tanner's spreading. When surface tension of the droplet was lower than the soap film, surface tension difference drove a fast spreading with the exponent  $\alpha$  ranging from 0.4 to 1.

### References

- [1] Zhang, Z., B. Peng, X. Ji, K. Pei and P. K. L. Chan, *Advanced Functional Materials* **27**(37): 1703443 (2017)
- [2] Bergeron, V., D. Bonn, J. Y. Martin and L. Vovelle, *Nature* **405**: 772 (2000).
- [3] Eggers, J., J. R. Lister and H. A. Stone, *Journal of Fluid Mechanics* **401**: 293-310. (1999).
- [4] Aarts, D., H. Lekkerkerker, H. Guo, G. H. Wegdam and D. Bonn, *Physical Review Letters* **95**(16): 164503 (2005).



## Hydrodynamics of prey capture in ciliated micro-swimmers

Mads Rode<sup>1</sup>, Thomas Kiørboe<sup>2</sup>, and Anders Andersen<sup>1</sup>

<sup>1</sup>Department of Physics and Centre for Ocean Life, Technical University of Denmark  
E-mail: [madsrod@fysik.dtu.dk](mailto:madsrod@fysik.dtu.dk), URL: <http://www.fysik.dtu.dk/complex>

<sup>2</sup>National Institute of Aquatic Resources and Centre for Ocean Life, Technical University of Denmark

### Introduction

Unicellular micro-swimmers play a key role in the biological processes in the ocean. Through grazing on phytoplankton and bacteria, these planktonic organisms have major impact on the global biogeochemical cycles, and by being grazed, they transfer primary production to higher trophic levels. The key process of resource acquisition, i.e., how micro-swimmers capture their prey, remains unexplored for most forms and the physical mechanisms by which micro-swimmers nevertheless clear huge volumes of water for prey are not fully understood. During the last three decades, only few studies have added knowledge to the pioneering work of Tom Fenchel that significantly progressed our understanding of the functional ecology of flagellated and ciliated micro-swimmers [1,2].

Here we will focus on the ciliated micro-swimmer *Euplotes vannus*. Ciliates are unicellular organisms that use slender strands (cilia) to propel themselves and capture prey. The cilia can be distributed over the cell body, organized as bundles (cirri) with 10 - 20 cilia acting together as a unit, or arranged in rows to form bands or membranelles. *Euplotes vannus* generates a strong feeding flow and retains prey particles using cirri and membranelles with complex beat patterns, and the retained prey particles are transported to the mouth region to be ingested. In this presentation we describe the hydrodynamics of the prey capture to answer the question of how the flow-rate of the feeding flow and the prey size spectrum depend on cilia motion and membranelle design.

### The ciliated micro-swimmer *Euplotes vannus*

*Euplotes vannus* has a typical cell length of 100  $\mu\text{m}$ , and width of 50  $\mu\text{m}$  when viewed ventrally (towards the side where the mouth region is located) or dorsally (towards the side opposite to the mouth region) (Fig. 1). In profile the height is typically a quarter of the cell length. On the ventral side the organism is equipped with approximately 20 cirri and a membranelle zone with a sequence of approximately 50 membranelles. The membranelles start at the front of the organism, twist towards the center of the cell, and end at the mouth region. Each membranelle consists of a row of cilia. The organism is observed to both swim freely and crawl or sit on solid surfaces. When swimming, both cirri and membranelle zone are observed to be active, and until now no prey capture has been observed during swimming. When crawling, large cirri at the front and back are in contact with the surface, while

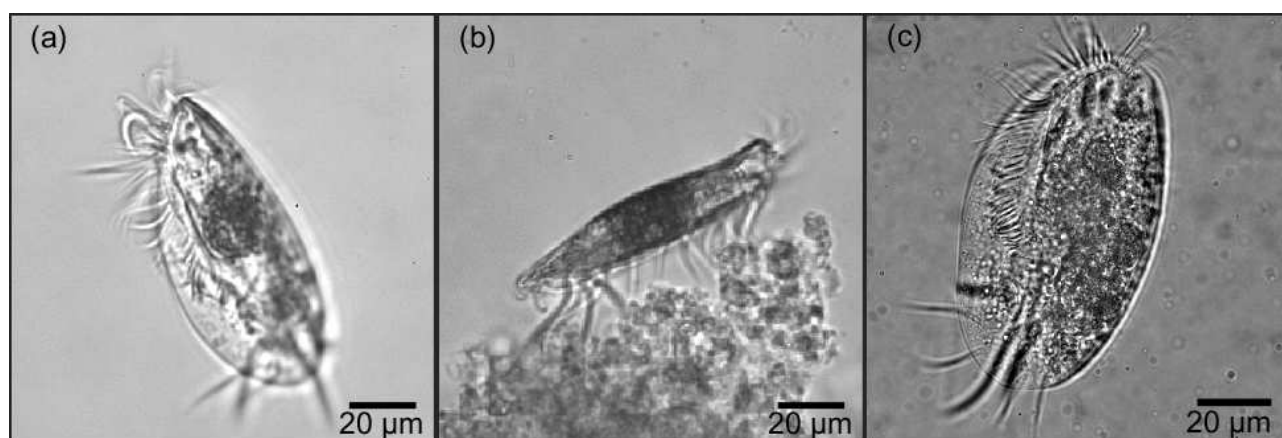


**Figure 1:** Microscope images of *Euplotes vannus*. (a) Dorsal view of a freely swimming individual with the front part of cell and membranelle zone in focus. (b) Right profile view of an individual crawling from left to right on a lump of material with a number of large cirri in contact with the material. (c) Ventral view of a crawling individual on the cover glass in the microscope. The membranelle zone can be seen to the left, starting at the front of the cell (up) and twisting towards the center of the cell. Large cirri are visible on the back.

other cirri and the membranelle zone are active. When sitting, the large cirri at the front and back are passive while other cirri and the membranelle zone are active and create the feeding flow.

### Hydrodynamics of prey capture

We use particle image velocimetry to measure the feeding flow and particle tracking to identify which particles come in contact with the membranelles and how they are retained and transported to the mouth region. Figure 2(a) shows a measurement of the instantaneous flow field surrounding a freely swimming individual. The organism swims in the negative  $y$ -direction with a swimming speed of  $320 \mu\text{m s}^{-1}$ . The organism generates a flow towards the front of the cell against the swimming direction, and water is dragged behind the cell and pushed away at the sides, resembling a puller-type flow. The flow velocity measured in front of the cell reaches approximately  $400 \mu\text{m s}^{-1}$ . Figure 2(b) shows an individual sitting on a lump of material while generating a flow towards the cell. Representative tracks of particles that come close to or in contact with the cell are outlined with 20 ms between each marking. The particles following the two tracks in front of the organism (yellow and red) are lost. The particles come in contact with the membranelle zone but are not retained. Two particles (cyan and magenta) from further below the organism are retained and transported under the organism, whereas the particles following the two tracks (green and blue) even further below the organism are lost. The flow-rate of the part of the feeding flow from which prey particles are potentially retained by the organism is estimated from the particle tracks to  $4 \times 10^5$  cell volumes per day. This value may seem large, but it is not atypical for plankton in the marine environment [1].

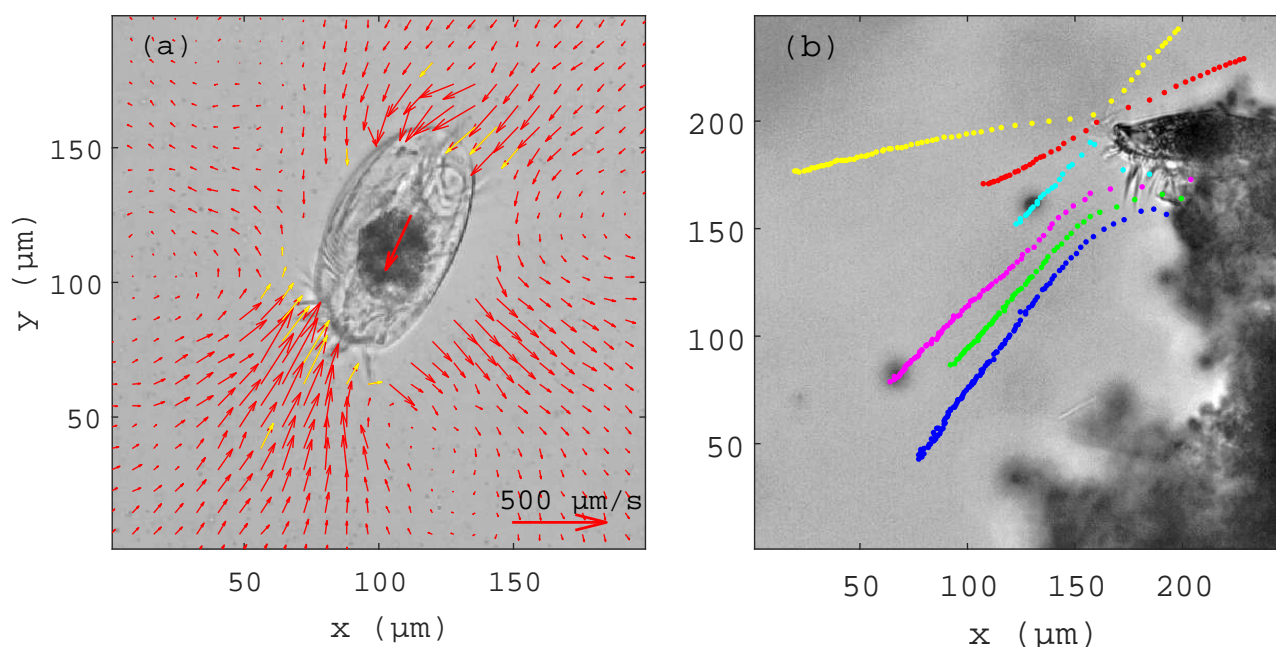


**Figure 2:** (a) Measurement of instantaneous flow field near a freely swimming *Euplotes vannus*. Dorsal view with the swimming velocity shown as the arrow at the cell center. (b) Representative particle tracks for an organism sitting on a lump of material showing retained and lost particles. During particle tracking the membranelle zone is active and creates the feeding flow, while the cirri at front are inactive.

### Conclusion

The freely swimming *Euplotes vannus* generates a strong puller-like flow field seemingly without feeding, whereas the sitting organism generates a flow, that resembles the flow due to a point force at the front of the cell. From the particle tracking we can determine which particles are retained and which are lost by the organism. Together with the particle velocity measurements these observations provide a quantitative estimate of the feeding flow. Further work on the feeding flow, particle retention, and transport by the membranelle zone is ongoing.

### References

- [1] T. Fenchel. Progress in Protistology **7**, 65-113 (1986).
- [2] T. Fenchel. Marine Ecology Progress Series **8**, 211-223 (1982).



## Microswimmer interactions with ultrasonic standing waves

Minji Kim<sup>1\*</sup>, Emma Huff<sup>2</sup>, Phillip V. Bayly<sup>1</sup>, and J. Mark Meacham<sup>1†</sup>

<sup>1</sup>Department of Mechanical Engineering & Materials Science, Washington University in St. Louis, St. Louis, Missouri, USA

\*E-mail: [kim.minji@wustl.edu](mailto:kim.minji@wustl.edu), †E-mail: [meachamjm@wustl.edu](mailto:meachamjm@wustl.edu), URL: <https://meachamlab.wustl.edu/>

<sup>2</sup>Department of Biomedical Engineering, Washington University in St. Louis, St. Louis, Missouri, USA

### Introduction

Interactions of self-propelled microorganisms and ultrasonic standing waves facilitate measurement of cell motility, as well as provide opportunities to investigate fundamental questions regarding how cells respond to external force fields. Conversely, if cell behavior is well-understood, these interactions enable rapid determination of acoustic microfluidic device performance. Herein, we demonstrate use of microswimmers as living probes to instantaneously map pressure distributions within microfluidic channels and chambers driven at resonance. Freely swimming cells allow for continuous monitoring of the evolving pressure field as operating parameters are varied. Device resonances are easily identified and field strength throughout the fluidic domain is quantified by correlating the density and distribution of swimming cells to the acoustic pressure, overcoming significant limitations of conventional acoustofluidic assessment techniques.

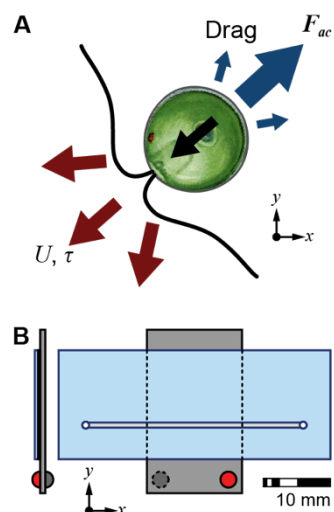


**Figure 1:** *C. reinhardtii* cells as living probes. (A) Forces acting on an acoustically-confined cell. (B) Device schematic.

### *Chlamydomonas reinhardtii* as living probes

Current methods that use passive microparticles (e.g., polystyrene beads) are time-consuming, difficult to implement, and/or inadequately describe the entire pressure field (1). As a simple, rapid, and responsive measurement tool, *Chlamydomonas reinhardtii* cells address all of these shortcomings. *C. reinhardtii* is a motile unicellular alga that is propelled by two flagella, slender whip-like organelles (Fig. 1A). Wild-type cells swim approximately ten body lengths (or  $\sim 100 \mu\text{m}$ ) per second (2). Large trapping forces hold the  $\sim 10 \mu\text{m}$ -diameter cell body, while the nanoscale flagella ( $\sim 200\text{-nm}$  diameter cross-section) are only weakly affected by low-MHz frequency ultrasound. Hence, the oscillatory motion of the flagella is not disrupted by the ultrasonic standing waves of typical acoustofluidic devices. *C. reinhardtii* cells continuously swim against an imposed force field to more completely describe the pressure distribution. *C. reinhardtii* cells also exhibit uniform size and swimming effectiveness across a given strain, and are easy to culture relative to other biological cells. Here, simple silicon-glass microfluidic chips (straight channel, width =  $765 \mu\text{m}$ , depth =  $49 \mu\text{m}$ ; Fig. 1B) are used to demonstrate our new approach.

### *C. reinhardtii* spatial distributions depict the pressure field shape

*C. reinhardtii* cells continuously probe and dynamically respond to their environment to enable real-time monitoring of changes in the pressure field with system operating conditions. For example, cell distribution as a function of swept frequency is used to automatically identify resonant frequencies of a device. The straight microfluidic channel was seeded with *C. reinhardtii* cells at  $\sim 10^6$  cells per mL. Freely swimming cells were initially at uniform density throughout the channel. The microchip was actuated using a 0.75-mm thick bulk piezoelectric transducer (APC 880, American Piezo Ceramics). Figure 2A shows the variation in correlation coefficient of successive images captured as the drive frequency was swept from 0.5 to 5 MHz at high ( $80 V_{pp}$ ) and low ( $10 V_{pp}$ ) voltages for low ( $< 1.0$  MHz) and high ( $> 1.0$  MHz) frequency ranges, respectively. At off-resonant frequencies, cells navigated the entire channel shape, and the correlation coefficient remained low. Peaks in correlation coefficient were observed at lateral resonant frequencies, where cells were tightly confined to the pressure nodal areas. In between resonant frequencies, *C. reinhardtii* cells again redistributed throughout the fluidic domain, yielding an experimental method for identification of optimal operating frequencies within a continuous frequency range.

### *C. reinhardtii* spread is related to voltage (and pressure field) amplitude

The spread of *C. reinhardtii* cells also reflects the pressure field strength. Figure 2B shows heat maps of cell distribution density as a function of swept voltage at the fixed resonant frequency 1.76 MHz. Drive voltage was linearly increased from 0 to  $20.7 V_{pp}$ . Each voltage step was actuated for 10 seconds. Brightfield images obtained during the voltage sweep were converted to binary (black/white) and black pixels (areas occupied by cells) from 50 images per voltage step were summed. The normalized densities of distributed cells were used to generate heat maps containing qualitative pressure strength information (Fig. 2B). Heat maps and

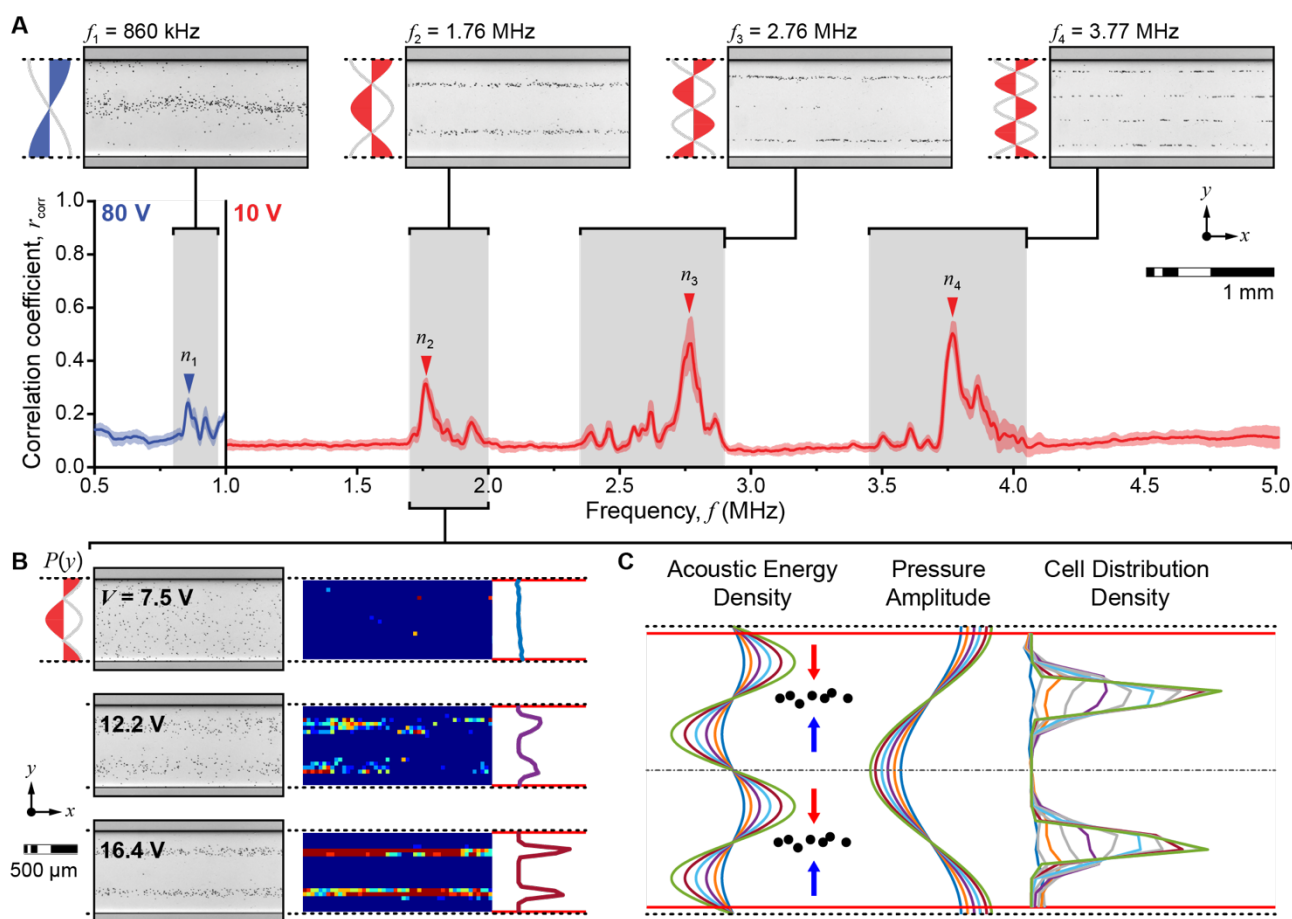


**Figure 2:** (A) Correlation of successive images for a constant voltage frequency sweep (0.5–5 MHz). Brightfield images confirm that peaks in correlation coefficient identify resonant frequencies. (B) Brightfield images and heat maps of *C. reinhardtii* cells in a straight channel driven at the second half-wavelength resonant frequency (1.76 MHz) as voltage is increased. (C) Cell distribution density, pressure, and acoustic energy density as functions of increasing voltage.

corresponding cell distribution density plots (Fig. 2C) suggest that cell confinement is a function of actuation voltage (and pressure) amplitude. The cells continuously respond to their environment and map out the pressure field as the field strength is varied. At low voltages, cells navigate the entire channel. As voltage is increased, cells become confined to smaller and smaller regions near pressure nodes. These regions are bounded by a threshold radiation force (see acoustic energy density, Fig. 2C) that cannot be overcome. Hence, the lateral cell distribution density evolves from a flat line (uniform density) into a double peak (Fig. 2C). The spatial location of the threshold for cell confinement is voltage and cell-strain dependent. When the field is turned off, cells immediately redistribute, enabling one to pause and resume an experiment with adjusted parameters.

## Conclusion

*C. reinhardtii* cells are used as living probes to automatically identify acoustofluidic device resonances and to qualitatively map the pressure field strength. By establishing *C. reinhardtii* as an effective performance measurement tool, we hope to enhance the feasibility of acoustofluidic devices, and thus, to accelerate adoption of these technologies in emerging biomedical applications. In addition to the utility of mapping the field, our platform allows study of fundamental interactions between self-propelled swimmers and applied acoustic fields. Active matter swimming dynamics can be affected by external fields (3), and *C. reinhardtii* exhibit negative gravitaxis [i.e., they swim upward in response to an external gravitational field (4)]. It is unknown whether orientation and swimming speed are affected by exposure to an ultrasonic standing wave. We will use our system to investigate this research question, among others.

## References

- [1] R. Barnkob, P. Augustsson, T. Laurell, and H. Bruus. *Lab Chip* **10**, 563-570 (2010).
- [2] J. Guasto, K. Johnson, and P. Gollub. *Phys. Rev. Lett.* **105**, 168102 (2010).
- [3] S. Takatori, and J. Brady. *Soft Matter* **10**, 9433-0445 (2014).
- [4] A. Roberts. *Biological Bulletin* **210**, 78-80 (2006).



## Instabilities of light-induced bioconvective flows

Aina Ramamonjy<sup>1</sup>, Julien Dervaux<sup>1</sup>, and Philippe Brunet<sup>1</sup>

<sup>1</sup>Laboratoire Matière et Systèmes Complexes UMR 7057, CNRS et Université Denis Diderot, 75013 Paris, France

E-mail: aina.ramamonjy@univ-paris-diderot.fr

### Introduction

Directed motions of micro-organisms slightly denser than their ambient fluid create spatial gradients of density from which macroscopic self-generated convective flows can arise. The associated concentration patterns are referred to as bioconvection patterns. Physico-chemical signals or passive physical forces can induce directed motions. In this study, we trigger lateral phototaxis using a localized light source to accumulate micro-algae *Chlamydomonas Reinhardtii* (CR) cells at the center of a shallow suspension. The bioconvection patterns are well understood when using a simple light source : a small gaussian spot [1]. We are now investigating the phase diagram of the bioconvection patterns when the light source becomes wider. Thus we can tune the relative importance of convection, radial phototaxis and a possible vertical phototaxis.

### Theoretical background

Bioconvection is a low Reynolds number self-sustained instability arising from density gradient in suspensions of swimming micro-organisms. Bioconvective patterns depend on a non-trivial coupling between the cell concentration field and the flow field self-generated by the algae. It is quantified by the Rayleigh number ( $Ra$ ) which compares the timescales of diffusion and buoyancy-driven fall. A bias of the random run and tumble motion is necessary for bioconvection and the averaged swimming direction resulting from this bias is also critical for bioconvection. Childress et. al, theoretically analyzed the case of micro-organisms swimming against gravity in a finite depth suspension [2] and showed that bioconvection happens only above a critical Rayleigh number. In our case, CR cells tend to swim along the horizontal light gradient, perpendicularly to gravity, so that there is no threshold for the onset of bioconvection, as in lateral thermal convection. A phototactic function that compares the timescales of the cells diffusion by random motion and the space dependent phototaxis quantifies the bias of the swimming direction.

### Experimental setup

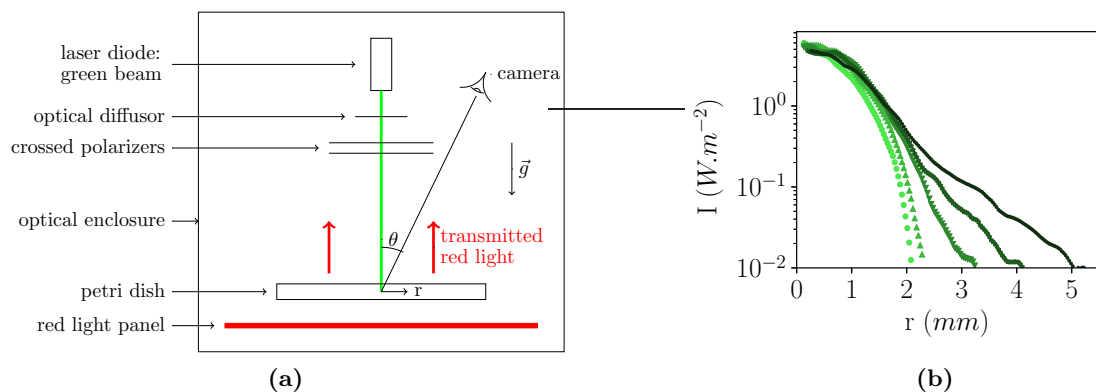


**Figure 1:** (a) A thin layer of a suspension of CR cells lays in a horizontal diameter petri dish and a green laser beam points at the center of the petri dish. Optical diffusers widen the divergence of the laser beam and crossed polarizers allow to change the light intensity. A LED panel with a red-light filter is placed below the petri dish. The transmitted red-light is visualized from the top. The CR concentration field averaged over the height of the layer can be accessed on the red channel of the images. (b) Radial profiles of different widths for the green light intensity. The profile with the minimum width is obtained without diffuser. The combined use of diffusers and crossed polarizers allow to widen and soften the light gradient by displacing the light intensity into the tail of the beam.

Figure 1 shows the experimental setup. In the petri dish of 140mm diameter, the typical cells concentration and layer height are respectively  $1-4 \times 10^6$  cells.mL<sup>-1</sup> and 1-5 mm. Thus the range in Rayleigh number varies from 10 to 1000. The combined use of diffusers and crossed polarizers enable to widen

the light radial gradient at constant maximum at the center (fig1b). The red-light illumination does not interfere with the lateral phototaxis since CR are blind to red light.

### Building of a phase diagram of bioconvective patterns

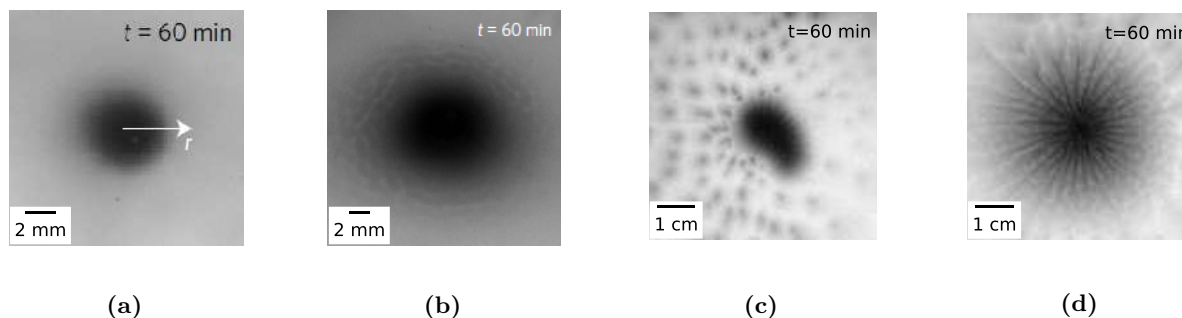


**Figure 2:** Effect of the Rayleigh number and the size of the light gradient on bioconvection patterns. (a) Small Rayleigh number  $Ra < 80$  and small light source[1]. (b) Large Rayleigh number  $Ra > 100$ , and small light source[1]. (c) Small Rayleigh number  $Ra < 80$  and light source widened with diffusers. (d) Large Rayleigh number  $Ra > 200$  and light source widened with diffusers.

Figure 2 shows the different concentrations patterns that are observed when changing the Rayleigh number and the light gradient size. We are building the corresponding phase diagram. Some regions are well identified in this diagram. At small  $Ra < 80$  with a small light source, the concentration pattern is radially symmetric and stationary (fig 2a). When  $Ra$  is increased  $Ra > 100$  with a small light source, the radial symmetry is broken into unstationary travelling waves (fig 2b). The effect of the size of the light gradient is investigated by widening the light source using diffusers (fig 2c,d). At small  $Ra < 80$ , growing fingering instability are sometimes observed (fig 2c). They become increasingly rare above  $Ra > 100$ . At large Rayleigh number  $Ra > 200$ , well-branched patterns are systematically observed (fig 2d).

Next, we try to rationalize the instabilities that we have observed. With a small light source, unstationary travelling waves were understood as the result of a gyrotactic effect in the  $(\vec{e}_r, \vec{e}_z)$  plane [1]. Gyrotaxis happens when the viscous torque is strong enough to deviate cells from their preferential orientation along the light gradient, and it can lead to self-focusing of microalgae [3]. With a wider and softer light gradient, phototaxis is weakened at the center but has a wider range. Gyrotaxis in the  $(\vec{e}_r, \vec{e}_\theta)$  plane could explain the new non-radially symmetric instabilities. Upward swimming triggered by a wider light source could also be taken into account, as suggested by the dot-like patterns around the central pattern (fig 2c,d) [4].

### Conclusion

Using a small light source to trigger lateral phototaxis could be seen as the simplest case of using a light pattern to trigger localized bioconvection in a thin layer of an active suspension. The system is very sensitive to the light gradient and by widening a little bit the light source, we uncover a great richness of new instabilities. In parallel to those experiments, our approach is to study each of them as a breaking of the radial symmetry observed with a small light source at low Rayleigh number and to analyse the induced convective flows that are susceptible to generate long-distance flows far from the laser beam. We try to understand what is the instability mechanism in each case. Such complex light-controlled fluid flows could find important applications in bioreactors, such as the generation of chaos in laminar fluid flows.

### References

- [1] J. Dervaux, M. Cappellazzi Resta, and P. Brunet. Nature Physics **13**, 306-312 (2017).
- [2] S. Childress, M. Levandowsky and E.A. Spiegel Journal of Fluid Mechanics **69**, 591-613 (1975).
- [3] X. Garcia, S. Rafai, and P. Peyla Physical Review Letters **110** **13**, 138106 (2013).
- [4] C. Rosie Williams and Martin Alan Bees Journal of Experimental Biology **214**, 2398-2408 (2011).



## A minimal model for *Spiroplasma* chemotaxis

Christian Esparza López<sup>1</sup>, Eric Lauga<sup>1</sup>

<sup>1</sup>Department of Applied Mathematics and Theoretical Physics, University of Cambridge, Cambridge CB3 0WA, United Kingdom

E-mail: [ce347@cam.ac.uk](mailto:ce347@cam.ac.uk)

### Introduction

The bacterium *Spiroplasma* is a tiny helical bacterium that swims and performs chemotaxis in a non conventional way. Based on experimental observations [1,2], we develop in this study a minimal model to describe *Spiroplasma* chemotaxis. We start by developing a resistive-force theory model of the bacterium swimming gait and we obtain expressions for the total linear and angular displacements of the cell body after one stroke. Observing that the swimming gait corresponds to a run-and-reverse motion, we next propose a random walk model to describe the random motion of *Spiroplasma* on long timescales. Finally, introducing a bias in the duration of each stroke depending on the bacterium swimming direction with respect to a defined chemical concentration gradient, we calculate the chemotactic drift. We validate our analytical results against numerical simulations.

### Swimming of *Spiroplasma*

*Spiroplasma* is a helical shaped bacterium with no flagella that swims by progressively shifting the chirality of its body. The change in geometry gives rise to a wall domain, termed a kink, which propagates along the cell body. The chirality is then reverted in a similar fashion, thereby completing a swimming stroke. The whole deformation is non-reciprocal in time, therefore net movement at low Reynolds number can be achieved. Experimentally, and as expected intuitively, the bacterium moves in the direction opposite to the propagation of the kink pair. The time between strokes has been measured in experiments to be exponentially distributed with rate  $\lambda_k \simeq 1 \text{ s}^{-1}$  while the time between a kink pair follows a normal distribution with mean  $\tau_p \simeq 0.26\text{s}$ . The kink pair propagates at an average speed  $v_0 \simeq 10.5 \mu\text{m/s}$  which is linearly related to the swimming velocity,  $v_s$  [1]. It has been further observed that the change in chirality occurs in the absence of external stress, therefore the body bends with an angle  $\theta = \pi - 2\phi \simeq 110^\circ$ , where  $\phi \simeq 35^\circ$  is the pitch angle of the helical body [3]. The total arc length of *Spiroplasma* is  $L \simeq 10 \mu\text{m}$  and its diameter  $a \simeq 100 - 200 \text{ nm}$ . The organism can thus be considered to be a slender body and resistive-force theory can be applied to describe its motion. We then model the organism as a deformable rod performing the swimming stroke in Fig. 1.

In order to make analytical progress, we consider the case  $d = v_0\tau_p/L \ll 1$  which is supported by experimental observations. Indeed, according to Shaevitz et al. [1],  $v_0 \simeq 10 \mu\text{m/s}$ ,  $\tau_p \simeq 0.25 \text{ s}$  and  $L \simeq 10 \mu\text{m}$  hence  $d \simeq 1/4$ . We further focus on the case in which the motion occurs in a plane (this assumption will be relaxed in future work). In this regime it is possible to show that the net angular displacement after one stroke vanishes. This result follows from the fact that the gait is symmetric under a half turn around an axis perpendicular to the plane of motion and time reversal. We are also able to obtain analytic expressions for the linear displacement as a function of  $d$  and  $\theta$ .

### *Spiroplasma* chemotaxis

Experimental observations of the chemotactic *Spiroplasma eriocheiris* show that the bacterium body has a definite orientation, with a distinguished tapered end [3]. It has also been observed that the bacterium swims most of the times in the direction of the tapered end. Moreover, the propagation of the kink pair can reverse its direction of motion and the reversal rate  $\lambda$  is altered in response to different chemoattractants, increasing when the concentration decreases and vice-versa. Together with the fact that there is no reorientation of the cell body after one stroke, we can think of the motility pattern of *Spiroplasma* to be of the run-and-reverse kind. We build a theoretical random walk model in which reorientation due to thermal noise is considered. In homogeneous environments we expect the average duration of a stroke to be independent of the direction of motion and therefore in the long time the bacterium displays effective diffusion. However, if we add a chemoattractant, the duration of the swimming stroke is shorter when the bacterium moves up the gradient than when it moves down the gradient. Hence, we can show that modulation of  $\lambda$  with respect to the rotational diffusion coefficient is sufficient to account for *Spiroplasma* chemotaxis and we obtain an expression for the chemotactic drift as a function of  $d$  and  $\theta$ .

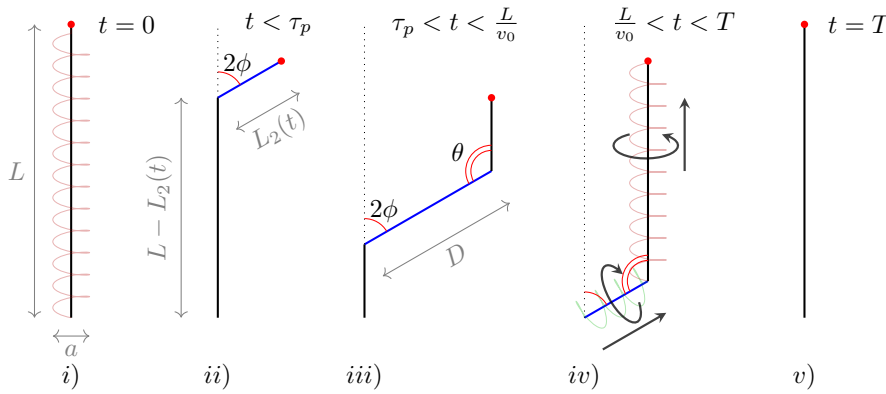


**Figure 1:** *Spiroplasma* swimming stroke described in the frame of reference in which the tail is static. i) Initially the body has a right handed helical shape, a kink appears at  $t = 0$  and propagates from head (red circle) to tail along the body of length  $L$  at speed  $v_0$ . ii) The deformed rod has two domains of size  $L_2(t)$  and  $L_1(t) = L - L_2(t)$ . iii) The second kink forms at  $t = \tau_p$ , the maximum distance between kinks is denoted by  $D = v_0\tau_p$ . iv) The configuration is similar to that of ii), with reversed signs of the forces and torques acting on the body, the blue segment has left handed chirality and rotates clockwise, while the right handed segment rotates anticlockwise. The arrows represent the induced force. v) The stroke finishes at  $T = \tau_p + L/v_0$ .

## Conclusion

Our first model for the motion of *Spiroplasma* shows that modulation of the reversal rate of kink propagation is sufficient for the bacterium to achieve chemotaxis. It also allows us to get some insight on the role of the helical structure of the cell body, through the dependence on  $\theta$  of the linear displacement after one stroke. In future work we will extend our model to consider the dynamics in three dimensions and further details on the helical shape of the bacterium.

## References

- [1] J. W. Shaevitz, J. Y. Lee, and D. A. Fletcher, *Cell* **122**, 941-945 (2005).
- [2] P. Liu, H. Zheng, Q. Meng, N. Terahara, W. Gu, S. Wang, G. Zhao, D. Nakane, W. Wang, and M. Miyata, *Front. Microbiol.* **8:58** (2017).
- [3] H. Wada, and R. R. Netz, *Phys. Rev. Lett.* **99**, 108102 (2007).



## Cavitation in Traumatic Brain Injuries

Juliette Amauger<sup>1,3</sup>, Thibault Guillet<sup>1,2</sup>, Caroline Cohen<sup>1,2</sup>, and Christophe Clanet<sup>1,2</sup>

<sup>1</sup>LadHyX, UMR 7646 du CNRS, École polytechnique, 91128 Palaiseau, France  
E-mail : juliette.amauger@ens.fr

<sup>2</sup>Physique & Mécanique des Milieux Hétérogènes, UMR 7636 du CNRS, ESPCI, 75005 Paris, France

<sup>3</sup>Département de Physique, École Normale Supérieure, PSL Research University, 75005, Paris, France

### Introduction

Traumatic Brain Injury (TBI) is a major healthcare problem, increasingly occurring in sports like rugby, boxing or football<sup>1,2</sup>. The occurrence of TBI is dependent on the head acceleration and the duration of the shock, as expressed by the empirical Wayne State Tolerance Curve (WSTC)<sup>3,4</sup> (See Figure 1.(a)) However, the Wayne Curve does not provide any explanation about the physical origin of brain concussion. One of the possible causes of TBI is the formation of cavitation bubbles in the cerebro-spinal fluid. To investigate this hypothesis, we use a model experiment to simulate TBI that consists in hitting an enclosed tank filled with water to simulate human brain .

### Experimental setup

To build a container equivalent to the head, we have to account for the observation that, during a heart cycle, the intracranial volume changes ( $\Delta ICV$ ) of a few milliliters while the intracranial pressure ( $ICP$ ) increases by several millimeters of mercury<sup>5</sup>. The selected model experimental setup consists of an acrylic reservoir with a flexible membrane placed at its bottom. Adjusting the bending stiffness of the membrane allows us to reproduce with high fidelity the in-vivo relation between  $ICP$  and  $\Delta ICV$ . This reservoir is then clamped on the falling mass of a three-meter tall drop tower impact device. Upon impact on a damper, the reservoir is accelerated up to 1000 g ( $a$ ) during 0 to 30 ms ( $\tau$ ), set by the height of the fall and on the damper characteristics.

### Modeling and prediction

The time evolution of the cavitation bubbles is captured with a 20000 fps high speed camera, and can be modeled using the Rayleigh-Plesset equation that balances inertia, pressure, capillary force and viscosity. Integrating this equation, leads to a prediction for  $R$  and in particular for the maximum value  $R_{max}$ , for any parameters ( $a, \tau$ ). But we can also express  $R_{max}$  analytically with a simplified version of the Rayleigh-Plesset equation, in which we neglect viscous and capillary terms compared to

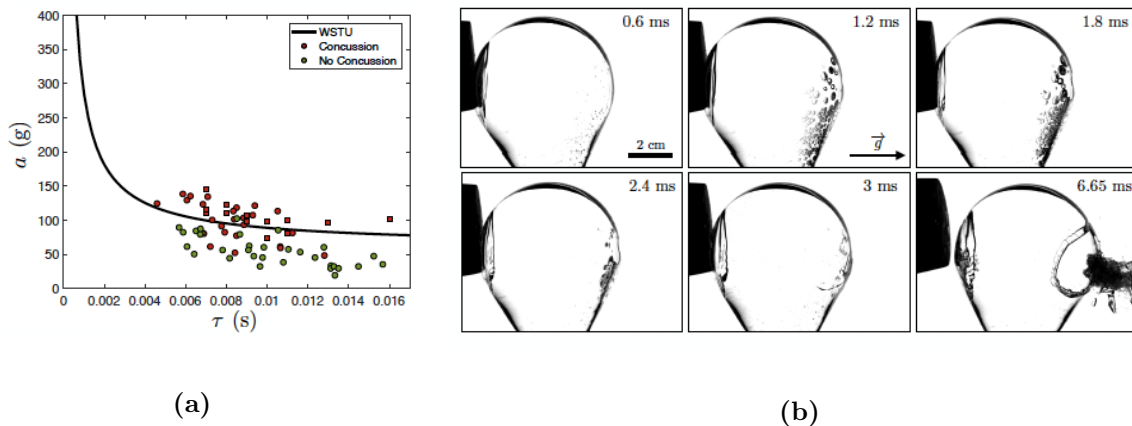


**Figure 1: Traumatic Brain Injuries and the damaging potential of cavitation bubbles. (a).** The Wayne State University (WSTU) tolerance curve delimits the head tolerance on application of a shock of peak linear acceleration  $a$  for a duration  $\tau$ . For a shock lying above the curve, there is a high probability of brain concussion. Dots are data recorded for shocks on football players taken from Pellman 2003 where the characteristic time of the shock was calculated from the Severity Index (SI). Squares are concussion cases recorded in football taken from Broglio 2010<sup>6</sup> **(b).** Chronophotography of a rounded bottom flask filled with water impacted on the left with a hammer at  $t = 0$  ms. Bubbles appear at the point opposite of impact (contrecoup location) 0.6 ms after the shock, grow until they reach their maximum radius at  $t = 1.8$  ms and then rapidly collapse. At  $t = 3$  ms, all the bubbles have collapsed and the glass is shattered at the focusing point. The flask is intact at the point of impact.

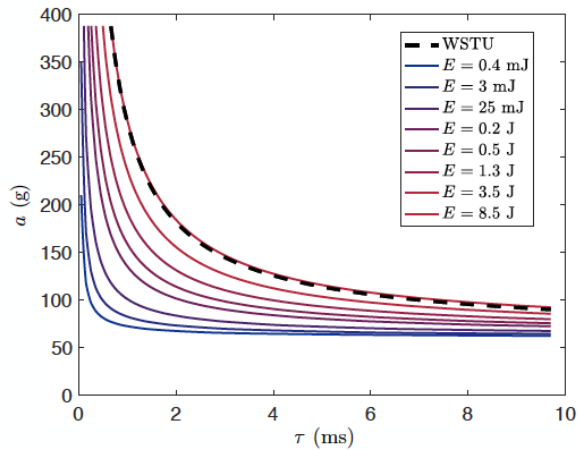


**Figure 2: Iso-energy curves in the  $(a, \tau)$  diagram and comparison with the Wayne State University curve.** The energy  $E = \rho a L R_{max}^3$  released by a bubble can be calculated using equation (1), which allows us to plot isoenergy curves in the  $(a, \tau)$  diagram. Varying  $E$  between 0.4 mJ and 8.5 generates a family of curves that gradually evolve towards the WSTU curve (dashed line) as increasing  $E$ . The value at which they matched is  $E_D = 8.5$  J.

pressure. The equation then writes  $\frac{1}{2} \frac{d(\rho R^3 \dot{R}^2)}{dt} = \Delta P R^2 \dot{R}$ , which we can see as the time evolution of the kinetic energy of the fluid entrained by the bubble arising from the work of the pressure forces at the bubble interface. The bubble growth is significant only if the acceleration is large enough to generate cavitation, that is, if it is larger than a threshold  $a_v$  given by the equation  $\rho a_v L = P_{vap}$ . This yields a threshold  $a_v$  on the order of 60 g for the parameters of our experiments. Integrating the simplified Rayleigh-Plesset equation for  $a > a_v$  and further assuming that the shock is a crenel with duration  $\tau$ , we find an analytical expression for  $R_{max}$  :

$$R_{max} \sim R_0 + \left(\frac{6\rho}{P_0}\right)^{\frac{1}{3}} \left(\frac{a_v - a}{3} L\right)^{\frac{5}{6}} \tau \quad (1)$$

Hence, we can express analytically the energy  $E$  stored in a bubble of maximum radius  $R_{max}$  : we have  $E \sim \delta p R_{max}^3 \sim \rho a L \delta p R_{max}^3$ . This energy will be release during the collapse through an energy focusing mechanism, which we assumed as necessary for brain concussion. Taking physical parameters related to those of a human's head, we compute the maximum radius and energy of cavitation bubbles during a triangular shock of peak acceleration  $a$  and half-width  $\tau$  and we plot in figure 2 the iso-energy curves in a  $(a, \tau)$  diagram.

We vary quite extensively the energy  $E$ , from 0.4 mJ to 8.5 J. For small energies (blue curves in figure 4), the iso-energy curves are almost angular, with a plateau at large  $\tau$  ( $> 3$  ms) and a strong divergence at small  $\tau$  ( $< 0.5$  ms). The plateau value is a  $\approx 70$  g, that I, the acceleration necessary to generate cavitation in the contrecoup region. The curves get higher and smoother when increasing  $E$ , and they follow a hyperbolic-like behavior when  $E$  is on the order of 1 J (red curves). Remarkably, a well-defined value of the energy, namely  $E_D = 8.5$  J, is found to follow the WSTU curve in the whole range of parameters which suggests that a scenario based on cavitation can explain the empirical WSTU criterion.

## Conclusion

Cavitation as a damaging process captures most of the characteristics of traumatic brain injuries : damages on the brain are located at the point opposite of impact (contrecoup injury), they appear at acceleration greater than 50 g, their severity depend on both the peak acceleration and the duration of the shock, result reminiscent with the empirical laws draw for TBI, in a similar fashion to empirical observations. This study should be the starting point for the derivation of refined models taking into account the energy focusing mechanism of the collapse of a cavitation bubble near brain tissues.

## References

- [1] Powell, J. W. Barber-foss, "K. D. in High School Athletes". Context **48824**, 3â8 (2011).
- [2] G.W., R., D., A. C., B. "The occult aftermath of boxing". J. Neurol. Neurosurg. Psychiatry **53**, 373â378 (1990).
- [3] Gurdjian, E. S., Roberts, V. L. Thomas, L. M. Tolerance curves of acceleration and intracranial pressure and protective index in experimental head injury. J. Trauma **6**, 600â604 (1966).
- [4] Lissner, H. R., M. Lebow, and F. G. E. Experimental studies on the relation between acceleration and intracranial pressure changes in man. Surg. Gynecol. Obstet. **111**, 329 (1960).
- [5] Unnerback, M., Ottesen, J. T. Reinstrup, "P. ICP curve morphology and intracranial flow-volume changes : a simultaneous ICP and cine phase contrast MRI study in humans". Acta Neurochir. (Wien). **160**, 219â224 (2018).
- [6] Broglio, S. P. et al. "The Biomechanical Properties of Concussions in High School Football". Med. Sci. Sport. Exerc. **42**, 2064â2071 (2010).



# Freezing morphologies inside a droplet impacting on a cold surface

Pallav Kant<sup>1</sup>, Robin Koldewei<sup>1</sup>, Kirsten Harth<sup>1</sup>, Michiel van Limbeek<sup>1,2</sup> and Detlef Lohse<sup>1,2</sup>

<sup>1</sup>Physics of Fluids, University of Twente, 7500 AE Enschede, Netherlands

<sup>2</sup>Max Planck Institute for Dynamics and Self-Organization, 37077 Göttingen, Germany

E-mail: p.kant@utwente.nl

## 1 Introduction

Impact of a droplet on an undercooled solid surface instigates a number of physical processes simultaneously, including drop scale fluid motion, heat transfer between the liquid and the substrate, and the related phase transition. Whereas a large number of studies have investigated the corresponding interface deformations and the spreading of a droplet after it impinges onto an undercooled surface [1], the *kinetics* of phase transition within the impacting droplet has been addressed only in a few [2]. Moreover, among the studies concerning solidification kinetics, only the regimes where phase transition effects are slower than the fast dynamics of droplet impact have been investigated. Here, we explore freezing behaviours that arise due to the rapid solidification of an impacting droplet at a sufficiently high substrate undercooling. Such scenarios are encountered in a number of industrial processes ranging from additive manufacturing to thermal plasma spraying of ceramics and metallic materials etc.

In the present work, we adapt the total-internal-reflection (TIR) technique [4] to visualise the phase transition in the vicinity of the liquid-substrate interface after a droplet impacts onto an undercooled transparent surface. This technique reveals the existence of distinct freezing morphologies at different undercooling. Also, it allows us to monitor the delamination of the frozen-splat from the substrate at later time.

## 2 Experimental setup

A schematic diagram of the experimental setup is shown in Fig. 1. In each experiment, a pendant drop was released from the tip of a needle with an outer(inner) diameter of 240(100)  $\mu\text{m}$ . The balance between surface-tension and gravity forces ensured that all droplets were of a similar size ( $1.58 \text{ mm} \pm 20 \mu\text{m}$ ). The employed liquid in the reported experiments was Hexadecane (99%, Sigma-Aldrich), however, a few experiments were also performed with 1-Octadecene (Sigma-Aldrich) to confirm the non-exclusiveness of different freezing morphologies. Hexadecane is optically transparent and has a high melting point of  $18^\circ\text{C}$ . The liquid has a density  $\rho = 770 \text{ kg/m}^3$ , surface tension  $\sigma = 27 \text{ mN/m}$ , dynamic viscosity  $\mu = 3.47 \times 10^{-3} \text{ Pa s}$ , specific heat  $c_p = 2310 \text{ J/kg K}$ , latent heat of fusion  $L = 2.3 \times 10^5 \text{ J/kg}$  and thermal diffusivity  $\alpha = 8.40 \times 10^{-8} \text{ m}^2/\text{s}$ . The impact velocity  $U$  was varied by adjusting the vertical distance between the horizontal substrate and the needle. The impact event was recorded in side-view as backlit shadow-graphs and in bottom-view *via* total-internal-reflection technique. The impact velocity and shape/size of the droplet at the time of impact were measured from side-view images recorded with a high-speed camera (Photron APX-RS) at 10000-14000 fps with a macro lens. Bottom view observations (*via* TIR) were recorded using a high-speed camera (Photron Fastcam SA-X2) connected to a long-distance microscope (Navitar 12x Telecentric zoom system) at 80 000 fps.

The horizontal surface of a sapphire prism (Crystan Ltd.) of thermal conductivity  $k_s = 34.60 \text{ Wm}^{-1}\text{K}^{-1}$  was used as a model surface in the experiments. It was placed in direct contact with a liquid-cooled aluminium holder. For TIR imaging, a 60 mW diode laser beam ( $\lambda = 643 \text{ nm}$ ) was introduced to the prism via mirrors at a certain incident angle. The incident angle was carefully chosen such that it is greater than the critical angle  $\theta_{\text{TIR}} > \sin^{-1}(\frac{n_d}{n_s})$ , where  $n_d = 1.434$  and  $n_s = 1.760$  are the refractive indices of liquid hexadecane and sapphire, respectively. This ensured that in the bottom views recorded *via* TIR, the liquid in contact with the sapphire surface is not visible. However, an evanescent wave emerges in the droplet, whose intensity decays in an exponential like manner within one-wavelength distance from the substrate. Hence, when a growing crystals in the vicinity of the substrate interacts with the evanescent wave it is visible in the images.

### References

- [1] M. Pasandideh-Fard *et al*, Phys. Fluids, 8(3):650-659, 1996.
- [2] M. Schreimb *et al*, Phys. Rev. E., 95(2):022805, 2017.
- [3] M. Shirota *et al*, Phys. Rev. Lett., 116, 064501, 2016.

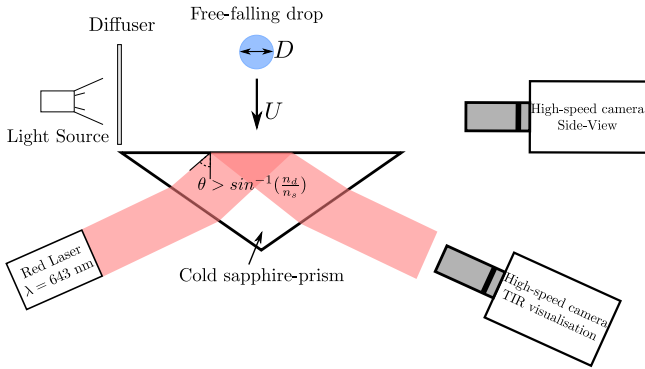


**Figure 1:** Schematic diagram of the Total Internal Reflection (TIR) method employed to reveal freezing morphologies during the impact of a droplet.

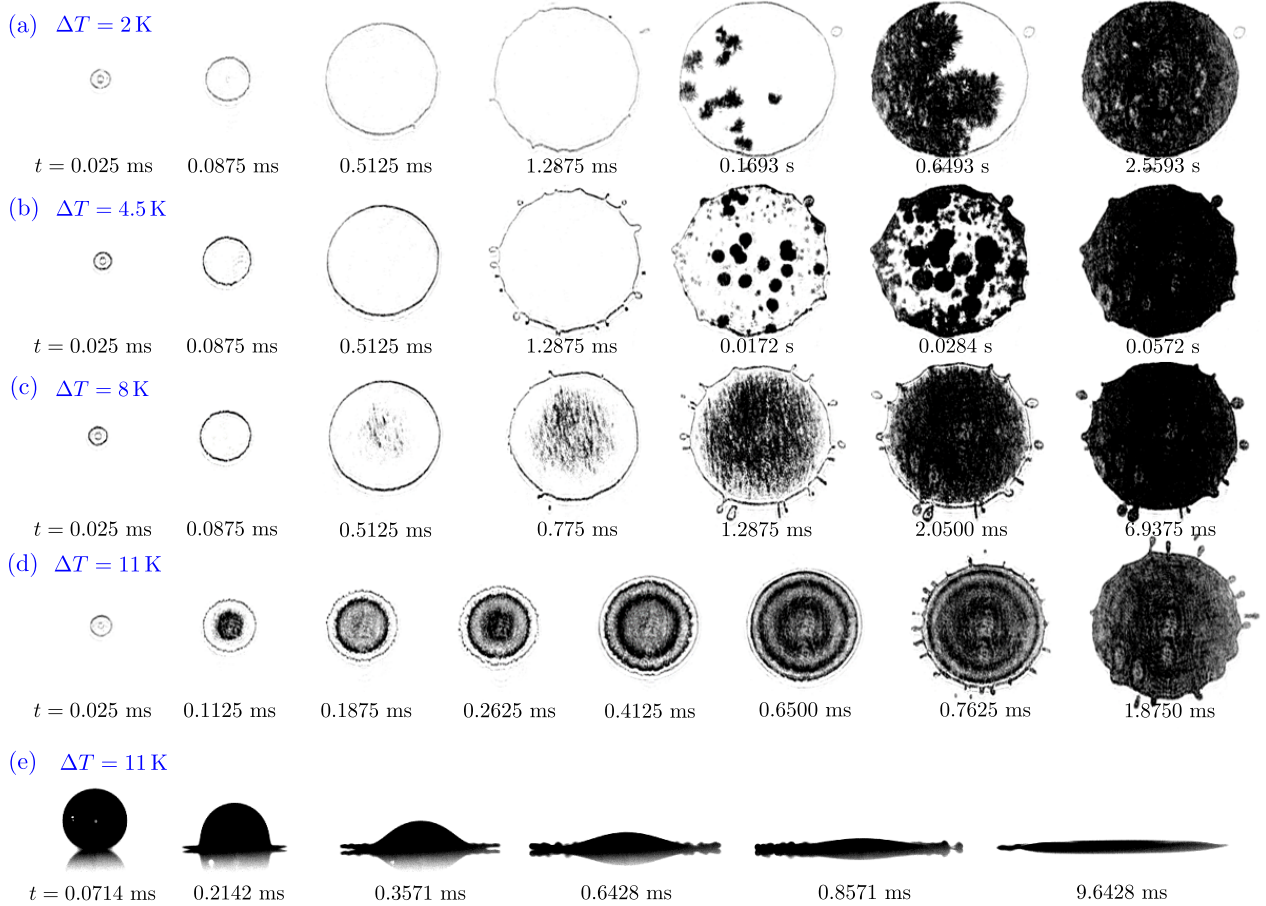


**Figure 2:** (a-d) Sequences of experimental snapshots highlighting the effect of substrate undercooling  $\Delta T = T_m - T_s =$  (a) 2 K (b) 4.5 K (c) 8 K (d) 11 K on the freezing morphology of an impacting droplet. In all the cases the velocity and the temperature of the droplet at the time of impact are  $U = 2.8\text{ m/s}$  and  $T_d = 20^\circ\text{C}$ , respectively. (e) Typical interface deformations associated with the impact of a droplet of size  $D = 1.58\text{ mm}$  on an undercooled surface; recorded in side view at 14000 fps.



## Water freezing and frosting on lubricant impregnated surfaces

Lukas Hauer<sup>1,2</sup>, Markus Schremb<sup>2</sup>, Cameron Tropea<sup>2</sup>, Hans-Jürgen Butt<sup>1</sup>,  
Doris Vollmer<sup>1</sup> and William S.Y. Wong<sup>1</sup>

<sup>1</sup>Physics at Interfaces, Max Planck Institute for Polymer Research, Mainz, Germany

<sup>2</sup>Institute of Fluid Mechanics and Aerodynamics, Technische Universität Darmstadt, Germany

E-mail: hauerl@mpip-mainz.mpg.de

### Introduction

Lubricant impregnated surfaces have shown improved anti-icing properties [1]. Due to the impregnation of lubricant into a micro-texture, the surface becomes slippery. Other materials, such as water, hardly pin on the substrate. This enables easy removal of water drops in liquid or in solid state from the surface [2]. During condensation frosting of water on lubricant impregnated surfaces, lubricants can wick in the dendritic frost structure [3]. This causes depletion of lubricants from the textured surface. However, since the lubricant is essential for the anti-icing characteristics of the substrate, a permanent depletion of the lubricant significantly degrades its ability to repel ice. To understand the dynamic processes of lubricant reorganization during the process, condensation frosting on lubricant infused substrates is investigated, using Laser Scanning Confocal Microscopy. This technique allows, for the first time, to monitor the depletion dynamics during condensation frosting in a space and time resolved manner. This renders a theoretical investigation of the wicking process possible, using Darcy's law. This law describes the flow within a porous network, such as the frost dendrites constitute.

### Lubricant impregnated surfaces

The investigated surface consists of a solid micro-pillar array in which a lubricant is impregnated. The micro-pillar array (Fig. 1 a) is produced using the photoresist SU-8 [4]. For the lubricant silicone oil is chosen. A fluorophore marker is dispersed in the silicone oil to facilitate discrimination between the lubricant from the rest of the substrate and the frost. The lubricant is impregnated into the micro-pillar array by placing a few drops onto the substrate. Capillary forces then cause the formation of a homogeneous layer (Fig. 1 b).

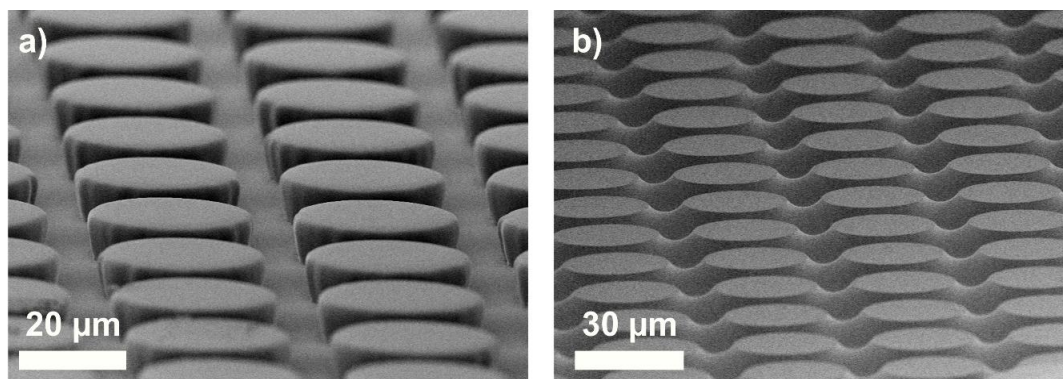


**Figure 1:** Scanning Electron Microscope image of lubricant impregnated surface. **a)** Micro-textured surface without the lubricant. **b)** Lubricant is impregnated in between the pillars.

### Condensation frosting

When the substrate is exposed to a humid atmosphere (Fig. 2 a) liquid water droplets condense on the surface. In the experiments the small droplets are initially visible on top of the pillars (Fig. 2 b). If the condensing droplets are sufficiently cooled, they start freezing from their bottom surface. The freezing front ends at the apex of the droplets where a spiky tip is formed, due to the axial expansion of the water (Fig. 2 c) [5]. The atmosphere is still supersaturated with respect to the temperature of the substrate and the frozen water droplets. Thus, water vapor desublimates on the frozen droplets as frost. The frost exhibits a dendritic structure which constitutes a capillary network. The oil wicks the capillary structure of the dendrites; therefore, the oil volume in between the pillars depletes (Fig. 2 d).

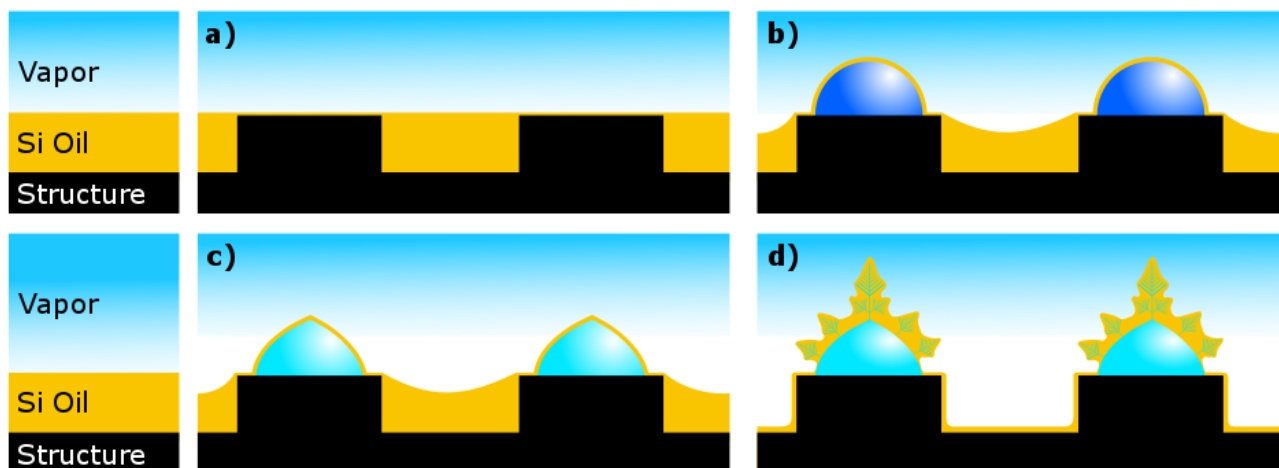


**Figure 2:** Illustration of the subsequent events during condensation frosting on a lubricant impregnated surface. **a)** Substrate exposed to humid atmosphere. **b)** Droplets condense on top of the pillars faces. The droplets are covered by a thin layer of lubricant because the spreading coefficient,  $S$ , is positive ( $S \approx 12$  mN/m [6]) **c)** Frozen droplets with a spiky tip. The lubricant cloaks the droplets. **d)** Dendrites desublimite on the frozen droplets surface. The capillary network of the dendrites wicks the oil on top of the frozen droplets, resulting in a lubricant depleted textured surface.

### Reorganization of lubricant

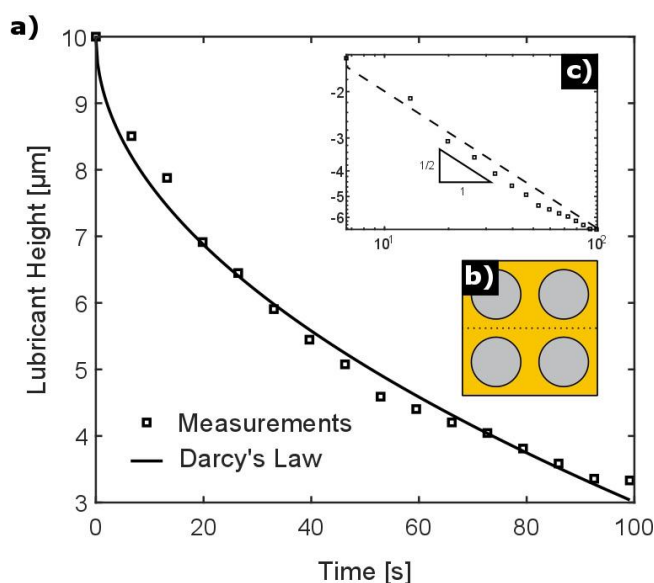


**Figure 3:** Reorganization of the lubricant during condensation frosting. **a)** Averaged lubricant height over time. **b)** Top view schematics of 2x2 pillar section; the dashed line indicates where the lubricant height is monitored. **c)** Logarithmic plot of averaged lubricant height vs. time.

### Conclusion

We captured lubricant reorganization during condensation frosting using Laser Scanning Confocal Microscopy. For the first time, a theoretical comparison of the lubricant height in between the pillar structure to experimental obtained data was possible. This led to a better understanding of the depletion process, providing new insights into the growth dynamic of frost on lubricant impregnated surfaces.

### References

- [1] Alvarenga et al. *ACS Nano*, **6(8)**, 6569–6577, (2012)
- [2] Niemelä-Anttonen et al. *Advanced Materials Interfaces*, **5.20**, 1800828, (2018)
- [3] Rykaczewski et al. *Langmuir*, **29(17)**, 5230–5238, (2013)
- [4] Arscott. *Lab on a Chip*, **14(19)**, 3668–3689, (2014)
- [5] Marín et al. *Physical Review Letters*, **113(5)**, 1–5, (2014)
- [6] Teisala et al. *Physical Review Fluids*, **3(8)**, 1–13, (2018)
- [7] Whitaker. *Transport in Porous Media*, **1**, 3–25, (1986)

The lubricated surface is attached to a cooling element to control its temperature with an accuracy of  $\pm 1$  K. The substrate is placed together with the cooling element into a humidity chamber to initiate condensation frosting. The substrate is invertedly mounted to the microscope stage allowing direct observation of the top surface of the impregnated surface. Since the condensing droplets are relatively small, gravity can be neglected. At the center line, in between the pillars (Fig 3 b; dashed line) the height profile of the lubricant can be extracted. The height profile is averaged over the center line and a scalar value is received for each time step. This averaged height is plotted in Fig. 3 a over time. The average height decays with a square root profile (Fig. 3 c). The depletion dynamic of the lubricant in the spaces between the pillars fits well with Darcy's law which describes the flow in a porous medium [7].



## Impinging Drop Lifts a Sessile Drop

Olinka Ramirez Soto<sup>1,2,3</sup>, Vatsal Sanjay<sup>1</sup>, Abhishek Khadiya<sup>2</sup>, Michael Kapp<sup>2</sup>, Detlef Lohse<sup>1,3</sup>, Hans-Jürgen Butt<sup>2</sup>, Jonathan T. Pham<sup>4</sup>, and Doris Vollmer<sup>2</sup>

<sup>1</sup>Physics of Fluids Group, Max Planck Center for Complex Fluid Dynamics, MESA+ Institute and J.M. Burgers Center for Fluid Dynamics, University of Twente, Enschede, The Netherlands.

E-mail: vatsalsanjay@gmail.com

<sup>2</sup> Max Planck Institute for Polymer Research, Mainz, Germany.

<sup>3</sup> Max Planck Institute for Dynamics and Self-Organization, Göttingen, Germany.

<sup>4</sup> Department of Chemical and Materials Engineering, University of Kentucky, Lexington, USA.

### Introduction

Colliding droplets have received considerable attention in the literature because of their ubiquitous presence in everyday technologies and natural processes (see pages 157–181 of [1] for a review). The outcome of these collisions depends on kinematic factors, such as the size of droplets (radius,  $R_0$ ), their relative impact velocity ( $U_0$ ) and the relative offset of their centers ( $d$ ) [1,2]. Fluid properties like surface tension ( $\gamma$ ) and viscosity ( $\mu$ ) also play a pivotal role in the flow dynamics [3].

An interesting situation is when a drop vertically impacts a sessile drop [4,5]. The fundamental difference compared to free-flying drops is the presence of an additional interface between the resting drop and the substrate. Research into high surface tension drop-on-drop impact at a superhydrophobic surface has a long history [4,5]. However, there is a relatively small body of literature concerned with the impact of hydrocarbons.

Impacts of these low surface tension drops differ from those of other liquids because they are more deformable. The deformations result in an enhanced viscous dissipation during impact. In this contribution, we present the rich rebound dynamics of low-surface tension hydrocarbons using detailed numerical simulations [6]. We aim to understand the influence of impact Weber number ( $We = \rho_l U_0 R_0 / \gamma$ , where  $\rho_l$  is the density of liquid drop) and relative offset position ( $\chi = d/R_0$ ) on the process.

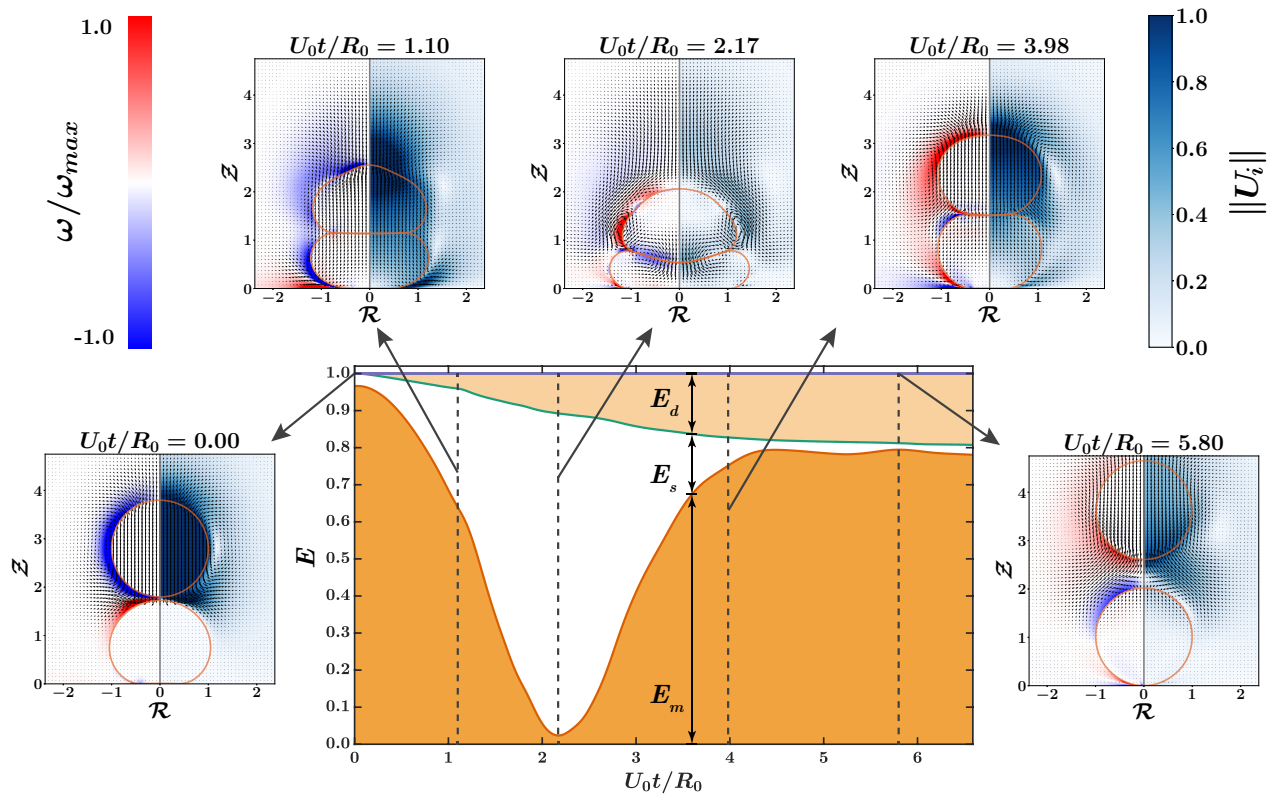


**Figure 1:** Energy budget for colliding droplets. The inset figures show the temporal evolution of the bouncing process. The left side of these insets shows vorticity contour (red for counter-clockwise rotation and blue for clockwise rotation). Both the velocity vectors and the velocity field is normalized with the capillary velocity scale,  $U_\sigma = \sqrt{\gamma/(\rho_l R_0)}$ .

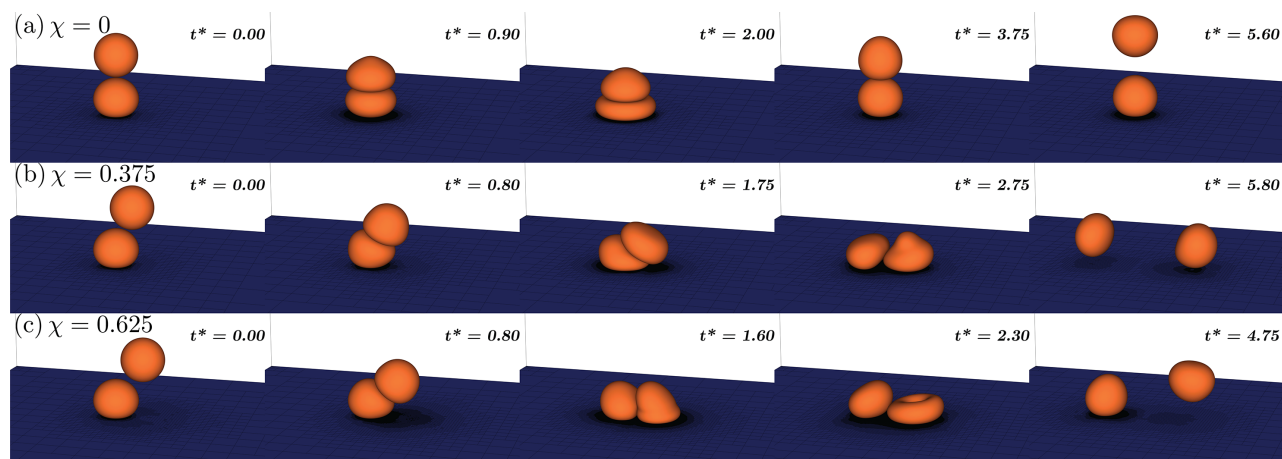


**Figure 2:** Rebound dynamics of the bouncing droplets. At a given impact velocity ( $We = 1.5$ ), changing the offset ( $\chi$ ) leads to different outcomes: (a) The impact velocity is too small to cause lift-off. (b) The impinging droplet slides off the sessile drop and then kicks the sessile drop to lift it. (c) The time of contact is too small to transfer sufficient energy to the sessile drop, and it does not lift-off.

### Temporal evolution of the bouncing droplets

Figure 1 shows different stages of bouncing drops. First, the impinging drop approaches the sessile drop (all energy is in the form of mechanical ( $E_m$ ) of the system and the surface energy ( $E_s$ ) of the sessile drop). Then, the kinetic energy of the impinging drop is transferred to the surface energy of the two drops. Both drops expand radially, and as a result, show axial compression. Furthermore, at  $U_0 t/R_0 = 2.17$ , the system reaches its minimum mechanical energy. We choose gravitational potential energy datum at this point, making its value zero. Notice that the system does not reach zero kinetic energy. This is because of the velocity rolls as observed in the inset figure at this instant. Moving forward in time, the two droplets enter a recovery stage where their surface energy reduces to increase the mechanical energy. Finally, the impinging drop goes away, and the sessile drop starts oscillating. A part of the initial total energy of the system is lost in the form of viscous dissipation ( $E_d$ ).

Strategies to lift-off the sessile droplet may involve increasing the mechanical energy of the impacting drop. However, in doing so, the probability of coalescence between droplets increases. We wish to develop a method without coalescence which we present in the next section.

### Lifting the sessile drop

Figure 2 shows the rich rebound dynamics of the collision of the binary droplets. Controlling the relative offset position ( $\chi$ ) and impact Weber number ( $We$ ), we can access a broad range of reproducible scenarios for binary oil drop impact on low adhesion surfaces. At low  $We$ , the sessile drop does not lift-off because of insufficient impact energy of the system. When the offset is small ( $\chi \rightarrow 0$ ), this effect is complemented by the impinging drop blocking the vertical motion of the sessile drop (Figure 2(a)). At high offset ( $\chi > 0.5$ ), the contact duration is too small to lift-off the sessile drop (Figure 2(c)). What is striking is that even at low  $We$ , a low surface tension oil drop impinging at an intermediate offset ( $0.1 < \chi < 0.5$ ), can lift-off a sessile drop (Figure 2(b)).

### Conclusion

This study set out to understand the rebound mechanism of a drop impinging on a sessile drop of the same liquid. We describe the different stages of this mechanism by analyzing the overall energy budget and the flow dynamics inside the droplets. Furthermore, we show that at low impact speeds, an impinging drop can still lift-off a sessile drop if the offset condition is favorable. These findings related to the removal of the droplet by bouncing can be of practical importance for many applications, including inkjet printing, spray processes, electronic packaging, and coatings.

### References

- [1] N. Ashgriz (Editor). *Handbook of atomization and sprays: theory and applications*, Springer Science & Business Media (2011).
- [2] J. Qian and C. K. Law. *Journal of Fluid Mechanics* **331**, 59–80 (1997).
- [3] K. Willis and M. Orme. *Experiments in fluids* **34**(1), 28–41 (2003).
- [4] M. Damak and K. Varanasi. *Physical Review Fluids* **3**(9), 093602 (2018).
- [5] J.H. Moon, C.K. Choi, J. S. Allen and S. H. Lee. *International Journal of Heat and Mass Transfer* **127**, 130–135 (2018).
- [6] Basilisk C. <http://basilisk.fr/>